

Institut für Theoretische Physik
Fakultät Mathematik und Naturwissenschaften
Technische Universität Dresden

Dynamics and mechanics of compartment boundaries in developing tissues

Dissertation

Zur Erlangung des akademischen Grades

Doctor rerum naturalium
(Dr. rer. nat.)

vorgelegt von

Maryam Aliee

geboren am 21.09.1984 im Iran

Max-Planck-Institut für
Physik komplexer Systeme

Dresden, 2013

Eingereicht am 03.01.2013

1. Gutachter: Prof. Dr. Frank Jülicher
2. Gutachter: Prof. Dr. Christian Dahmann

Verteidigt am 22.04.2013

Acknowledgements

I would like to thank all the people who have supported me while I pursued my PhD project.

I would like to express my special gratitude to my supervisor, Frank Jülicher, from whom I have learned a lot. I very much appreciate his support and leading advice during these years of learning and research.

I thank Christian Dahmann and his lab members, especially Daiki Umetsu, Jens-Christian Röper, Constanze Pentzold, Katharina P. Landsberg, and Thomas J. Widmann for the nice collaboration and the fruitful meetings. They provided all the fantastic experimental results I discussed in this thesis.

Furthermore, I would like to thank Jacques Prost, Jean-François Joanny, and Jonas Ranft for the inspiring discussions and their contribution to the continuum description of interfaces in tissues.

I thank all the friends and people that I had the chance to meet at MPIPKS all over these years. I express appreciation to Stephan Grill for his critical comments in my TAC meetings. I am grateful for the conversations I had with Reza Farhadifar, Peer Mumcu, Matthias Merkel, and Sebastian Fürthauer. I thank Christoph Ehrlich for the help with developing software for image analysis, Jochen Schneider, Jöbin Gharakhani, and Silvanus Alt for proofreading parts of this thesis.

Finally, I would like to thank my parents and my sisters, with whose support and encouragement my studies and research have become possible. I would like to give my deepest gratitude to my husband Alireza who is always the best friend and comrade.

Abstract

During development of tissues, cells collectively organize to form complex patterns and morphologies. A general feature of many developing epithelia is their distinct organization into cellular compartments of different cell lineages. The interfaces between these compartments, called compartment boundaries, maintain straight and sharp morphologies. The interfaces play key roles in tissue development and pattern formation. An important model system to study the morphology of compartment boundaries during development is the wing disc of the fruit fly. Two compartment boundaries exist in the fly wing disc, the anteroposterior (AP) boundary and the dorsoventral (DV) boundary. A crucial question is how compartment boundaries are shaped and remain stable during growth.

In this work, we discuss the dynamics and mechanisms of compartment boundaries in developing epithelia. We analyze the general features of interfacial phenomena in coarse-grained models of passive and active fluids. We introduce a continuum description of tissues with two cell types. This model allows us to study the propagation of interfaces due to the interplay of cell dynamics and tissue mechanics. We also use a vertex model to describe cellular compartments in growing epithelia. The vertex model accounts for cell mechanics and describes a 2D picture of tissues where the network of adherens junctions characterizes cell shapes. We use this model to study the general physical mechanisms by which compartment boundaries are shaped. We quantify the stresses in the cellular network and discuss how cell mechanics and growth influence the stress profile. With the help of the anisotropic stress profile near the interfaces we calculate the interfacial tension. We show that cell area pressure, cell proliferation rate, orientation of cell division, cell elongation created by external stress, and cell bond tension all have distinct effects on the morphology of interfaces during tissue growth. Furthermore, we investigate how much different mechanisms contribute to the effective interfacial tension.

We study the mechanisms shaping the DV boundary in wing imaginal disc at different stages during the development. We analyze the images of wing discs to quantify the roughness of the DV boundary and average cell elongation in its vicinity. We quantify increased cell bond tension along the boundary and analyze the role of localized reduction in cell proliferation on the morphology of the DV boundary. We use experimentally determined values for cell bond tension, cell elongation and bias in orientation of cell division in simulations of tissue growth in order to reproduce the main features of the time-evolution of the DV boundary shape.

Contents

1	Introduction	13
1.1	Development of two-dimensional tissues	13
1.2	Compartment boundaries in developing epithelia	14
1.3	Development of the fly wing	16
1.3.1	Anteroposterior boundary in the wing imaginal disc	18
1.3.2	Dorsoventral boundary in the wing imaginal disc	19
1.4	Biophysics of tissues	21
1.4.1	Continuum description	21
1.4.2	Vertex models	22
1.5	The Physics of interfaces	22
1.6	Overview of this work	25
2	Coarse-grained models for interfaces in passive and active systems	27
2.1	Interfaces in passive fluids	27
2.1.1	Interfaces at thermodynamic equilibrium	28
2.1.2	Stress anisotropy and interfacial tension	29
2.1.3	Driven interfaces	31
2.2	Continuum description of cellular compartments in growing tissues	34
2.2.1	Cell number balance and momentum conservation	34
2.2.2	Propagating interfaces between two cell populations	35
2.3	Summary	39
3	Mechanics of growing tissues in a vertex model	41
3.1	Work function for polygonal cell packing	41
3.2	Time evolution of cellular networks	42
3.3	Models for cell division	43
3.3.1	Division rate depending on cell pressure	43
3.3.2	Oriented cell division	44
3.4	Stresses in cellular networks	45
3.4.1	Stress tensor in the vertex model	45
3.4.2	Cell average stress tensor	47
3.5	Summary	50

4	Vertex model study of interface dynamics	53
4.1	Cellular compartments in the vertex model	53
4.2	Physical mechanisms shaping interfaces during growth	54
4.3	Stress anisotropy and effective interfacial tension associated with inter- faces	56
4.3.1	Stress anisotropy associated with interfaces	56
4.3.2	Effective interfacial tension	61
4.4	Roughness of interfaces during tissue growth	63
4.5	Summary	73
5	Experimental study of the dorsoventral compartment boundary in the developing fly wing	75
5.1	Morphology of wing imaginal discs near the dorsoventral boundary	75
5.1.1	Cell shape analysis	76
5.1.2	Roughness of the DV boundary	76
5.2	Response of wing discs to ablation of cell bonds	78
5.3	Cell division pattern in the wing imaginal disc	80
5.4	Summary	80
6	Comparison of theory and experiment	83
6.1	Estimate of cell bond tension	83
6.1.1	Simulation of bond ablation in the Vertex model	84
6.1.2	Estimate of the relative bond tension along DV	84
6.2	Estimation of the bias in the division axis	87
6.3	Estimation of anisotropic stress	88
6.4	Simulations accounting for the time-evolution of the DV morphology . . .	88
6.5	Summary	91
7	Conclusion	93
A	The Ericksen stress tensor	97
B	Stresses and force balance at cellular vertices	99
B.1	Stress tensor at cell vertices	99
B.2	Force balance at cell vertices	101
C	Quantification of cell shape	103
C.1	Tensor of cell elongation	103
C.2	Ellipse approximation for cell elongation	104
D	Effective Laplace's law in cellular networks	107

E	Morphology of interfaces	109
E.1	Quantification of interface morphology	109
E.1.1	Roughness as the average peak height	110
E.1.2	Fourier transform of the interface shape	110
E.1.3	Circle roughness	111
E.2	Scaling properties of interfaces	111
F	Cell morphology near an interface in a cellular network	115
G	Analysis of experimental images	119

List of abbreviations

°C	degree Celsius
1D	one-dimensional
2D	two-dimensional
3D	three-dimensional
A	anterior
AEL	after egg laying
AP	anteroposterior compartment boundary
<i>BrdU</i>	bromodeoxyuridine
<i>Ci</i>	<i>cubitus interruptus</i>
<i>CycE</i>	<i>Cyclin E</i>
D	dorsal
DV	dorsoventral compartment boundary
<i>DAPI</i>	4',6-diamidino-2-phenylindole
DNA	deoxyribonucleic acid
<i>DPP</i>	<i>Decapentaplegic</i>
<i>E-cad</i>	<i>E-cadherin</i>
<i>F-actin</i>	filamentous actin
GFP	green fluorescent protein
h	hours(s)
<i>Hh</i>	<i>Hedgehog</i>
μm	micrometer
P	posterior
SEM	standard error of the mean
UV	Ultraviolet
V	ventral
<i>Wg</i>	<i>Wingless</i>

Chapter 1

Introduction

1.1 Development of two-dimensional tissues

Multi-cellular organisms represent complex patterns of individual cells organized in different and specified structures. During development, one single cell undergoes several rounds of cell division to form well-ordered structures, such as eyes, hearts, legs, or lungs. This is done through different developmental processes, such as pattern formation, cell differentiation, and growth [1]. It has always been interesting to analyze the mechanisms which control the complex characteristics of developing organisms. These issues have been addressed in different model systems at particular developmental stages [1]. It is well-known that these processes are regulated by complicated signaling systems as well as cell mechanics.

Many developmental features can be studied in a simpler system, an epithelium, where cells are packed together with very little intercellular space. Cavities, surfaces of many structures in the body, such as insides of the lungs and hearths, and many glands are covered by epithelia [3]. A simple epithelium is composed of one layer of cells with similar heights (figure 1.1A). Cells are connected by adhesion connections which consist of transmembrane adhesion molecules. Adhesion junctions are more pronounced near the apical surface of cells, where they form a network. Of course the full description of the system needs the three dimensional information. However we can consider a simpler two dimensional picture where the network of adherens junctions characterizes cell shapes (figure 1.1B). This junctional network forms a stable configuration although it actively remodels during tissue growth.

During development of an epithelium, cells collectively organize to form complex patterns and morphologies. Collective organization of cells is based on the interplay of chemical signals between cells and mechanical events such as division, adhesion, apoptosis, and force generation. The signaling network controlling developmental processes involves the interaction between many different chemical molecules and signals. These signaling molecules modify tissue development through limited processes such as cell division, cell death and cell shape changes. Therefore many developmental issues can be studied from the mechanical point of view.

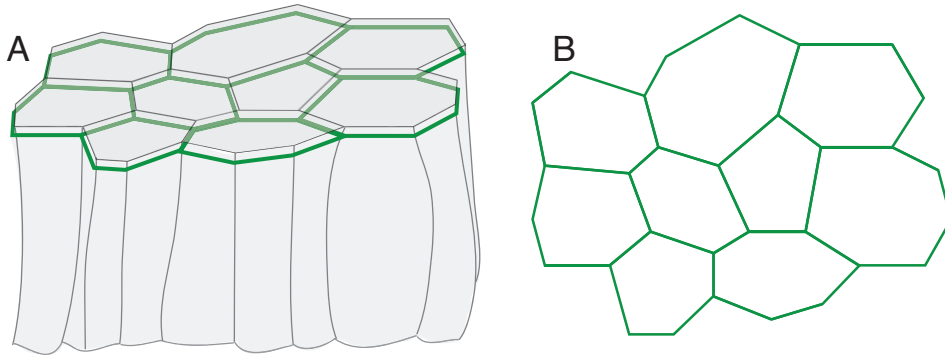


Figure 1.1: Schematic view of an epithelium. (A) The 3D structure of a simple epithelium as a single-layer sheet of cells. Cells are connected to each other via cell-cell adhesion. The adhesion molecules are enriched near the apical surface (shown in green). (B) The adherens junctions of cells characterize a network, which defines the packing properties of cells [2].

1.2 Compartment boundaries in developing epithelia

A general feature of many developing tissues is their distinct organization into cellular compartments of different cell lineages. The interfaces between these compartments, called compartment boundaries, maintain straight and sharp morphologies in tissues undergoing cell division and cell rearrangements. Figure 1.2 shows an example of cellular compartments in the wing of the fruit fly. In this figure, cells in the posterior compartments express GFP allowing to see the AP compartment boundaries between anterior and posterior cells. We can see that the AP boundary is straight and sharp in the wings of the fly. Compartment boundaries play an important role as organizers in patterning processes [5–13]. They are important examples of the interplay of chemical signals and mechanical events in the formation of patterns and morphologies.

Compartments boundaries can be visualized by lineage markers. They were first observed in the fruit fly *Drosophila* and *Oncopeltus* with the help of lineage tracking experiments [14, 15]. In these experiments a single cell which is genetically marked divides and grows to a clone of cells which are inherently marked. The border of the clone becomes irregular with many fluctuations everywhere except where it meets the compartment boundary. The clone does not pass the compartment boundary and its border is straight when the marked cells and the neighboring cells belong to different compartments (figure 1.3).

Compartmentalization has been observed in many different tissues. For instance during segmentation, *Drosophila* embryo is divided into alternating segments [1]. Within each segment there are respective anterior and posterior compartments which are separated by lineage boundaries [16]. There is also a compartment boundary in the mouse brain between midbrain and hindbrain [17]. The developing wing of the fruit fly *Drosophila* is an important model system to study the morphology of compartment boundaries. We

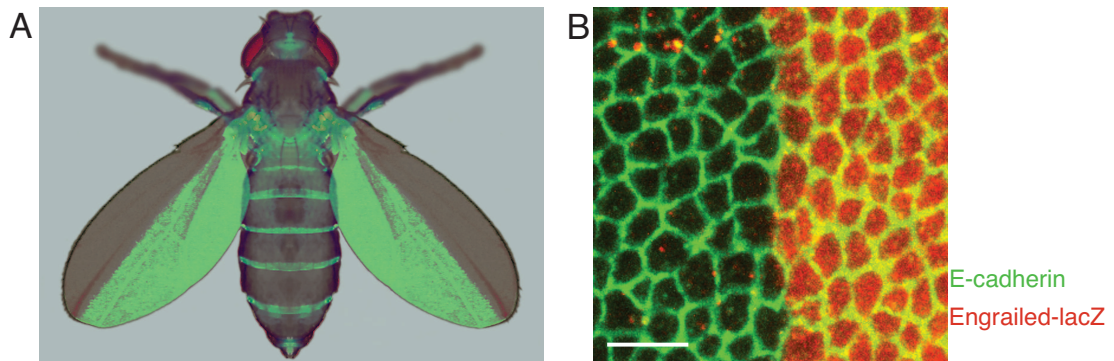


Figure 1.2: The anteroposterior boundary in the wing of the fruit fly. (A) The adult fruit fly expressing GFP under control of the *engrailed* enhancer in all cells of the posterior compartments. In particular we can see the anteroposterior (AP) compartment boundary in the wing as a sharp interface. The figure is kindly provided by Christian Dahmann. (B) The AP boundary in the wing imaginal disc at 120h AEL. The scale bar represents $5\mu\text{m}$. The figure is adopted from [4].

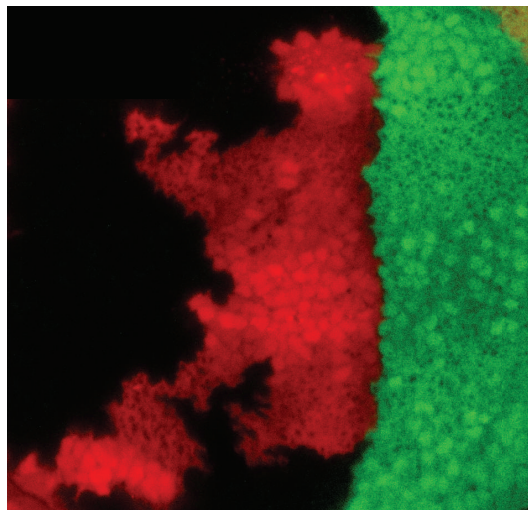


Figure 1.3: A cellular clone near the AP compartment boundary in the wing imaginal disc. The posterior compartment is visualized by green fluorescence (*Engrailed-lacZ*) and the clone is visualized by red fluorescence. The clone shows a relatively straight border along the compartment boundary, but its border is irregular everywhere else. The figure is kindly provided by Christian Dahmann.

will discuss in detail the development of the fly wing in the next section.

Cells within one compartment express specific selector genes which identify their fate, for example it controls which signals cells can send and respond to. The signaling between cells of two compartments generates a reaction-diffusion network in the vicinity of the interface specifying some cells near the boundary as organizers. Organizer cells secrete a patterning morphogen [7,9,18]. Morphogens are long range signaling molecules which diffuse in the tissues and their local concentration provides cells with their positional information. The morphogen concentration may also influence cell characteristics in order to control the size and complicated patterns of tissues. Therefore the profile of morphogen concentration is vital in tissue development. This profile is controlled by the position of organizers, which are located by compartment boundaries. The shape of the boundaries influences the profile of signaling molecules and therefore compartment boundaries play a critical role in patterning of tissues. An important question is which mechanisms form and straighten the compartment boundaries in developing tissues where stochastic processes like cell division tend to make the boundaries irregular.

In 1963 Steinberg suggested that the maintenance of compartment boundaries is based on differential cell adhesion [19]. In this model, cells within two compartment have different adhesion properties. He showed that for certain values of relative adhesions, cells within different compartments minimize their interface and sort out into separate populations. Some evidence has been observed indicating that differential adhesion may play a role in maintaining boundaries in different tissues [20,21].

More recently, it has been proposed that cell segregation can be governed by differential bond tension of cells [22]. Cell bond tension is generated by contractility of cell cortex originated from actin-myosin filaments. Further observations provide evidence of *F-actin* and *Myosin II* accumulation along the compartment boundaries in different tissues, which can be considered as indications of increased bond tension [4,23–25]. Moreover, tissue relaxation in response to laser ablation of cell bonds provides an estimate of cell bond tension [26]. The mechanisms that shape compartment boundaries are best understood in the fruit fly. In the next section, we describe compartment boundaries in the developing fly wing.

1.3 Development of the fly wing

The fruit fly *Drosophila melanogaster* is an important model system to address many developmental questions. Investigating some mechanisms and principles in *Drosophila* embryo helps to understand the development processes of many other systems [3]. The *Drosophila* development, like other animals, starts with the fertilized egg, a single specified cell. The fertilized egg develops into a larva which hatches in 24 hours after fertilization. The larval stage takes about 5.5-6 days, while most growth occurs. Larval development takes place within three stages, called *instar*, during which the larva grows, and molts at the end of each stage. Larval development is followed by the pupal stage, when adult structures are formed. The entire growth of *Drosophila* usually takes 10-12 days. The timings described here correspond to $T = 25^{\circ}C$.

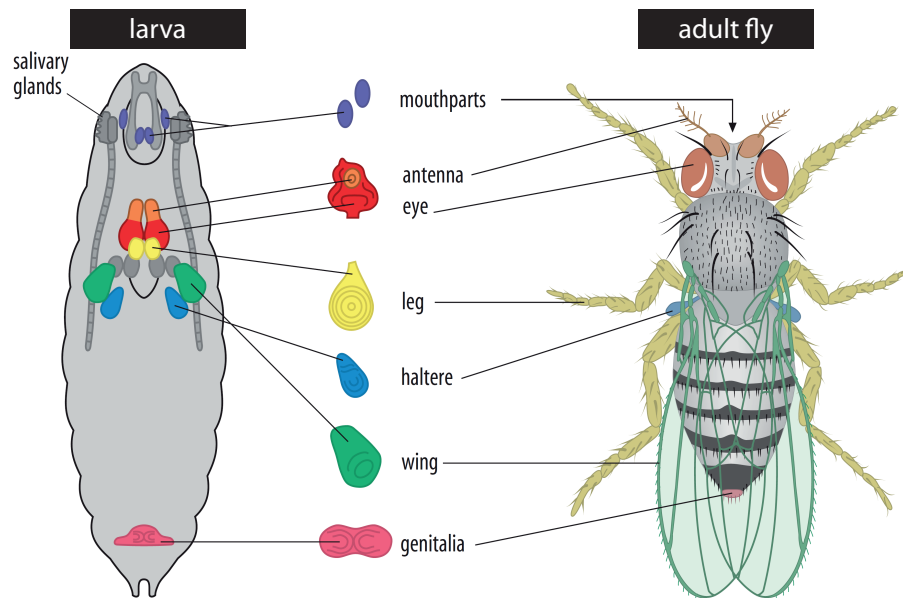


Figure 1.4: A cartoon of imaginal discs in the larva which develop and form different organs of the adult fruit fly. There are separate imaginal discs of wings, antennae, legs, eyes, genitalia, mouth parts, and halteres. The figure is adopted from [1] with permission from Oxford University Press.

Many organs of the adult *Drosophila* develop from flat epithelia in the larva, called imaginal discs. For instance, there are separate imaginal discs of wings, antennae, legs, and eyes (figure 1.4). Each imaginal disc starts out in the embryo as a group of tens of cells, and grows and differentiates into a more complex structure. Here we discuss the development of the wing imaginal disc, which starts with approximately 50 cells. It grows during larval development in approximately 10 rounds of cell division to about 50,000 cells (figure 1.5D-I).

The wing disc is a 2-side sac-like epithelium in which the apical surface of cells face inward [28] (figure 1.5B). One side includes elongated columnar cells, whereas cells on the other side are flattened, known as peripodial membrane [29]. An oval-shaped region of the columnar epithelium, called the pouch, will form the blade of the adult wing (figure 1.5A-B). The network of adherens junctions of the columnar tissue is an irregular network of different polygons which show a specific distribution of different classes of polygons [2, 30].

There are two compartment boundaries in the wing imaginal disc: the anteroposterior (AP) boundary and the dorsoventral (DV) boundary. The AP and the DV boundaries are perpendicular to each other in the wing imaginal disc (Figure 1.6A). The wing disc bends over the DV boundary during the pupal stage and the dorsal and ventral compartments become the dorsal and ventral surfaces of the adult wing (figure 1.6B).

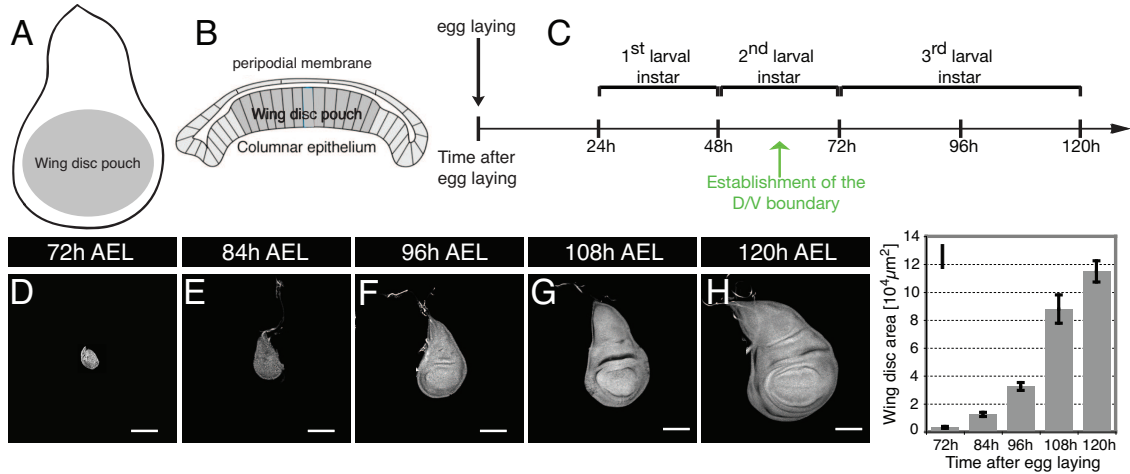


Figure 1.5: Development of the wing imaginal disc. (A) A scheme of the apical surface (xy view) of the columnar epithelium of the wing disc, the pouch is shaded in gray. (B) A scheme of the cross section (xz view) of the wing disc in the third larval instar. The wing disc is 2-side sac-like epithelium. One side includes elongated columnar cells. The pouch, which forms the blade of adult wing, is shaded in gray. On the other side, peripodial membrane, cells are more flat [27]. (C) The time line of larval development. The larval instars and approximate time point of the establishment of the DV boundary are indicated as hours AEL. (D-H) Low magnification views of wing discs (D) 72h, (E) 84h, (F) 96 h, (G) 108h, and (H) 120h AEL stained for *F-actin* (D) or *DAPI* (E-H). Scale bars represent $100\mu\text{m}$. (I) Wing disc area as a function of time after egg laying for the indicated time points. Mean and SEM are shown ($n = 5$ (72h), 6 (84h), 5 (96 h), 5 (108h), and 6 (120h) wing discs).

1.3.1 Anteroposterior boundary in the wing imaginal disc

The wing imaginal disc is initially subdivided into anterior and posterior compartments [14]. This AP compartmentation corresponds to the parasegmental compartment boundary within each segment of the embryo at the early stages [31]. The activity of selector genes and chemical signals is essential for maintenance of the AP compartment boundary [31–36]. Cells on the posterior side express the selector genes *engrailed* and *invected* which activate the expression of *Hedgehog* (*Hh*) and repress the expression of the transcription factor *cubitus interruptus* (*Ci*) [14, 37, 38]. *Hh* is a short range signaling molecule which diffuses to the anterior compartment. *Ci*, which is required for responding to the *Hh* signal, is therefore expressed only in the anterior compartment. Accordingly anterior cells produce *Decapentaplegic* (*DPP*) in a narrow stripe at the boundary where the *Hh* concentration is sufficient [31, 39] (figure 1.7A). *DPP* is a patterning morphogen which diffuses inside the wing disc and produces a decaying morphogen gradient [40]. *DPP* concentration profile provides cells with a positional information and has a strong influence on the growth of wing discs [41, 42].

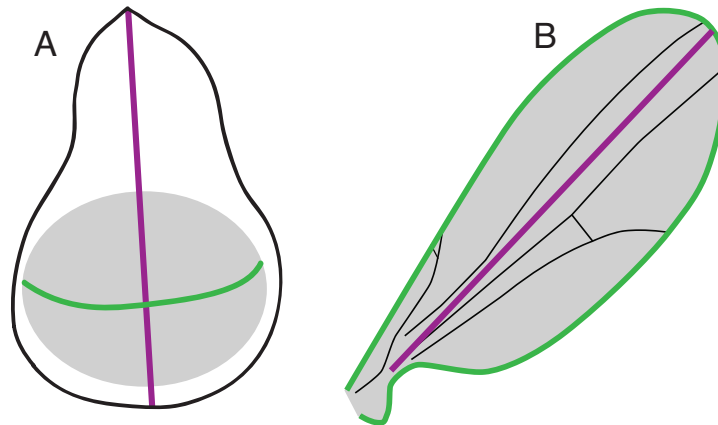


Figure 1.6: A scheme of the location of compartment boundaries in the wing of the fruit fly. The anteroposterior (AP) boundary and the dorsoventral (DV) boundary are respectively shown in violet and green, (A) in the wing imaginal disc during the larval development, and (B) in the adult wing, which is made of two layers of epithelia separated by the DV boundary.

The AP compartment boundary keeps a straight shape during wing development [4] (figure 1.2B). The shape of the AP boundary influences the profile of the *DPP* morphogen concentration. Cells near the AP boundary have a distinct morphology compared to cells elsewhere. It was previously shown that at the AP compartment boundary, cell bond tension is increased compared to the tissue. Based on experimental observations, *Myosin II* and *F-actin* are enriched along the AP compartment boundary [25]. Moreover, laser ablation experiments revealed approximately a 2.5 fold increase of cell bond tension at the AP boundary relative to the bonds elsewhere [4]. This increased cell bond tension is sufficient to prevent mixing of cells during cell proliferation and controls the shape of the boundary. It has been suggested that this locally increased cell bond tension results from cell-cell communication across the boundary [4, 43].

1.3.2 Dorsoventral boundary in the wing imaginal disc

The second compartment boundary subdivides the wing imaginal disc into dorsal and ventral compartments. The dorsoventral (DV) compartment boundary was discovered by Garcia-Bellido in 1971 with the help of clonal lineage tracing [44]. In contrast to the AP boundary it does not exist in the initial wing disc, but arises during mid-second larval instar (60h after egg laying AEL) [14, 45, 46]. It maintains a sharp and straight morphology until the end of wing development.

Similar to the AP compartment boundary, maintenance of the DV boundary requires the activity of selector genes and signaling pathways [47, 48]. Dorsal cells are identified by the expression of the selector gene *apterous* [49]. *apterous* drives dorsal synthesis of the proteins *Serrate* and *Fringe*. *Fringe* modifies *Notch*, which is expressed throughout

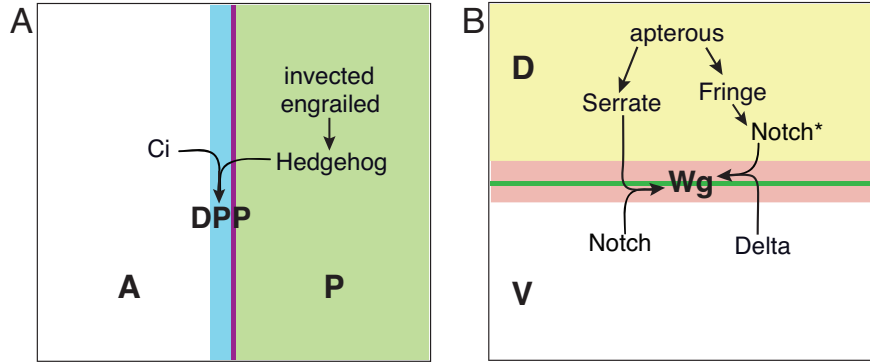


Figure 1.7: A scheme describing the signaling pathways in association with the compartment boundaries in the wing imaginal disc. (A) Signaling between compartments near the AP boundary (violet line). Cells in the posterior compartment, colored in green, express *engrailed* and *invected* which activate the expression of *Hedgehog* (*Hh*) and blocks the expression of *Ci*. Anterior cells express *Ci* which allows them to respond to *Hh* by producing *DPP* in a narrow region (indicated by the blue stripe) where the *Hh* concentration is sufficient. (B) Signaling between compartments near the DV boundary (green line). Dorsal cells, colored in light yellow, express *apterous* which leads to the synthesis of *Serrate* and *Fringe*. *Fringe* modifies *Notch* (*Notch**), so that it responds to *Delta* and not to *Serrate*. *apterous* represses the activation of *Delta*, so that *Delta* only exists in the ventral compartment. *Wingless* (*Wg*) is expressed in a narrow stripe (indicated by a pink stripe) where dorsal *Serrate* activates ventral *Notch*, and ventral *Delta* activates dorsal *Notch** [31].

the wing disc, blocking its response to *Serrate* but increasing it for *Delta*. On the other hand, *apterous* blocks the activation of *Delta*, so that *Delta* is only present in the ventral compartment. *Notch* can interact with *Serrate* and *Delta*, leading to a narrow region of *Notch* activity on both sides of the DV boundary, where dorsal *Serrate* meets ventral *Notch* and ventral *Delta* meets dorsal modified *Notch*. *Wingless* (*Wg*) is then expressed in response to intense activity of *Notch* [31, 47, 49, 50] (figure 1.7B). *Wg* behaves as an important signaling molecule which distributes in the wing imaginal disc, produces a concentration gradient, and affects the patterning of the wing disc [51–54].

It was shown that at late larval development the cell proliferation rate was reduced in a strip of cells, approximately $10 - 20\mu\text{m}$ wide [55]. It has been discussed in literature whether or not this reduced proliferation is important for shaping the boundary [24, 25, 49, 56]. Moreover, it has been observed that *Myosin II* and *F-actin* are enriched at the DV compartment boundary, which has been interpreted as a signature of increased tension [23, 24]. Furthermore, the orientation of cell division is biased in the vicinity of the DV boundary such that the division plane is frequently perpendicular to the DV boundary [24, 57]. It has been proposed that oriented cell division might influence the boundary shape [24, 58]. In chapters 5 and 6, we use a combination of theory and quantitative experiments to study the role of different physical mechanisms for shaping

the DV boundary during wing development.

1.4 Biophysics of tissues

Tissue development can be studied at different time and length scales. For example, it is well known that many tissues respond as elastic materials in short time scales, however, behave as viscous fluids in long time scales [59–62]. Furthermore, the models may take into account the details of cell components into account [63], or simplify these details to describe the system on a larger scale. Several models have been developed to describe different aspects of tissues. Here we briefly review two different approaches, a continuum coarse-grained description of tissues and a vertex model to analyze dynamics of tissues in the cellular scale.

1.4.1 Continuum description

Tissues can be described in a continuum limit, where tissue properties are averaged in a volume larger than the typical size of cells. Continuum descriptions are practical tools to study different properties of tissue development, for example cell flows or deformation of tissues or cell competition [64–66]. In particular continuum models are widely studied to describe cancer growth [67–69]. These models are based on the balance of cell numbers and forces. It is essential to consider the activity of living organisms, since cells can undergo division or death [70, 71]. Therefore active terms, proportional to the division and apoptosis rates, should be included in the balance of cell number

$$\partial_t n + \partial_\alpha (n v_\alpha) = (k_d - k_a) n . \quad (1.1)$$

Here n describes the density of cell number and \mathbf{v} is the local velocity of cells. It should be noted that throughout the thesis we use Einstein summation notation, i.e., repeated indices is summed. The division and apoptosis rates are respectively represented by k_d and k_a . These rates are in general dependent on local pressure, characterized by the homeostatic pressure of cells, at which cell division and apoptosis balance [67, 72]. Furthermore, the stress tensor is given by a constitutive material relation which includes terms accounting for cell apoptosis and cell division. One can study the flow profiles that result from cell divisions [73].

Tissues effectively behave like viscoelastic materials. It is valid even if cells are considered as elastic solids at time scales smaller than cell division cycle [74]. In this system, stresses relax like a viscous fluid at time scales longer than cell division cycle. This viscous behavior is driven by the coupling of cell division and cell death to the local stresses. Cell division provides an active anisotropic stress whose direction is set by division axis. On the other hand, cell elongation, which is proportional to the anisotropic stress, biases the axis of cell division. This is based on the observation that in many tissues, the cleavage plane frequently bisects dividing cells perpendicular to their long axis [75, 76].

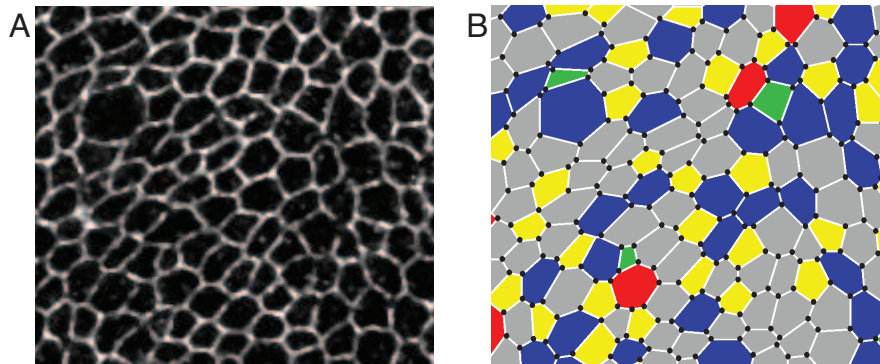


Figure 1.8: 2D morphology of epithelia. (A) The network of adherens junction of a wing imaginal disc as an epithelium. (B) Cell bonds are replaced by straight lines in the same epithelium. This approximation is used in the vertex model. Cell bonds meet at cell vertices which are shown by black dots. Each cell is represented by a polygon which is colored by the number of its neighbors, 4: green, 5: yellow, 6: gray, 7: blue, 8: red.

1.4.2 Vertex models

Vertex models describe epithelia at the scale of individual cells [2, 72, 77]. Due to the flat nature of the epithelium as stated in section 1.1, a simple epithelium can be described by the network of adherens junctions. The junctional network defines cell packing properties which have various structures in different tissues [78, 79]. It is interesting to study epithelia packing properties, like the distribution of different classes of polygons, cell area and cell shape [80–82].

In the vertex models, cells are represented by polygons that are adhered together along cell bond (figure 1.8). A cellular network consists of a particular number of cells where each cell is described by the position of cell vertices and their connections. Cell division and cell rearrangements are introduced in the cellular network, and the network configuration is determined by minimizing an energy function which accounts for the mechanical properties of cells. In this thesis, we use the vertex model introduced in [2] to simulate tissue growth. We discuss the bases of this model in chapter 3. Simulations of this vertex model showed very good agreement with the wing imaginal disc of the fruit fly with respect to the cell packing properties [2, 83, 84].

1.5 The Physics of interfaces

It has always been fascinating to study interfaces between different phases, such as the interface between a liquid and its vapor in a closed bottle, the interface between two immiscible fluids, or the interface of a liquid drop and surrounding air. Interfaces have also been investigated in living systems. An interesting example is the interface between a population of cancer cells and the host tissue [85]. The border of bacterial colonies is another example which have striking features [86]. Despite the diversity of interfaces,

some general characteristics of them have been studied.

Mechanics of interfaces in a binary system. One can analyze the properties of interfaces in a two-component system. The Hamiltonian of such a system depends on the interaction between molecules of different types. This helps to calculate the partition function and the free energy of the system. Based on the strength of the interaction between molecules relative to the thermal energy, the free energy may have one or two minima. This defines a two-phase region of the phase diagram, where two distinct phases can coexist [87]. For the other choices of characteristic parameters, the single minimum of the free energy describes a mixed configuration.

In a two component system, both the energy and the entropy of molecules are different at the interfaces compared to the bulk. Interfacial tension is known as the extra free energy per unit area needed to move molecules from the bulk to the interface [88]. It has respectively the dimension of energy per unit area, or per unit length for a 2D surface, or a 1D line. We will discuss the basic concepts of a standard model to study interfaces in passive fluids in section 2.1.

Morphology of interfaces. The shape of interfaces changes dynamically in time. In particular interfaces get rough in the presence of noise. The morphology of interfaces depends on the scale by which they are observed. For example, a surface can be straight to eye, but looks rough under a microscope [89]. There are different standard methods to quantify the shape of surfaces and interfaces. Here we briefly describe two methods to analyze the shape of 1D interfaces, however, the methods can be generalized to 2D surfaces. The shape of an interface is identified by a function $h(y)$ describing the orthogonal distance of the interface from the reference line (figure E.1). For any distance L along the interface, interface roughness w is determined by the average variance of excursions of the boundary away from the average straight line

$$w^2 = \langle (h - \bar{h})_L^2 \rangle . \quad (1.2)$$

Here \bar{h} represents the mean value of $h(y)$ within the distance L and the averages are done within the distance L and along the interface (see appendix E for details). Interface roughness is a function of distance L and can change during time, $w = w(L, t)$. The Fourier transform of an interface $\tilde{h}(q)$ is also used to describe its shape as a decomposition into periodic functions with different wavelengths

$$\tilde{h}(q) = \int_{-\infty}^{\infty} e^{-2\pi i q y} h(y) dy . \quad (1.3)$$

In Chapter 4 we use these methods to analyze the shape of interfaces in our growth model.

One of the basic concepts in various roughening processes is scaling [90, 91]. The scaling behavior of interfaces does not depend on many details of the system. Roughness quantities show simple scaling properties, although there are many differences in the

characteristics of the material and their dynamics. In a large number of systems, starting from a straight interface, roughness increases as a power of time $w(L, t) \propto t^b$. This is valid for short times, and in many cases, roughness is then saturated. b is the growth exponent, and the growth and saturation regimes are separated by the crossover time t_x . The crossover time depends on the length scale with a power law $t_x \propto L^z$, where z is called the dynamic exponent. Moreover, the saturation value of roughness scales with the length L by the roughness exponent a . Roughness scaling properties can be summarized in this relation

$$w(L, t) = L^a f\left(\frac{t}{t_x}\right), \quad (1.4)$$

where $f(u)$ shows two different scaling properties in two limits

$$f(u) = \begin{cases} u^b & \text{if } u \ll 1 \\ \text{const} & \text{if } u \gg 1 \end{cases}. \quad (1.5)$$

The three exponents are related by $z = a/b$.

In addition, the Fourier transform of interfaces $\tilde{h}(q)$ scales with the wavelength

$$|\tilde{h}(q)|^2 \propto q^f. \quad (1.6)$$

The Fourier exponent f is related to the growth and roughness exponents a, b . Concerning the interface dynamics and the correlation of noises, one can calculate the relation between these exponents [89].

Effective description of the dynamics of interfaces. Different models have been developed to analyze the dynamics of interfaces in different systems. For example the KPZ equation describes the stochastic growth of interfaces with interfacial tension and bending rigidity [92]. Of utmost interest for active systems is the Fisher wave equation, which was originally suggested to describe the spread of genes in a population [93, 94]. It was later used to study the growth of populations and many reaction-diffusion systems. The Fisher equation is a nonlinear reaction diffusion equation describing the dynamics of the quantity φ , which can be the concentration of a specific gene or the volume fraction of one population [93]

$$\partial_t \varphi = k \varphi(1 - \varphi) + D \partial_x^2 \varphi, \quad (1.7)$$

where k is the reaction coefficient and D is the diffusion coefficient. This equation has two homogenous steady states, $\varphi = 0$ and $\varphi = 1$ which are unstable and stable respectively. It suggests that this equation can have traveling wave solutions, where φ reaches steady state values $\varphi = 0$ and $\varphi = 1$, at each side far from the interface. The traveling wave solutions of the Fisher equation have been widely studied. In section 2.2, we discuss a generalized version of the Fisher equation which describes the dynamics of an interface between two cell populations influenced by cell mechanics.

1.6 Overview of this work

In this thesis, we analyze how interfaces evolve during tissue growth. In the next chapter we discuss the general properties of interfaces in continuum models. A two-component passive fluid can be described by the Ginzburg-Landau free energy. We analyze the system near the equilibrium state and study how the interface influences the stress profile. Stress anisotropy allows us to calculate the interfacial tension. This model can be extended to study interfaces in active systems. A coarse grained model will be introduced based on the balance of cell numbers and conservation of momentum. We study the case where two cell populations with different homeostatic pressures are separated by an interface and analyze the propagation of the interface.

In Chapter 3, we describe a vertex model to study the tissue growth at the level of cellular junctions. Cell growth is in general influenced by cell mechanics, like cell pressure or cell anisotropy. This will be considered in the growth model of the vertex model. We also quantify the stress tensor in this model as a function of elasticity of cells and line tension along the bonds. Local changes in mechanical properties as well as cell division modify the stress profile locally. The vertex model can be used to analyze the cellular compartments in developing tissues. In Chapter 4, we discuss general physical mechanisms by which compartment boundaries are shaped during the growth phase. We quantify stress profile near the interfaces, and study how different mechanisms contribute the interface stress anisotropy and interfacial tension. We analyze interface morphology, and show that these mechanisms have distinct effects on the morphology of compartment boundaries during tissue growth.

In Chapter 5 and 6, we briefly review our experimental results using the developing *Drosophila* wing as a model system. We analyze the morphology of the dorsoventral compartment boundary at different time steps during wing growth. We also quantify anisotropic shape of cells in the vicinity of the DV boundary. By measuring tissue relaxation in response to laser ablation of cell bonds at different developmental times, we estimate the increased cell bond tension along the compartment boundary. We also quantify proliferation pattern in the wing imaginal discs and analyze whether reduction of proliferation near the DV boundary is important for shaping the boundary. Finally, using the parameters experimentally determined, we compare our theoretical model with the time evolution of the shape and mechanics of the DV boundary.

Chapter 2

Coarse-grained models for interfaces in passive and active systems

In this chapter we discuss the basic concepts of continuum coarse-grained models to study the compartments in tissues. We start from a passive fluid with two compartments. This system can be described by the Ginzburg-Landau free energy. We analyze the interfacial tension in the system and derive it from stress anisotropy. We later generalize this model to study an active system considering active sources of mass and stresses.

2.1 Interfaces in passive fluids

There are different physical models describing multi-component fluids. Here we briefly describe a well-known model to study interfaces in passive fluids. We are interested in a binary fluid, which is composed of 2 different species A and B . $\phi(\mathbf{r})$ describes the volume fraction of A molecules, and in the case that there is no free space the volume fraction of B molecules equals to $1 - \phi(\mathbf{r})$. The free energy of the system can be calculated considering the interaction of the molecules and their entropy. In the continuum limit with a mean field approach, the free energy density can be written as [87]

$$f(\phi) = \frac{1}{a_0^3}(k_B T[\phi \log \phi + (1 - \phi) \log(1 - \phi)] + \frac{1}{2}j\phi(1 - \phi)) + \frac{j}{4a_0}|\nabla\phi|^2. \quad (2.1)$$

Here $k_B T$ is the thermal energy and j describes the interaction of A and B molecules. The lattice size is given by a_0 which is, for simplicity, considered to be the same for both species. Furthermore, the fluid is considered as an incompressible fluid. The total free energy is calculated by integrating f over volume $F = \int f(\phi)d^3r$. In the limit close to the critical composition, the free energy density can be expanded around $\psi = \phi - 1/2$. This expansion leads to the Ginzburg-Landau free energy

$$f(\psi) = -\frac{\epsilon}{2}\psi(\mathbf{r})^2 + \frac{c}{4}\psi(\mathbf{r})^4 + \frac{B}{2}|\nabla\psi(\mathbf{r})|^2, \quad (2.2)$$

where $B = j/(2a_0)$, $\epsilon = (j - 4 k_B T)/a_0^3$, and $c = 16 k_B T/(3a_0^3)$.

In a homogenous fluid, the gradient of volume fraction vanishes and the remaining part of the free energy is a polynomial function of ψ . It has two symmetric minima $\psi = \pm\psi_0^m$, where $\psi_0^m = (\epsilon/c)^{1/2}$, if ϵ is positive. For $\epsilon \leq 0$, it has just one minimum at $\psi = 0$ (figure 2.1A) [95].

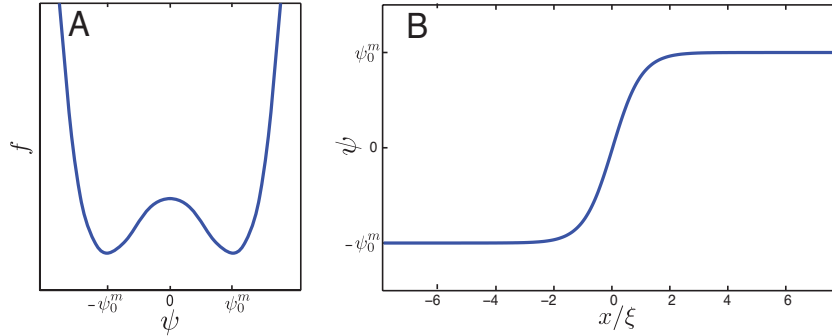


Figure 2.1: (A) The profile of the Ginzburg-Landau free energy described in equation 2.2 as a function of volume fraction ψ in a homogenous fluid. It has two symmetric local minima at $\psi = \pm\psi_0^m$ and one local maximum at $\psi = 0$. (B) Volume fraction as a function of the position x in a two component fluid at thermodynamic equilibrium. x is normalized by the interface width ξ .

2.1.1 Interfaces at thermodynamic equilibrium

The Ginzburg-Landau free energy has two distinct minima with the same energy, for positive values of ϵ . It implies that two phases can coexist in a system at thermodynamic equilibrium. In such a system, we need to take into account the gradient term in the free energy (equation 2.2). To find the equilibrium state, we minimize the total free energy with respect to the function $\psi(\mathbf{r})$ which reads

$$\frac{\delta f}{\delta \psi} = \frac{\partial f}{\partial \psi} - \frac{\partial}{\partial r_i} \frac{\partial f}{\partial (\partial_{r_i} \psi)} = 0. \quad (2.3)$$

For the Ginzburg-Landau free energy it requires

$$-\epsilon \psi(\mathbf{r}) + c \psi(\mathbf{r})^3 - B \nabla^2 \psi(\mathbf{r}) = 0. \quad (2.4)$$

We consider a simple picture where the two phases are separated with an interface perpendicular to x -axis. The system is symmetric along the interface (y direction) and therefore ψ is only x dependent in a 2D picture. Far from the interface two distinct phases $\psi = \pm\psi_0^m$ exist on both sides. In this geometry the analytical solution of the equation 2.4 is given by

$$\psi(x) = \sqrt{\frac{\epsilon}{c}} \tanh\left(\frac{x}{\xi}\right), \quad (2.5)$$

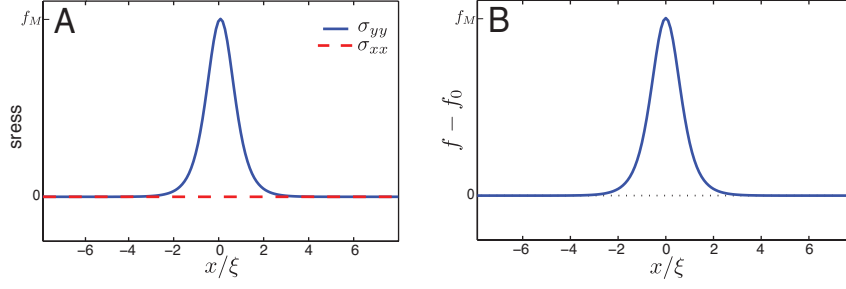


Figure 2.2: (A) The profile of stresses σ_{xx} and σ_{yy} as a function of the distance from the interface x in a two component fluid at thermodynamic equilibrium, (equation 2.8). (B) The free energy deviation from the bulk value as a function of x in the same system. $f_M = \epsilon\sqrt{B/(2c)}$ and x is normalized by the interface width ξ .

where $\xi = (2B/\epsilon)^{1/2}$ describes the width of the interface. There is a mixed configuration in the vicinity of the interface, however, when $x \rightarrow \pm\infty$ the volume fraction reaches two uniform steady states. Figure 2.1B shows the profile of volume fraction ψ as a function of distance from the interface.

2.1.2 Stress anisotropy and interfacial tension

In this section we analyze the stress profile in the two component fluid. We calculate the stress components for a system described by a free energy which is a function of volume fraction ψ and its gradients $\partial_\alpha\psi$ (see appendix A for details)

$$\sigma_{\alpha\beta} = (f - g)\delta_{\alpha\beta} - \frac{\partial f}{\partial(\partial_\alpha\psi)}\partial_\beta\psi. \quad (2.6)$$

Where f is the free energy density and g is the chemical potential. For the Ginzburg-Landau free energy (equation 2.2) g vanishes in the equilibrium state and the stress tensor is given by

$$\sigma_{\alpha\beta} = f\delta_{\alpha\beta} - B\partial_\alpha\psi\partial_\beta\psi. \quad (2.7)$$

The non-diagonal stress components vanish and the diagonal components are

$$\begin{aligned} \sigma_{xx} &= -\frac{\epsilon}{2}\psi(x)^2 + \frac{c}{4}\psi(x)^4 - \frac{B}{2}|\partial_x\psi(x)|^2, \\ \sigma_{yy} &= -\frac{\epsilon}{2}\psi(x)^2 + \frac{c}{4}\psi(x)^4 + \frac{B}{2}|\partial_x\psi(x)|^2. \end{aligned} \quad (2.8)$$

Considering the profile of the volume fraction ψ (equation 2.5), σ_{xx} is a constant equals to $-\epsilon^2/(4c)$. Interestingly, σ_{yy} has a gradient as far as $\partial_x\psi$ is nonzero and is equal to σ_{xx} far from the interface. The stress profile is plotted in figure 2.2A as a function of the distance from the interface.

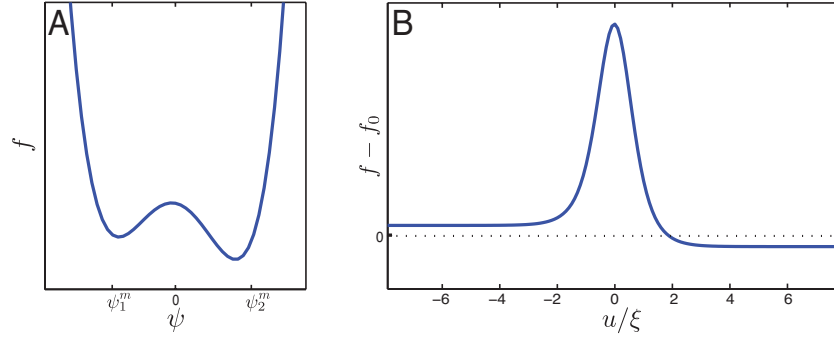


Figure 2.3: (A) The profile of the Ginzburg-Landau free energy for a non-zero external field described in equation 2.12 as a function of volume fraction ψ in a homogenous fluid. It has two local minima at ψ_1^m and ψ_2^m and one local maximum. (B) A scheme of the free energy deviation from the bulk value as a function of the distance from the interface u in a two component fluid. u is normalized by the interface width ξ .

The anisotropic part of the stress tensor is $\tilde{\sigma} = (\sigma_{yy} - \sigma_{xx})/2$. If the two component system is large enough we expect that the anisotropic stress reaches a constant value far from the interface (bulk). The anisotropic stress deviates from the bulk value in the vicinity of the interface. We calculate the interfacial tension by integrating the deviation of anisotropic stress from its bulk value

$$\gamma = 2 \int_{-\infty}^{+\infty} (\tilde{\sigma} - \tilde{\sigma}_0) dx . \quad (2.9)$$

The bulk anisotropic stress $\tilde{\sigma}_0$ does not vanish in general, however, it vanishes in the binary fluid described by the Ginzburg-Landau free energy (equation 2.8). For such a two component fluid the interfacial tension is

$$\gamma = B \int_{-\infty}^{+\infty} (\partial_x \psi)^2 dx = \frac{4}{3} \frac{B \epsilon}{c \xi} . \quad (2.10)$$

This is in consistence with the interfacial tension calculated by the free energy profile [87]. Figure 2.2B shows the profile of the free energy density as a function of the distance from the interface. The interfacial tension is calculated by integrating the deviation of the free energy from the bulk free energy

$$\gamma = \int_{-\infty}^{+\infty} (f - f_0) dz = B \int_{-\infty}^{+\infty} (\partial_x \psi)^2 dx , \quad (2.11)$$

where f_0 is the free energy density inside bulks and far from the interface.

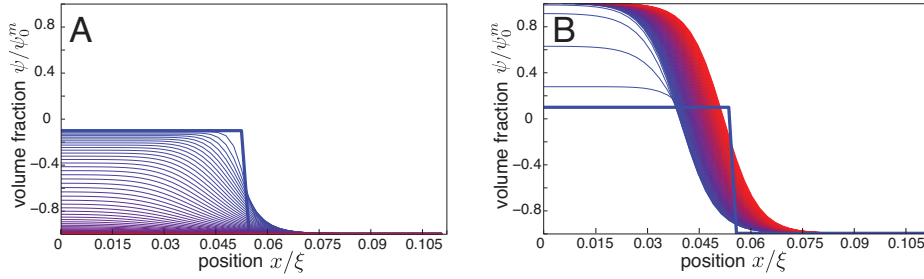


Figure 2.4: Numerical analysis of propagating interfaces in the Ginzburg-Landau free energy in the presence of an external field ($h = 0.01\sqrt{\epsilon^3/c}$). The profile of the volume fraction as a function of distance is shown for different times in different colors (from blue to red). The initial configuration is shown by the bold blue curves, for them $\psi = \psi_1^m$ everywhere except in a small region near the left edge where $\psi = \Delta\psi$. (A) The disturbance amplitude $\Delta\psi$ is relatively small and the system rapidly returns to the homogenous state $\psi = \psi_1^m$. The time interval between two consequent frames is $1 (\eta\epsilon)^{-1}$. (B) The initial disturbance amplitude $\Delta\psi$ is relatively large. The time interval between two consequent frames is $10 (\eta\epsilon)^{-1}$.

2.1.3 Driven interfaces

Now we consider an out of equilibrium limit of the Ginzburg-Landau free energy. An external field h breaks the degeneracy of the equilibrium free energy

$$f = -\frac{\epsilon}{2}\psi(\mathbf{r})^2 + \frac{c}{4}\psi(\mathbf{r})^4 + \frac{B}{2}|\nabla\psi(\mathbf{r})|^2 - h\psi(\mathbf{r}) . \quad (2.12)$$

Here we consider a small external field, $h^2 \ll \epsilon^3/c$, therefore, we expect near-equilibrium solutions. In a homogenous situation, where $\nabla^2\psi(\mathbf{r})$ has no contribution, the derivative of the free energy with respect to ψ is

$$\frac{\delta f}{\delta\psi} = -\epsilon\psi(\mathbf{r}) + c\psi(\mathbf{r})^3 - h . \quad (2.13)$$

As far as $h^2 < 4\epsilon^3/(27c)$, two independent distinct phases minimize this free energy. The volume fractions minimizing the free energy modify to $\psi_1^m \simeq -(\epsilon/c)^{1/2} + h/(2\epsilon)$ and $\psi_2^m \simeq (\epsilon/c)^{1/2} + h/(2\epsilon)$ up to the first order changes in h . Figure 2.3A shows the free energy as a function of the volume fraction ψ . Since the free energy of the two minima are different, it is not possible to have a two-phase equilibrium configuration.

We consider a simple case like the equilibrium condition, while far from the interface two distinct phases exist, but close to the interface these two phases are mixed. The interface is normal to the x -axis and there is no anisotropy along the interface. In the non-equilibrium state the interface moves with a velocity in x direction. Since the system is considered to be very large, the interface velocity v is constant and we expect traveling wave solutions $\psi(x, t) = \psi(x - vt)$. Different possible mechanisms may govern

the dynamics of the system. We can consider the diffusive dynamics as

$$\frac{\partial \psi}{\partial t} = -\nabla \cdot J = \zeta \nabla^2 \frac{\delta f}{\delta \psi}, \quad (2.14)$$

where J is the relative flux and is proportional to $-\nabla \frac{\delta f}{\delta \psi}$ by a coefficient ζ . This equation is known as the Cahn-Hilliard equation or model B which describes purely dissipative dynamics for a conserved variable [96]. However, there is no relevant traveling wave solution $\psi(x, t) = \psi(x - vt)$ for this type of dynamics [97]. The conservation of ψ with zero flux boundary conditions requires

$$\partial_t \int_{-\infty}^{\infty} \psi(x, t) dx = -v \int_{-\infty}^{\infty} \partial_x \psi(x - vt) dx = 0, \quad (2.15)$$

which can not be satisfied since ψ has different values at two infinities.

One other possible dynamic model, referred as model A or Glauber model, describes the time-dependent Ginzburg-Landau energy [96]

$$\frac{\partial \psi}{\partial t} = -\eta \frac{\delta f}{\delta \psi} = \eta (\epsilon \psi(x) - c \psi(x)^3 + B \nabla^2 \psi(x) + h), \quad (2.16)$$

where η is a constant which is related to the friction coefficients. Despite the model B, model A does not describe a conserved field and equation 2.15 does not need to be valid. This can especially be relevant for active systems.

We expect a traveling wave solution $\psi(x, t) = \psi(u)$, where $u = x - vt$ and two distinct phases exist at two infinities on both sides of the interface. The Taylor expansion of the volume fraction as a function of the external field can be written as

$$\psi(u) = \psi_0(u) + \sum_n \frac{h^n}{n!} \psi_n(u). \quad (2.17)$$

Here $\psi_0(u)$ is what describes the equilibrium case, $\psi_0(u) = (\epsilon/c)^{1/2} \tanh(u/\xi)$. The other coefficients $\psi_n(u)$ describe the higher order terms. For small values of the external field h , we use the first order expansion $\psi(u) \simeq \psi_0(u) + h \psi_1(u)$. Replacing $\psi_0(u)$, we can solve equation 2.16 to calculate $\psi_1(u)$. Taken together the volume fraction is

$$\psi(x, t) \simeq \sqrt{\frac{\epsilon}{c}} \tanh\left(\frac{u}{\xi}\right) + \frac{h}{2\epsilon}, \quad (2.18)$$

and the interface velocity is given by

$$v = \frac{3h\eta}{2\epsilon} \sqrt{2Bc}. \quad (2.19)$$

Furthermore, we can analyze numerically whether this solution is relevant. We consider a homogenous initial condition $\psi(x) = \psi_1^m$, where ψ_1^m corresponds to the local minimum with higher free energy. We perturb it by imposing $\psi = \Delta\psi$ in a small localized region near the left edge (figure 2.4A). We solve equation 2.16 numerically to calculate the

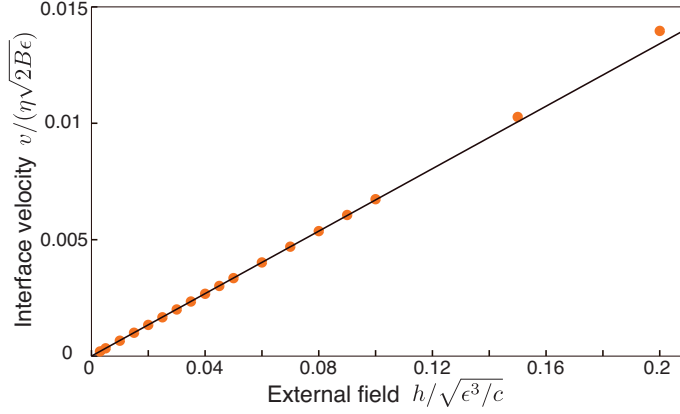


Figure 2.5: The normalized velocity of the traveling wave as a function of the normalized external field for a non-equilibrium Ginzburg-Landau energy. The black line represents the analytical approximation up to first order in the external field and the points show the velocities calculated numerically.

evolution of ψ profile. If the disturbance amplitude is small $\Delta\psi < \psi_M$, the system will rapidly return to the homogenous state where $\psi = \psi_1^m$ everywhere (figure 2.4A). For relatively higher values of the disturbance amplitude $\Delta\psi > \psi_M$, the other phase $\psi = \psi_2^m$, the local minimum with lower energy, emerges on the left side (figure 2.4B). Here ψ_M is the crossover volume fraction and its value is set by the position of the energy barrier, which is close to $\psi_M \simeq 0$. After the rapid response, the interface keeps an unchanged profile and moves with a constant velocity. The interface profile is very similar to the analytical solution (equation 2.18). We compare the interface velocity between the analytical and numerical solutions for different strengths of the external field in figure 2.5. For small values of the external field $h < 0.1\epsilon^{3/2}/c^{1/2}$ the analytical approximation fits very well with the numerical result. However, the first order approximation fails for larger values of h , when higher order terms in equation 2.17 become important.

We study the profile of energy and anisotropic stress for the analytical solutions to determine the interfacial tension. Figure 2.3B shows that the free energy reaches two different values at both sides far from the interface. This makes it complicated to calculate the interfacial tension from the free energy profile since there is no unique value for the bulk free energy f_0 (equation 2.11). Interestingly, we can calculate it from the profile of the anisotropic stress. Using the Erikson stress tensor described in appendix A, the anisotropic stress is $\tilde{\sigma} = B(\partial_x\psi)^2/2$. The anisotropic stress vanishes far from the interface and therefore the interfacial tension is

$$\gamma = 2 \int_{-\infty}^{+\infty} \tilde{\sigma}(x) dx = \frac{4}{3} \frac{B}{c} \epsilon. \quad (2.20)$$

This is the same as the interfacial tension in equilibrium condition, implying that the external field does not change the interfacial tension in the first order approximation.

2.2 Continuum description of cellular compartments in growing tissues

In this section we develop a coarse-grained description of cellular compartments in growing tissues. This model is based on the balance of cell numbers and forces. We first explain how to derive dynamic equations by taking into account the active terms. We then study the propagation of the interface between two cell populations due to the difference between the homeostatic pressure of cells.

2.2.1 Cell number balance and momentum conservation

We consider a tissue composed of two types of cells represented by A and B . Cell number density of these populations are described by $n_A = n_A(\mathbf{r}, t)$ and $n_B = n_B(\mathbf{r}, t)$. For each component cell number is balanced by cell division and apoptosis

$$\begin{aligned}\partial_t n_A + \partial_\alpha (v_\alpha^A n_A) &= (k_d^A - k_a^A) n_A, \\ \partial_t n_B + \partial_\alpha (v_\alpha^B n_B) &= (k_d^B - k_a^B) n_B.\end{aligned}\quad (2.21)$$

Here \mathbf{v}^A and \mathbf{v}^B are the local velocities of the corresponding cells and $k_d^{A,B}$ and $k_a^{A,B}$ are division and apoptosis rates of A or B cells.

For such a two component system $n_A \Omega_A + n_B \Omega_B = 1$, where Ω_A and Ω_B are the volume of cells of type A and B . We can introduce the volume fraction of A cells as $\varphi = n_A \Omega_A$. The average velocity \mathbf{v} and the relative flux \mathbf{J} are defined as

$$\begin{aligned}v_\alpha &= \varphi v_\alpha^A + (1 - \varphi) v_\alpha^B, \\ J_\alpha &= (v_\alpha^A - v_\alpha^B) \varphi (1 - \varphi).\end{aligned}\quad (2.22)$$

Considering these relations, we can rewrite the balance equations of cell numbers. The divergence of the average velocity is given by

$$\begin{aligned}\partial_\alpha v_\alpha &= k^A \varphi + k^B (1 - \varphi) + J_\alpha \partial_\alpha (\ln \Omega_A - \ln \Omega_B) \\ &+ \varphi (\partial_t + v_\alpha \partial_\alpha) \ln \Omega_A + (1 - \varphi) (\partial_t + v_\alpha \partial_\alpha) \ln \Omega_B,\end{aligned}\quad (2.23)$$

where k^A and k^B are the effective production rates of A and B cells, $k^{A,B} = k_d^{A,B} - k_a^{A,B}$. The other equation describes the dynamics of the volume fraction

$$\begin{aligned}\partial_t \varphi + v_\alpha \partial_\alpha \varphi + \partial_\alpha J_\alpha &= \varphi (1 - \varphi) (k^A - k^B) + \varphi (1 - \varphi) (\partial_t + v_\alpha \partial_\alpha) (\ln \Omega_A - \ln \Omega_B) \\ &+ J_\alpha (\varphi \partial_\alpha \ln \Omega_B + (1 - \varphi) \partial_\alpha \ln \Omega_A).\end{aligned}\quad (2.24)$$

Equations 2.23 and 2.24 represent the comprehensive form of balance of cell numbers in a two component tissue. In general, cell volumes Ω_A and Ω_B are not constant and may depend on local pressure. However, for simplicity, we consider an incompressible limit where the volume of cells are constant. In this limit equation 2.23 can be simplified as

$$\partial_\alpha v_\alpha = k^A \varphi + k^B (1 - \varphi).\quad (2.25)$$

In this respect the dynamics of the volume fraction is given by

$$\partial_t \varphi + v_\alpha \partial_\alpha \varphi + \partial_\alpha J_\alpha = \varphi(1 - \varphi)(k^A - k^B). \quad (2.26)$$

To satisfy the conservation of momentum, the divergence of the stress tensor should be balanced by external forces $\nabla \cdot \sigma = \mathbf{f}^{\text{ext}}$. For instance, if the tissue lies on a substrate the force balance reads

$$\nabla \cdot \sigma = \mu \mathbf{v}, \quad (2.27)$$

where μ is the friction coefficient. The total stress tensor σ includes different terms describing elasticity and viscosity of cells, and the activity of tissue, as well as the interfacial interaction between different types of cells. According to tissue properties, the stress tensor can be simplified [73, 74]. We consider a simplified version of stress tensor, describing the tissue as a viscous fluid

$$\sigma_{\alpha\beta} = -P\delta_{\alpha\beta} + \eta(\partial_\alpha v_\beta + \partial_\beta v_\alpha - \frac{1}{d}\partial_\gamma v_\gamma) - B(\partial_\alpha \varphi \partial_\beta \varphi - \frac{1}{d}\partial_\gamma \varphi \partial_\gamma \varphi). \quad (2.28)$$

The first term describes total pressure which can be considered as a Lagrange multiplier to satisfy the incompressibility condition. The second term describes dissipative viscosity stress, where η is the shear viscosity coefficient. The last term accounts for the anisotropic stress originating from the interfacial interaction between A and B cells, which is based on equation 2.7.

In general the effective cell division rates k^A and k^B depend on local pressure. Their relation can be expanded to the first order near the homeostatic pressure $k^{A,B} = \kappa(P_h^{A,B} - P)$ [67]. Here κ is a constant which, for simplicity, is considered to be equal for cells of type A and B . With this assumption we can rewrite equation 2.25 and derive pressure as a function of the volume fraction and velocity field

$$P = P_h^A \varphi + P_h^B (1 - \varphi) - \frac{\partial_\gamma v_\gamma}{\kappa}. \quad (2.29)$$

2.2.2 Propagating interfaces between two cell populations

We are interested in the propagation of an interface between two cell populations. We consider a thin tissue and average cell densities and stresses in the z direction to have an effective two-dimensional tissue. The tissue lies on a substrate and a friction force is applied to the tissue by the substrate. In a 2D picture, the tissue is symmetric along the interface (y direction) and its properties change only in the perpendicular direction (x direction). Cell populations are at their respective homeostatic states and at rest far from the interface, $\varphi = 1$ at $x = -\infty$ and $\varphi = 0$ at $x = \infty$. Near the interface two cell types are mixed, $0 < \varphi < 1$. When the homeostatic pressure of A and B cells are different, the interface moves due to the different division rates of two cell populations in the vicinity of the interface. Here we analyze the dynamics of such a two-component tissue. For a thin film in one dimension, the dynamics of the volume fraction is determined by

$$\partial_t \varphi + v_x \partial_x \varphi - D \partial_x^2 \varphi = \kappa \Delta P_h \varphi (1 - \varphi). \quad (2.30)$$

Here $\Delta P_h = P_h^A - P_h^B$. We also assumed that the relative flux is driven by diffusion $\mathbf{J} = -D\nabla\varphi$, where D is the diffusion constant. We then use the force balance equation to calculate the velocity field

$$\left(\frac{1}{\kappa} + \eta\right)\partial_x^2 v_x - \Delta P_h \partial_x \varphi - \frac{B}{2}\partial_x^2 \varphi \partial_x \varphi = \mu v_x . \quad (2.31)$$

Equations 2.30 and 2.31 characterize tissue dynamics. Equation 2.30 is a generalized version of the Fisher wave equation with an additional convection term which accounts for mechanical feedback in cell number balance. We discuss later some special cases where this equation can be described by the Fisher wave.

We can write the dimensionless form of the characteristic equations. We use the characteristic interface width $\ell_0 = (D/(\Delta P_h \kappa))^{1/2}$ and the time scale $\tau = 1/(\Delta P_h \kappa)$ for normalizing length and time in the dynamics equations. Using normalized time $T = t/\tau$ and length $X = x/\ell_0$ equation 2.30 can be written as

$$\partial_T \varphi + V \partial_X \varphi - \partial_X^2 \varphi = \varphi(1 - \varphi) . \quad (2.32)$$

In this framework, the dimensionless form of equation 2.31 is

$$\Lambda^2 \partial_X^2 V - \alpha \partial_X \varphi (1 + \beta \partial_X^2 \varphi) = V . \quad (2.33)$$

The dimensionless parameters $\Lambda^2 = (1 + \kappa\eta)\Delta P_h/(D\mu)$, $\alpha = \Delta P_h/(D\mu)$, and $\beta = B\kappa/D$ characterize the tissue dynamics. Equation 2.33 can be integrated in order to calculate V , using a Green's function approach,

$$V(X, T) = -V_0 \int_{-\infty}^{\infty} dX' e^{-\frac{|X-X'|}{\Lambda}} \partial_X \varphi(X', T) [1 + \beta \partial_X^2 \varphi(X', T)] . \quad (2.34)$$

Here $V_0 = \alpha/(2\Lambda)$ is a characteristic velocity. For $V_0 = 0$, equation 2.30 is the classical Fisher wave without advection. For long times the system reaches traveling wave solutions of the form $\varphi(X, T) = \varphi(U)$, where $U = X - CT$ and C is the wave speed. Starting from a localized initial condition, the classical Fisher wave moves with the wave speed $C_0 = 2$. This solution is a so-called pulled front solution for which the wave speed is determined by the linearized dynamics in the tail of the profile. Pulled front solutions can not have larger wave speeds than C_0 [98]. Interestingly, in the limit that $\Lambda \gg 1$, as far as β is not large, we can neglect the spacial variation of V compared to φ and consider $V\partial_X \varphi = V_0\partial_X \varphi$. Therefore, equation 2.32 is the Fisher equation in a moving frame. This equation has traveling wave solutions with the interface velocity $C = C_0 + V_0$. These solutions must be pushed fronts for which wave speed is determined by nonlinearities [98]. For large values of interfacial tension $\beta \gg \Lambda/\alpha$ this argument is not valid any more and wave velocity increases compared to the approximation $C_0 + V_0$.

Numerical results. We can solve equations 2.34 and 2.32 numerically in order to calculate the profiles of the volume fraction and the velocity field. We replace the velocity field V in equation 2.32 in order to determine the time evolution of the volume fraction

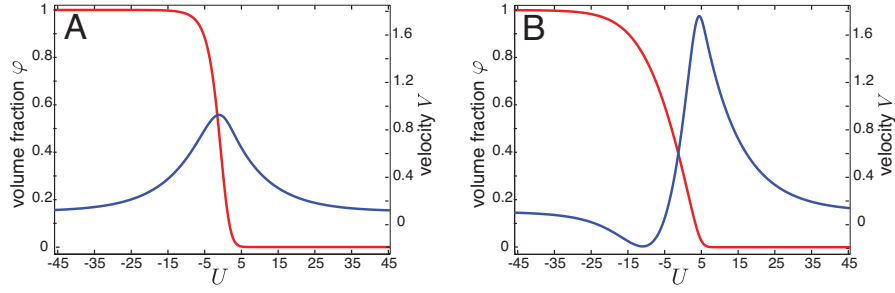


Figure 2.6: The profiles of the volume fraction (red) and the normalized velocity (blue) for the traveling wave between two cell populations. The characteristic parameters are $\Lambda = 10$, $V_0 = 2$, for two choices of the interfacial tension (A) $\beta = 0$, and (B) $\beta = 1000$.

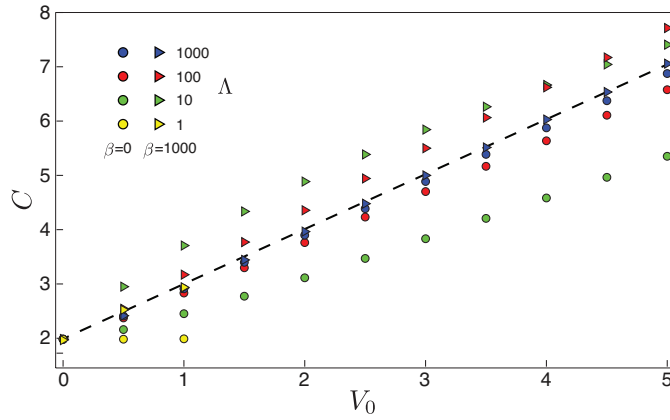


Figure 2.7: The velocity of the traveling waves as a function of the dimensionless parameter V_0 . Different colors depict different values of Λ , for two choices of the interfacial tension $\beta = 0$ (circles) and $\beta = 1000$ (triangles). The dashed black line represent the approximation $C = C_0 + V_0$.

φ . Starting from a localized initial configuration, the interface evolves to a stationary profile $\varphi(U)$ for long times which travels with the wave speed C . Figure 2.6 shows two examples of the profile of the volume fraction and velocity field for two choices of the characteristic dimensionless parameters. The dimensionless wave speed C is shown in figure 2.7 for different choices of the characteristic parameters Λ , α , and β . Our numerical results confirm the simple Fisher wave limit where the advective velocity V_0 adds up to the minimum wave speed C_0 .

Linear analysis. Moving front solutions with wave speed C can also be obtained as profiles of $\varphi(U)$ and $V(U)$ that solve equations 2.34 and 2.32. We analyze the behavior of such solutions in the front region where the linear theory is valid. For simplicity we assume that $\beta = 0$, but this analysis can be generalized when $\beta > 0$. To describe the phase plane we need four parameters φ , $\varphi' = \partial_U \varphi$, V , $V' = \partial_U V$. The dynamics

equations are given by

$$\begin{aligned}
\partial_U \varphi &= \varphi', \\
\partial_U \varphi' &= [(V - C)\varphi' - \kappa \Delta P^h \varphi(1 - \varphi)], \\
\partial_U V &= V', \\
\partial_U V' &= \Lambda^{-1}[V + \alpha \varphi'].
\end{aligned} \tag{2.35}$$

The fixed points are $(\varphi = 0, \varphi' = 0, v = 0, v' = 0)$ and $(\varphi = 1, \varphi' = 0, v = 0, v' = 0)$. We linearize equations 2.35 near the first fixed point which represents the unstable front

$$\begin{bmatrix} \partial_U \varphi \\ \partial_U \varphi' \\ \partial_U V \\ \partial_U V' \end{bmatrix} = - \begin{bmatrix} 0 & -1 & 0 & 0 \\ 1 & C & 0 & 0 \\ 0 & 0 & 0 & -1 \\ 0 & -\alpha/\Lambda^2 & -1/\Lambda^2 & 0 \end{bmatrix} \begin{bmatrix} \varphi \\ \varphi' \\ V \\ V' \end{bmatrix}. \tag{2.36}$$

The eigenvalues of this matrix are

$$\begin{aligned}
\lambda_1 &= C/2 - \sqrt{(C/2)^2 - 1}; & \lambda_3 &= 1/\Lambda; \\
\lambda_2 &= C/2 + \sqrt{(C/2)^2 - 1}; & \lambda_4 &= -1/\Lambda.
\end{aligned} \tag{2.37}$$

In order to have real eigenvalues, the wave velocity should be larger than a critical value $C > 2$. The corresponding eigenvectors are

$$\begin{aligned}
\mathbf{z}_1 &= \begin{bmatrix} \lambda_2(1 + \Lambda^2(1 - C\lambda_1)) \\ -1 + (\lambda_1\Lambda)^2 \\ \alpha \\ -\alpha\lambda_1 \end{bmatrix}; & \mathbf{z}_3 &= \begin{bmatrix} 0 \\ 0 \\ -\Lambda \\ 1 \end{bmatrix}; \\
\mathbf{z}_2 &= \begin{bmatrix} \lambda_1(1 + \Lambda^2(1 - C\lambda_2)) \\ -1 + (\lambda_2\Lambda)^2 \\ \alpha \\ -\alpha\lambda_2 \end{bmatrix}; & \mathbf{z}_4 &= \begin{bmatrix} 0 \\ 0 \\ \Lambda \\ 1 \end{bmatrix}.
\end{aligned} \tag{2.38}$$

Therefore, the system phase near the front tail can be expanded as

$$\mathbf{Z} = \sum_i d_i \mathbf{z}_i \exp(-\lambda_i U), \tag{2.39}$$

where d_i are constant coefficients. This allows us to write the profiles of the volume fraction and velocity as following

$$\begin{aligned}
\varphi(U) &= \varphi_1 \exp(-\lambda_1 U) + \varphi_2 \exp(-\lambda_2 U), \\
V(U) &= V_1 \exp(-\lambda_1 U) + V_2 \exp(-\lambda_2 U) + V_3 \exp(-\lambda_3 U).
\end{aligned} \tag{2.40}$$

Here we took into account that the fourth eigenvalue does not describe a decaying function and is irrelevant. We used constant coefficients φ_i and V_i which are given by $\varphi_i = d_i z_{i,1}$, $V_i = d_i z_{i,3}$.

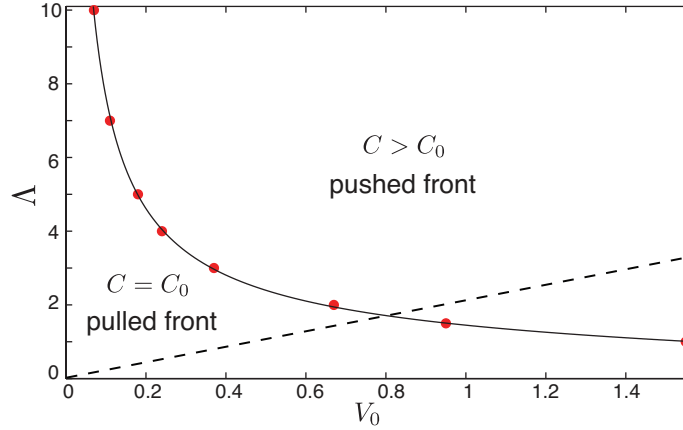


Figure 2.8: The state diagram of front propagation as a function of the dimensionless parameters Λ and V_0 , when $\beta = 0$. The red dots are the measured transition points between the pushed and pulled fronts. The black curve is an interpolation of these data points. The unphysical sets of parameters is below the dashed line $V_0 < \Lambda/2$.

For localized initial conditions, the system either reaches a pulled front solution with $C = C_0$ and $\lambda_1 = \lambda_2 = 1$ or a pushed front solution with $C > C_0$ and $\varphi_1 = 0$ such that the tail is given by $\varphi(U) \simeq \varphi_2 e^{-\lambda_2 U}$. The requirement $\varphi_1 = 0$ selects the wave speed C in the pushed front solutions. This analysis allows us to distinguish pulled front solutions from pushed fronts in our numerical study. We observe that for a particular range of parameter (Λ and V_0), the wave velocity equals to the linear velocity $C = C_0$. In this pulled fronts regime, propagation is dominated by diffusion as the Fisher wave without advection, independent of V_0 . In the other regime, the interface propagation is influenced by tissue mechanics. The advective fluxes caused by increased cell proliferation behind and apoptosis in front of the leading edge propel the interface with a larger speed $C > C_0$. In this pushed front regime, the decay length of the φ tail is set by λ_2 . Figure 2.8 shows regions where pulled and pushed fronts occur for $\beta = 0$ as a function of V_0 and Λ . For a given value of Λ , interface propagation is described by a pulled front if $V_0 = 0$. Increasing V_0 the velocity remains unchanged until a critical value, beyond that the front is pushed by nonlinearities and moves at an increased speed C that depends on V_0 in this advection dominated regime. This critical value describes the transition between pulled and pushed fronts which is calculated numerically for different values of Λ (figure 2.8).

2.3 Summary

In this chapter we analyzed the dynamics of interfaces in passive and active tissues. In the first section we studied the interfacial phenomena in a passive fluid. In a mean field approach, a binary fluid can be described with the Ginzburg-Landau free energy. Two distinct volume fractions minimize this free energy. At thermal equilibrium two energy minima have equal energies and can coexist. We analyzed the phase separation problem

in a 2D system which is infinitely large and symmetric along the interface. The volume fraction reaches two distinct equilibrium values far from the interface and the interface between them is identified by a special mixed profile of the volume fraction. When an external field breaks the symmetry of the system, such an equilibrium two-component phase does not exist anymore. In this situation one of the minima has less free energy and is more stable. In a two component fluid a traveling wave solution exists where the interface propagates with a velocity proportional to the external field. We investigated the dynamics of this system numerically, and analytically up to first order approximation. We analyzed the stress profile in the two-component fluid in both equilibrium and out of equilibrium situations. The anisotropic stress shows a specific profile near the interface. We calculated the effective interfacial tension integrating anisotropic stress along a line perpendicular to the interface. This will be used later to calculate interfacial tension for interfaces in the vertex model.

We discussed the basic concepts of a continuum model to describe cellular compartments in active tissues. The balance of cell numbers is modified by source terms, which originate from cell division and apoptosis. The equation of cell number balance is coupled to the stress profile. We studied the interesting case where two cell populations with different homeostatic pressure meet. As a result, the interface propagates due to the difference in the homeostatic pressures of two cell types. This front propagation is described by a generalized version of the Fisher wave, which includes the effects of tissue mechanics. We solved the equations numerically to calculate the front shape and the wave velocity as a function of the characteristic parameters. We discussed the analytical solutions by linearizing the equations near the unstable front. We showed that both pulled and pushed front solutions occur depending on parameter values. In the pulled front solutions the interface propagation is dominated by diffusion, however, convection drives interface dynamics in the pushed fronts.

Chapter 3

Mechanics of growing tissues in a vertex model

In this chapter we use a vertex model to describe the mechanics of cellular networks. In section 1.4.2 we introduced vertex models to study epithelia in the cellular scale. These models describe the network of adherens junctions which characterizes the shape of cells in epithelia (figure 1.1). In these models each cell is represented by a polygon and cell bonds are shared between neighboring cells (see section 1.4.2 and figure 1.8). Here we describe the vertex model developed in [2]. This model describes the elasticity of cells and tension and adhesion along cell bonds. We first analyze the mechanics of cellular networks and then describe tissue dynamics in the vertex model.

3.1 Work function for polygonal cell packing

Tissue development is influenced by different processes which operate on distinct time scales. In particular a cell network relaxes in response to perturbations on time scales of several seconds to minutes, whereas cell division takes place within several hours. Therefore on the time scales of cell division, the adherens junctional network can be described as a stable network. Balanced network configurations are determined as minima of a work function with respect to the position of all vertices

$$E = \frac{K}{2} \sum_{\alpha=1}^{N_c} (A_{\alpha} - A_{\alpha}^{(0)})^2 + \sum_{\langle ij \rangle} \Lambda_{ij} \ell_{ij} + \frac{\Gamma}{2} \sum_{\alpha=1}^{N_c} L_{\alpha}^2 - f_x L_x - f_y L_y . \quad (3.1)$$

Here K describes the cell area elasticity, $A_{\alpha}^{(0)}$ is the preferred area and A_{α} is the area of cell α . We choose $A_{\alpha}^{(0)} = A^{(0)}$ for all cells which are not undergoing cell division. The summation is over all the cells where N_c is the total number of cells. The mechanical tension on cell bonds $\langle ij \rangle$, where i and j are two adjacent vertices, is illustrated by Λ_{ij} . ℓ_{ij} is the length of the corresponding bond. Λ_{ij} can be considered as the combination of cell bond tension and the adhesive interaction between the neighboring cells sharing the

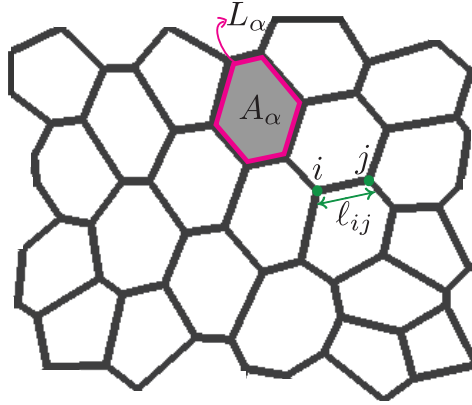


Figure 3.1: Cellular geometry in the vertex model. Shape of cells is described by a two-dimensional network of polygons. A_α and L_α are respectively the area and perimeter of cells indexed by α . l_{ij} is the cell bond of length connecting the vertices i and j .

bond. The perimeter of cell α is L_α and Γ denotes the perimeter elasticity. This term originates from the contractile actin-myosin ring accumulated around the cell perimeter. f_x and f_y are the external forces applied to the whole tissue in x and y directions. To describe the system, we use a rectangular box with periodic boundary conditions. L_x and L_y represent the system size in x and y directions, respectively.

The network is characterized by two dimensionless parameters $\bar{\Lambda} = \Lambda/(KA^{(0)})^{3/2}$ and $\bar{\Gamma} = \Gamma/(KA^{(0)})$ which define the phase diagram of the system. Depending on the value of these parameters, tissues may respond as solids or as soft materials. We apply an external shear stress $\tilde{\Sigma}$ by considering the external forces to be proportional to the tissue size $f_x = -\tilde{\Sigma}L_y$ and $f_y = \tilde{\Sigma}L_x$. In our study we use the normalized shear stress $\bar{\Sigma} = \tilde{\Sigma}/(KA^{(0)})$.

3.2 Time evolution of cellular networks

The dynamics of cellular networks is generated by topological changes including cell division and junctional remodelings. For dividing a cell we double its preferred area in a quasi-static way. We next introduce a new bond passing the geometric center of the cell (figure 3.2). The direction of the new bond determines the orientation of cell division. Moreover, we consider two categories of tissue remodeling, named T1 and T2 transitions. In a T1 transition a short cell bond shrinks and expands in the opposite direction. The number of cell neighbors are changed for the four involved cells (figure 3.3A). Furthermore, a small triangle shrinks and is replaced by a vertex, called a T2 transition (figure 3.3B). After any topological change the network is relaxed to a new minimized energy configuration.

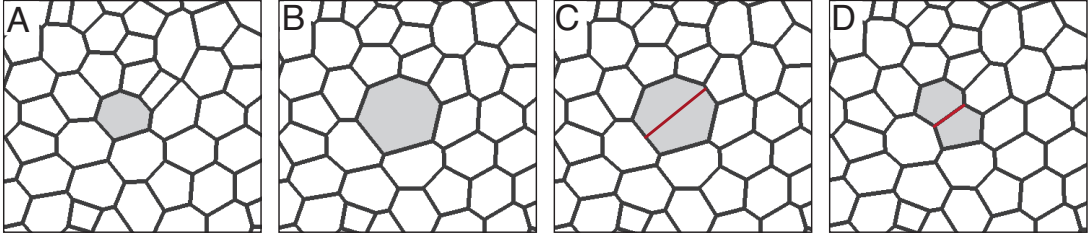


Figure 3.2: Cell division in the vertex model. (A) One cell is chosen randomly to divide (shaded in gray). (B) The preferred area of the cell is doubled. (C) A new bond (colored in red) is introduced in a random direction passing the geometric center of the cell. (D) The cellular network is relaxed to a new minimum of the work function.

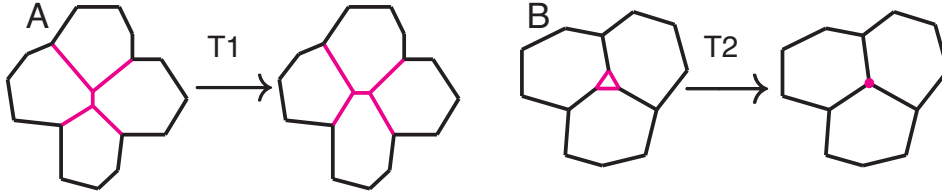


Figure 3.3: Junctional remodeling in the vertex model. (A) T1 transition describes the shrinkage of a cell bond and its expansion in the opposite direction. (B) T2 transition represents the contraction of a small triangle to a vertex.

3.3 Models for cell division

We model the growth of tissues by introducing stochastic cell divisions. During each step one cell division occurs. Cell α is chosen with the probability p_α to divide, where $\sum_{\alpha=1}^{N_c} p_\alpha = 1$. Each cell divides with the same probability $p_\alpha = 1/N_c$ if cell division rate is equal for all the cells. However, in general the probability of cell division may be influenced by cell properties.

We explained in the previous section that the direction of the new bond φ sets the division axis. A function $p(\varphi)$ denotes the probability distribution of the direction of the new bond φ . For unbiased cell division, the direction of the new bond is chosen randomly $p(\varphi) = 1/\pi$. Later, we discuss the cases where the probability of cell division depends on cell pressure and where the direction of the new bond is biased by anisotropy in cell shape.

3.3.1 Division rate depending on cell pressure

The division rate of cells can be controlled by different factors, like the concentration of different signaling molecules or mechanical properties of cells [99]. We are interested in

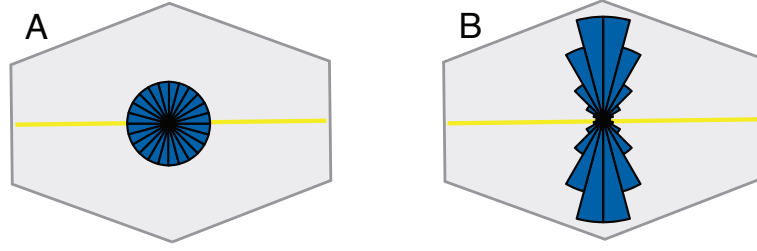


Figure 3.4: A scheme representing the probability distribution of the orientation of cell division. (A) Cell division is unbiased. (B) The division orientation is biased by cell elongation. The orientation probabilities are shown by bars for different angle intervals. The yellow line shows the axis of cell elongation.

the possible mechanical feedbacks that affect growth patterns. It is well known that cell growth is inhibited by cell compression [72, 100]. Here we analyze the general case that cell proliferation is influenced by cell pressure.

In case of no external pressure the average cell pressure is zero. However cells have different shapes and this leads to fluctuations in cell pressure. This effect would control cell proliferation so that cells with higher pressure divide with lower probability and conversely cells with lower pressure divide with higher probability. The fluctuations in cell pressure change the probability of cell division locally, but the division rate will be homogenous in average throughout the tissue. We consider the situation where the probability of cell division p_α depends on the cell pressure P_α as

$$p_\alpha = \frac{1}{Z} e^{-\epsilon \frac{P_\alpha}{KA^{(0)}}} . \quad (3.2)$$

Where ϵ describes the strength of this effect and Z is the partition function

$$Z = \sum_{\alpha=1}^{N_c} e^{-\epsilon \frac{P_\alpha}{KA^{(0)}}} . \quad (3.3)$$

Here $KA^{(0)}$ is used for normalizing the cell pressure P_α . We will introduce the stress tensor of cells in the vertex model in section 3.4.2. Cell pressure can be obtained from the trace of stress tensor.

3.3.2 Oriented cell division

It is observed that in many developing tissues the orientation of the mitotic cleavage plane is not completely random and is influenced by the cell geometry [75, 76]. The cleavage plane bisects dividing cells perpendicular to their long axis (figure 3.4B). In particular this correlation between cell elongation and orientation of cell cleavage plane is observed and quantified for the *Drosophila* wing disc [76].

In our division model we choose the new bond direction φ with the probability

$$p(\varphi) = \frac{1}{Z} e^{\delta \text{Tr}(\tau_\alpha \cdot M_\varphi)}, \quad (3.4)$$

where τ_α is a symmetric traceless tensor representing the elongation of cell α (see appendix C). The effect of cell elongation on the division axis is described by a coefficient δ . Division orientation is unbiased when $\delta = 0$ (figure 3.4A). The normalization factor is given by $Z = \int e^{\delta \text{Tr}(\tau_\alpha \cdot M_\varphi)} d\varphi$. The tensor M_φ describes the orientation of the new bond

$$M_\varphi = \begin{pmatrix} \cos 2\varphi & \sin 2\varphi \\ \sin 2\varphi & -\cos 2\varphi \end{pmatrix}. \quad (3.5)$$

3.4 Stresses in cellular networks

In this section, we introduce stresses in two dimensional networks of cells. Here we calculate stress components in a phenomenological way based on the model concepts and force balance. In the absence of external forces, the divergence of stress tensor should vanish to satisfy force balance

$$\partial_j \sigma_{ij} = 0. \quad (3.6)$$

The stress tensor defined here, σ_{ij} , is not unique and can be transformed in such a general form

$$\sigma_{ij}^N = \sigma_{ij} + \partial_k \chi_{ijk}, \quad (3.7)$$

where χ_{ikl} is an arbitrary tensor which is antisymmetric in the last two suffixes $\chi_{ijk} = -\chi_{ikj}$. The new stress tensor σ_{ij}^N and the old one σ_{ij} satisfy the same force balance equation [101].

3.4.1 Stress tensor in the vertex model

Here we present our method to quantify stress tensor in cellular networks described by the vertex model. In a two dimensional picture the stress components have the dimension of energy per area. Inside each cell the stress tensor is a diagonal tensor

$$\sigma_{ij} = -P_\alpha^A \delta_{ij}, \quad (3.8)$$

where P_α^A is called the area pressure of cell α . In the vertex model the area pressure is the stress associated with the changes of cell area due to the area elasticity of cells

$$P_\alpha^A = -K (A_\alpha - A^{(0)}). \quad (3.9)$$

The stress tensor at cell bonds is more complicated. We consider a bond perpendicular to the x_1 -axis, and along the x_2 -axis (figure 3.5). This bond is shared between the cells α and β . We should consider the line tension and the contractility of cells

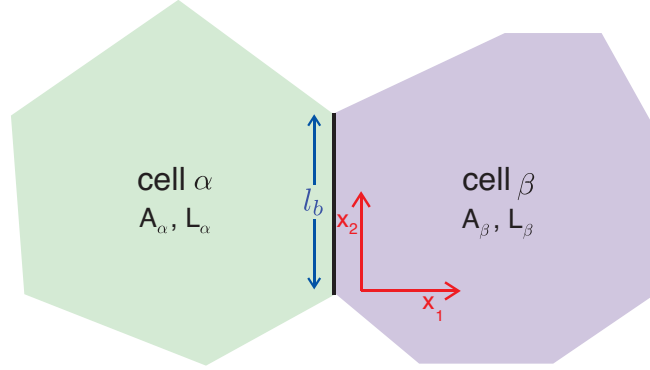


Figure 3.5: A scheme of two cells sharing a bond. The bond, represented by a black line with length l_b , is shared between cell α , with area A_α and perimeter L_α , and cell β , with area A_β and perimeter L_β . x_1 and x_2 axes represent the local coordinate system, perpendicular and parallel to the bond direction.

which leads to an anisotropic stress at the cell bonds. Such a term $T_b \delta(x_1)$ should be added to σ_{22} . Here $\delta(x_1)$ is the Dirac Delta function and T_b is the effective tension of the bond which includes both the line tension and the cell perimeter contractility of the neighboring cells

$$T_b = \Lambda_b + \Gamma(L_\alpha + L_\beta) . \quad (3.10)$$

Therefore we can summarize the stress tensor in the vicinity of the cell bond

$$\begin{aligned} \sigma_{11}^b &= -P_\alpha^A \theta(-x_1) - P_\beta^A \theta(x_1) , \\ \sigma_{22}^b &= -P_\alpha^A \theta(-x_1) - P_\beta^A \theta(x_1) + T \delta(x_1) , \\ \sigma_{12}^b &= \sigma_{21}^b = 0 . \end{aligned} \quad (3.11)$$

Here P_α^A and P_β^A are the area pressures of cell α and β introduced in equation 3.9. $\theta(x)$ is the Heaviside function

$$\theta(x_1) = \begin{cases} 0 & x_1 < 0 \\ 1 & x_1 > 0 \end{cases} . \quad (3.12)$$

The divergence of the stress tensor does not vanish as far as the pressures of two adjacent cells are different

$$\partial_1 \sigma_{11}^b + \partial_2 \sigma_{12}^b = -(P_\beta^A - P_\alpha^A) \delta(x_1) . \quad (3.13)$$

This is related to our assumption that cell bonds are straight lines. In the vertex model the bending rigidity of cell bonds is infinite, otherwise the bonds would bend due to the pressure difference at both sides (Laplace's law). Therefore other terms should be added

to the stress components on the cell bond to satisfy this constraint. Apart from that, we should take into account that the stress tensor has to be symmetric with respect to the middle of the cell bond. Requiring force balance and symmetry properties of the system, we calculate the stress tensor around the bond

$$\begin{aligned}\sigma_{11}^b &= -P_\alpha^A \theta(-x_1) - P_\beta^A \theta(x_1) , \\ \sigma_{22}^b &= -P_\alpha^A \theta(-x_1) - P_\beta^A \theta(x_1) + T \delta(x_1) + (P_\beta^A - P_\alpha^A) \left(\frac{l_b}{2} x_2 - \frac{x_2^2}{2} + c_1 \right) \delta'(x_1) , \\ \sigma_{12}^b &= \sigma_{21}^b = -(P_\beta^A - P_\alpha^A) \left(\frac{l_b}{2} - x_2 \right) \delta(x_1) .\end{aligned}\tag{3.14}$$

Where l_b is the bond length and $\delta'(x_1)$ is the derivative of the Dirac delta function. This is a symmetric stress tensor which satisfies torque balance since there is no external torque applying on the tissue. One can show that the force balance equations are also satisfied

$$\begin{aligned}\partial_1 \sigma_{11}^b + \partial_2 \sigma_{12}^b &= -(P_\beta^A - P_\alpha^A) \delta(x_1) + (P_\beta^A - P_\alpha^A) \delta(x_1) = 0 , \\ \partial_2 \sigma_{22}^b + \partial_1 \sigma_{21}^b &= -(P_\beta^A - P_\alpha^A) \left(\frac{l_b}{2} - x_2 \right) \delta'(x_1) + (P_\beta^A - P_\alpha^A) \left(\frac{l_b}{2} - x_2 \right) \delta'(x_1) = 0 .\end{aligned}\tag{3.15}$$

To complete this discussion, we need to study the validity of force balance at cell vertices as well. At the vertices the stress is a combination of stresses along cell bonds coinciding at the vertex. It has a complicated form and therefore more calculations are needed to analyze force balance at cell vertices (see appendix B for detailed calculations).

3.4.2 Cell average stress tensor

To avoid the singularities of delta functions we average the stress tensor for individual cells. The average stress of cell α is given by

$$\sigma_{mn}(\alpha) = \frac{1}{A_\alpha} \int_{A_\alpha} \sigma_{mn} dA .\tag{3.16}$$

We calculate the stress tensor in the global coordinate system (x, y) and use the indices m and n to distinguish it from the local coordinate system of cell bonds (x_1, x_2) represented by indices i and j . Cell average stress includes cell area pressure as well as the contribution of all the bonds of the cell

$$\sigma_{mn}(\alpha) = -P_\alpha^A \delta_{mn} + \frac{1}{A_\alpha} \sum_b S_{mn}^{b,\alpha} .\tag{3.17}$$

We call $S_{mn}^{b,\alpha}$ the bond stress integral, which describes the contribution of bond b to the total stress of cell α . The summation is over all the bonds of cell α .

For simplicity, we calculate the stress integral for each bond $S_{ij}^{b,\alpha}$ in its local coordinate system explained in figure 3.5. At the end, it will be transformed rotationally in

order to get $S_{mn}^{b,\alpha}$ in the global coordinate system. The stress integral is the integral of stress components over area in the vicinity of the cell bond

$$S_{ij}^{b,\alpha} = \int_0^{l_b} dx_2 \int_{\Delta x_1} dx_1 \sigma_{ij}^{b,\alpha} . \quad (3.18)$$

The area integral is written as the multiples of integrals over x_2 which goes along the bond from 0 to l_b and the integral in the perpendicular direction from the center of the bond to a small distance Δx_1 inside the cell α . The bond contribution to the cell stress $\sigma_{ij}^{b,\alpha}$ is given by

$$\begin{aligned} \sigma_{11}^{b,\alpha} &= 0 , \\ \sigma_{22}^{b,\alpha} &= T_{b,\alpha} \delta(x_1) - (P_\beta^A - P_\alpha^A) \left(\frac{l_b}{2} x_2 - \frac{x_2^2}{2} + c_1 \right) \delta'(x_1) , \\ \sigma_{12}^{b,\alpha} &= \sigma_{21}^{b,\alpha} = (P_\beta^A - P_\alpha^A) \left(\frac{l_b}{2} - x_2 \right) \delta(x_1) . \end{aligned} \quad (3.19)$$

Here $T_{b,\alpha}$ is the effective tension along the bond corresponding to contractility of cell α and half of the line tension of the bond

$$T_{b,\alpha} = \frac{1}{2} \Lambda_b + \Gamma L_\alpha . \quad (3.20)$$

Replacing $\sigma_{ij}^{b,\alpha}$ in equation 3.18, all the components of the bond stress integral vanish except $S_{22}^{b,\alpha} = T_{b,\alpha} l_b$. The bond stress tensor in the global coordinate system $S_{mn}^{b,\alpha}$ is found by a rotational transformation R

$$S_{mn}^{b,\alpha} = R_{mi} R_{nj} S_{ij}^{b,\alpha} ; \quad R = \begin{bmatrix} \cos \varphi_b & -\sin \varphi_b \\ \sin \varphi_b & \cos \varphi_b \end{bmatrix} . \quad (3.21)$$

Here φ_b is the angle of the local x_1 -axis with the global x -axis. In conclusion the average stress tensor of cell α can be written as

$$\begin{aligned} \sigma_{xx}(\alpha) &= -P_\alpha + \frac{1}{A_\alpha} \sum_b T_{b,\alpha} l_b \sin^2 \varphi_b , \\ \sigma_{yy}(\alpha) &= -P_\alpha + \frac{1}{A_\alpha} \sum_b T_{b,\alpha} l_b \cos^2 \varphi_b , \\ \sigma_{xy}(\alpha) &= \sigma_{yx}(\alpha) = \frac{1}{A_\alpha} \sum_b T_{b,\alpha} l_b \sin \varphi_b \cos \varphi_b . \end{aligned} \quad (3.22)$$

The trace of the stress tensor is the isotropic stress and represents total cell pressure

$$P_\alpha^{tot} = P_\alpha - \frac{1}{2A_\alpha} \sum_b T_{b,\alpha} l_b . \quad (3.23)$$

The remaining anisotropic part is a symmetric shear tensor

$$\tilde{\sigma}_\alpha = \frac{1}{2} \begin{bmatrix} -\sum_b T_{b,\alpha} l_b \cos 2\varphi_b & \sum_b T_{b,\alpha} l_b \sin 2\varphi_b \\ \sum_b T_{b,\alpha} l_b \sin 2\varphi_b & \sum_b T_{b,\alpha} l_b \cos 2\varphi_b \end{bmatrix} . \quad (3.24)$$

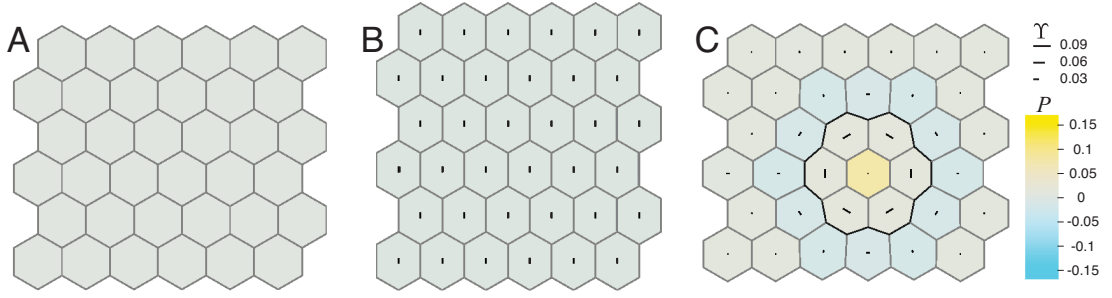


Figure 3.6: Examples of the stress profile in 2D cellular networks. The average cell stress is shown for individual cells. The color shows the average pressure for individual cells and the bars represent the direction and magnitude of the anisotropic stress Υ . Stress values are normalized by $KA^{(0)}$. For all cases we use $\bar{\Lambda} = 0.12$ and $\bar{\Gamma} = 0.04$. (A) A hexagonal network where all cells are identical. (B) A hexagonal network where all cells are identical and an external stress is applied to elongate tissue, $\bar{\Sigma} = 0.03$. (C) Cell bond tension is doubled at some bonds, shown in black, in a hexagonal network.

The shear tensor defines a magnitude of cell shear stress Υ , and a shear axis with an orientation angle Φ

$$\tilde{\sigma}_\alpha = \Upsilon \begin{bmatrix} \cos 2\Phi & \sin 2\Phi \\ \sin 2\Phi & -\cos 2\Phi \end{bmatrix}. \quad (3.25)$$

Stress profile and tissue properties. We can analyze the distribution of cell stresses in cellular networks for some simple examples. This helps us to understand the basic characteristics of cell stresses. To visualize the stress tensor, cell pressure is displayed with a color code and the shear stress is replaced with a bar describing shear magnitude Υ and shear axis orientation Φ . At first we look at a hexagonal network with identical cells. As we expect, cell pressure and cell shear stress vanish for all cells in the absence of external stresses (figure 3.6A). However, when an external stress is applied to the cellular network, the average cell stress will be nonzero and proportional to the magnitude of the external stress. In figure 3.6B an external shear stress $\bar{\Sigma} = 0.03$ stretches the tissue in y direction. Cells get elongated and cell average stress equals to the external stress.

Local changes in cell properties break the symmetries and produce local changes in the stress profile. For instance, if cell bond tension is increased locally at some cell bonds, cells are deformed near the bonds with increased tension and the stress is not homogeneous (figure 3.6C). However, the average stress of the whole cellular network vanishes since no external stress exists.

Cell division is an active process which disturbs the stress profile locally. Figure 3.7A shows an example when one cell division occurs in a network of hexagonal cells. Cell pressure and anisotropic shear stress of surrounding cells are modified by a cell division. The local anisotropic stress is governed by the orientation of cell division. However,

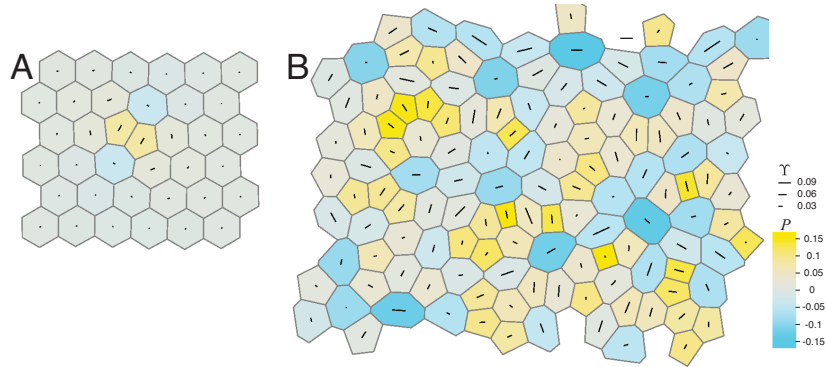


Figure 3.7: Stress profile changes during growth. Average cell stress is shown for individual cells. The color shows average pressure for individual cells and the bars represent the direction and magnitude of the anisotropic stress Υ . Stress values are normalized by $KA^{(0)}$. (A) One cell division occurs in the hexagonal network and disturbs the stress profile anisotropically. (B) A hexagonal network modifies to a network of random polygons of different classes after sequential cell divisions. Stresses are distributed randomly in such a network.

the average stress of the cellular network is zero since there is no external stress. We discussed in section 3.3 that growth is modeled by sequential stochastic cell divisions. Figure 3.7B shows the stress distribution in a cellular network after tens of cell division. In such a network the average stress is homogenous in the length scales bigger than the average bond length of cells.

3.5 Summary

In this chapter, we reviewed the basic concepts of a vertex model as an effective tool to study growth of epithelia. This model describes a 2D picture of epithelia where the shape of cells is determined by their apical junctional network. This model accounts for the area and perimeter elasticity of cells, adhesion and tension at cell bonds and external stresses. Tissue growth is introduced by stochastic cell divisions. We analyzed how to consider mechanical feedback in cell division algorithm. In particular we described the cases where the probability of cell division depends on cell pressure or the axis of cell division is influenced by the elongation of the cell.

Furthermore, we quantified the stress tensor in a two dimensional network of cells described by the vertex model. Stress components consist of different terms accounting for cell area pressure and contractility and tension along cell bonds, as well as the constraint that cell bonds are straight. The stress tensor satisfies force balance and includes singularities along cell bonds. We averaged the stresses for each cell in order to visualize the stress distribution in a cellular network. With some examples we showed

how the mechanical properties of the tissue, like cell bond tension and external stresses, change the stress profile. Furthermore the activity of cells influences the local distribution of stress. Cell division produces local active stresses whose anisotropy is set by division axis.

Chapter 4

Vertex model study of interface dynamics

Many developing tissues are organized into cellular compartments separated by boundaries, as highlighted in the introduction (section 1.2). Compartment boundaries keep sharp and straight morphologies during tissue growth. They play a crucial role in tissue development and it is important to investigate which mechanisms control their morphology. In this chapter, we introduce compartments in the cellular networks described by the vertex model. We analyze the general mechanisms by which compartment boundaries are shaped during growth phase. For example, we study the influence of cell bond tension, cell proliferation rate, cell elongation, and orientation of cell division on time-evolution behavior of compartment boundaries during tissue growth. In particular, we study how each mechanism affects stress distribution in the tissue and contributes to the effective interfacial tension. Furthermore, we quantify how the shape of interfaces evolves during tissue growth for each mechanism.

4.1 Cellular compartments in the vertex model

We first demonstrate how we study cellular lineage compartments in the vertex model. Two compartments of A and B cells are introduced in a cellular network. Each cell belongs to one compartment and divides into two daughter cells belonging to the same compartment. The daughter cells have the same characteristics as the mother cell does. The interface between two compartments consists of all cell bonds which are shared between two compartments.

In general, the properties of cells may be different within each compartment. This may be originated from the differences in the signaling molecules cells of each compartment express or respond to. On the other hand cells near the compartment boundaries may have specific characteristics. This is based on the intensive activity of genes and signals near the compartment boundaries. In the vertex model, mechanical properties of cells are described by cell area and perimeter elasticity, line tension along cell bonds, and external stresses (equation 3.1). In addition, cell division probability and orientation of

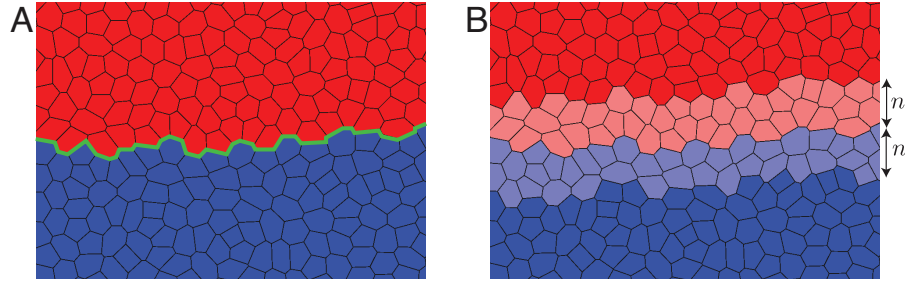


Figure 4.1: A scheme of local properties of cells near the interface between two compartments (blue and red). (A) Cell bond tension is increased along the interface with a factor λ (shown in green). (B) Cell division probability is reduced by a factor β within n cell rows on both sides of the interface (colored in light blue and light red).

cell division indicate division properties of cells.

Here we consider the cases where cells within two compartments have identical properties. This assumption is based on the experimental evidences that cell mechanics and morphology are indistinguishable within two compartment far from the boundaries [4, 102]. However, cells near the compartment boundaries show distinct characteristics. In particular, we consider the situation where the bond tension is constant for all cell bonds, $\Lambda_{ij} = \Lambda_0$, except for the bonds along the interface, where it equals to Λ_I (figure 4.1A). We introduce λ as the relative bond tension along the interface compared to the other bonds

$$\lambda = \frac{\Lambda_I}{\Lambda_0} . \quad (4.1)$$

Furthermore, we consider another situation where cells within a number of cell rows, n , close to the interface divide with the probability p_I , while all the other cells divide with the same probability p_0 (figure 4.1B). The parameter β is introduced as the relative division rate of cells in the vicinity of the interface

$$\beta = \frac{p_I}{p_0} . \quad (4.2)$$

In this framework the overall properties of cells are determined by bulk bond tension $\bar{\Lambda}_0$, contractility of cells $\bar{\Gamma}$, external shear stress $\bar{\sigma}$, bias in cell division orientation δ , and bias in cell division probability ϵ .

4.2 Physical mechanisms shaping interfaces during growth

In this section we propose some general mechanisms to shape interfaces during growth phase. Starting with a reference case, we analyze how tissue growth influences the interfaces. We then introduce five different cases based on the physical mechanisms which may play a role in shaping interfaces. They take into account the local properties

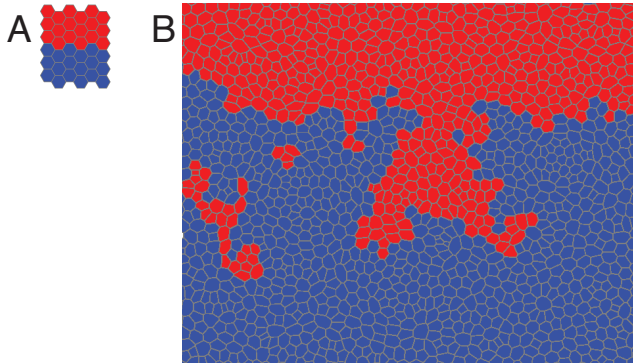


Figure 4.2: Growth of a cellular network including two lineage compartments (red and blue) of identical cells. (A) The initial configuration, two compartments are introduced in a small hexagonal network. (B) An example of the network configuration at generation $G = 6$ when thousands of cell divisions have occurred.

of cells near the interfaces and the overall cell characteristics. We will discuss in the next sections how each mechanism modifies the stress distribution in cellular networks and affects the morphology of interfaces.

Compartments of identical cells. As the reference case, we consider that all the cells in two compartments are identical. There is no external stress applying to the network and cell division is unbiased. We start from a hexagonal network, where half of the cells are marked as A compartment (red) and the other half are marked as B cells (blue) (figure 4.2A). The interface between two compartments is initially sharp and straight. During the growth phase, the interface becomes rough and some islands of one type of cells are observed surrounded by the cells of the other type (figure 4.2B). This roughening process originates from cell rearrangements and the randomness in cell divisions.

Increased cell bond tension along interfaces. In case I , we consider the situations where the bond tension is increased along the interface by a factor λ compared to the other bonds. Here $\lambda = 1$ implies that cell bond tension along the interface is the same as the other cell bonds. When the relative bond tension is increased at the interface $\lambda > 1$, cells of different compartments tend to shrink their shared interface. It suggests that this mechanism can play a role in shaping interfaces. This mechanism is considered as a basic mechanism to keep compartment boundaries straight [12]. There are some evidences for the increased bond tension at the compartment boundaries in biological tissues [4, 23–25, 102].

Reduced cell proliferation near interfaces. Case II describes the situations where cells within a number of rows, n , on both sides of the interface divide with the relative division rate β compared to the other cells. Here $\beta = 1$ describes the homogenous cell division all over the cellular network. With the help of this mechanism the strength of noise is reduced in the vicinity of the interface when $\beta < 1$. Experimental observations show that the cell proliferation is reduced near the DV boundary in the wing imaginal

disc [55] and at rhombomere boundaries in the chick embryo hindbrain [103]. This raises the question whether or not this mechanism has any influence on the shape of interfaces.

External shear. In case *III*, we analyze how global anisotropies of cells may influence the shape of interfaces. We consider that external shear stresses are applied to the tissue to produce global elongation of cells along the interface. Here $\bar{\Sigma}$ denotes the relative strength of external shear, while $\bar{\sigma} = 0$ corresponds to no external shear stress. This mechanism is motivated by the evidences of overall cell elongation near the DV boundary in the wing imaginal disc [102].

Oriented cell division. In case *IV*, the axis of cell division is biased by the elongation of the dividing cell. There are some evidences of such a bias in different tissues [75, 76], and we wonder whether this mechanism has any influence on interface dynamics. The strength of this effect is described by the coefficient δ , where $\delta = 0$ corresponds to an unbiased division axis. Interestingly, for $\delta > 0$ the axis of cell division will be randomly distributed where there is no correlation between elongation of cells. However, we expect that near an interface the local patterns of cell elongation appear depending on the interface curvature.

Pressure dependent proliferation rate. In case *V*, we consider that the probability of dividing each cell depends on its pressure (equation 3.2). Here ϵ describes the strength of this effect and for an unbiased division probability $\epsilon = 0$. The total pressure of each cell is determined by the isotropic part of the stress tensor (equation 3.23). It consists of cell area pressure and another term originating from the tension along cell bonds. Here we choose that the probability of cell division is influenced by cell area pressure. We also study other choices and the final conclusion is independent of this choice. The motivation for this mechanism is that interfaces can become straight due to the local changes in cell division probability, driven by special patterns of cell pressure near a curved interface suggested by Laplace's law.

4.3 Stress anisotropy and effective interfacial tension associated with interfaces

Here we analyze how cell stresses are modified in the vicinity of an interface during growth. In sections 3.4.1 and 3.4.2 we quantified stresses in two dimensional networks and averaged it for individual cells. Now we study how different mechanisms influence stress profile near the interfaces. We use the profile of anisotropic stress to quantify effective interfacial tension associated with different mechanisms.

4.3.1 Stress anisotropy associated with interfaces

In this section we analyze the stress profile for different cases introduced in the previous section. We investigate how the average stresses change moving from the interface to

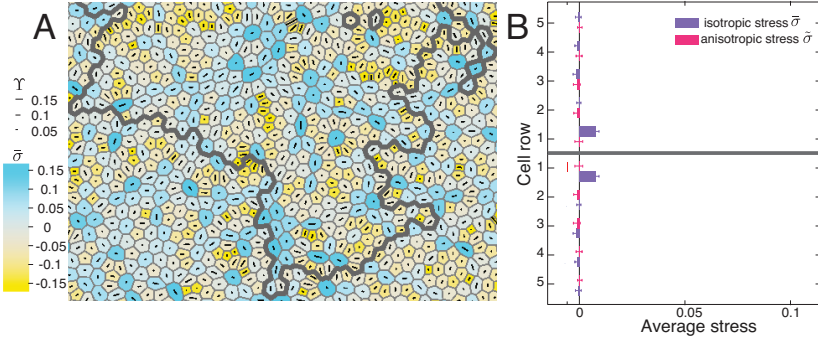


Figure 4.3: Stress profile near the interface (shown in dark gray) between compartments of identical cells in the reference case. (A) An example of average stress displayed for individual cells at generation $G = 8$. Isotropic stress $\bar{\sigma}$ is shown by a continuum color code. Anisotropic stress is represented by bars which describe the direction and strength of anisotropic stress, Υ . (B) The isotropic stress $\bar{\sigma}$ and the anisotropic stress $\tilde{\sigma}$, are averaged for different cell rows near the interface. Stress values are normalized by KA_0 . Mean and SEM are shown ($n=20$ realizations).

the compartments. To avoid fluctuations we average stress components for different cell rows near the interface, since everything is symmetric along the interface. The first cell rows of each compartment R_1 includes all the cells involving bonds at the interface. The next cell rows are defined in a similar way: $(n + 1)$ 'th row, R_{n+1} , is composed of all the cells which are not within the first n rows and share a bond with cells of n 'th row. The average stress of cell row n is then defined as

$$\langle \sigma_{ij}^n \rangle = \frac{1}{A^n} \int_{A^n} \sigma_{ij}(x, y) dA = \frac{\sum_{\alpha \in R_n} \sigma_{ij}(\alpha) A_\alpha}{A^n}, \quad (4.3)$$

where A^n is the area of cell row n , $A^n = \sum_{\alpha \in R_n} A_\alpha$. We average both the isotropic stress $\bar{\sigma} = (\sigma_{yy} + \sigma_{xx})/2$, as well as the anisotropic stress of cells $\tilde{\sigma} = (\sigma_{yy} - \sigma_{xx})/2$ to calculate $\langle \bar{\sigma}^n \rangle$ and $\langle \tilde{\sigma}^n \rangle$. We next discuss how the distribution of stresses near interfaces is influenced by tissue mechanics.

Compartments of identical cells. In the reference case where all the cells are identical the stress will be homogenous in average. Figure 4.3 shows the stress distribution in this case. We observe that the average anisotropic stress vanishes for different cell rows near the interface. However, the average isotropic stress has a non-zero average value in the first cell row. We discuss in appendix F that although the mechanical properties of all cells are identical, cells in the first rows have a larger area in average compared to the other cells. This explains that the average isotropic stress has a positive value in the first cell row.

Increased bond tension at the interface. In case I , increased cell bond tension at the interface leads to some anisotropies in the cellular network. Shape of cells is changed

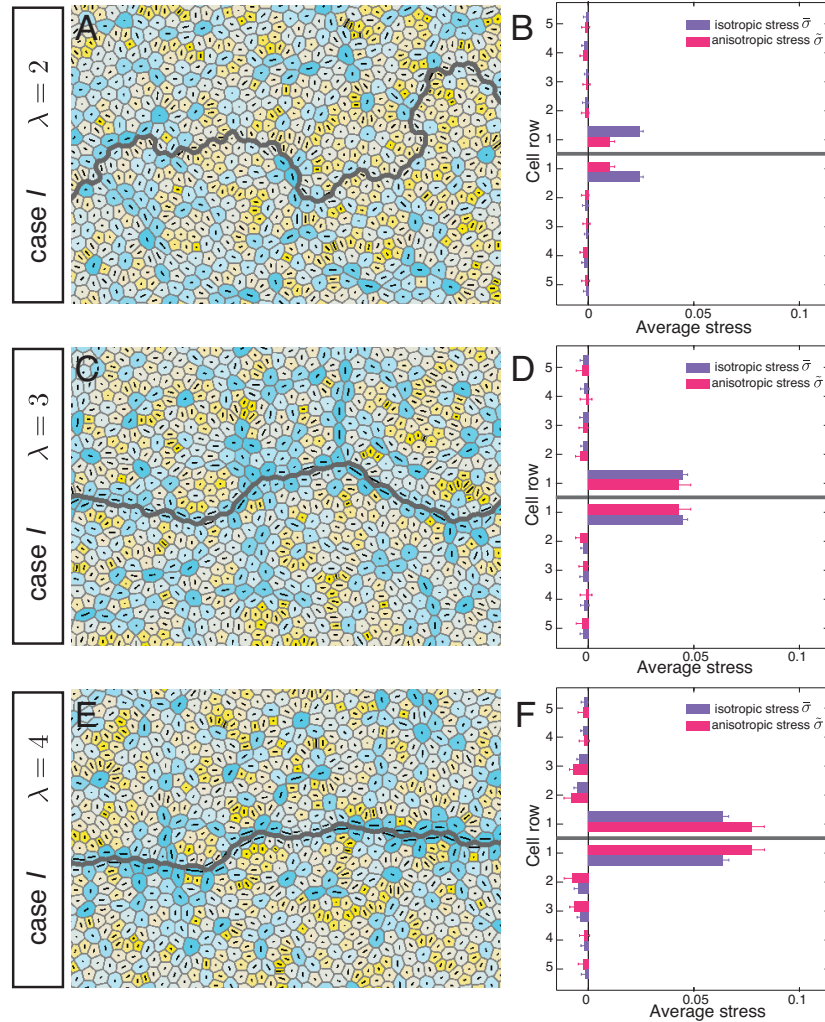


Figure 4.4: Stress profile near interfaces (shown in dark gray) in case I . Cell bond tension is increased along the interface with a factor (A, B) $\lambda = 2$, (C, D) $\lambda = 3$, and (E, F) $\lambda = 4$. (A, C, E) Average cell stress is displayed for individual cells at generation $G = 8$. The cell color shows average isotropic stress and the black bars represent the direction and magnitude of the anisotropic stress (with the same scales as figure 4.3). (B, D, F) The isotropic stress $\bar{\sigma}$ and the anisotropic stress $\tilde{\sigma}$, are averaged for different cell rows near the interface. Stress values are normalized by KA_0 . Mean and SEM are shown (n=20 realizations).

in response to the increased cell bond tension at the interface. For instance, cell bonds are in average shorter along the interface than cell bonds within the compartments, and cells are a bit elongated perpendicular to the interface. Importantly, the stress profile is no longer uniform. Figure 4.4 shows the stress profile in cellular networks with different values of relative bond tension at the interface, λ . The average isotropic stress of cells is increased for the cells sharing bonds at the interfaces. Apart from that, the shear stress does not vanish near the interfaces. The nematics representing cell shear stress become parallel to the interface for the cells within the first rows (figure 4.4A, C, and E). Figure 4.4B, D, and F shows the average isotropic and shear stress $\langle \tilde{\sigma}^n \rangle$ for different cell rows. The anisotropic stress in the vicinity of the interfaces grows in magnitude with increasing the relative interface bond tension λ . The average stresses of the cellular networks vanish when there is no external stress applying on the network. Therefore, the average stresses of the cells inside compartments change to satisfy this constraint. The stress anisotropy will be used later to quantify interfacial tension.

Reduced cell proliferation near the interface. Here we discuss how stress profile modifies if cell proliferation is reduced locally in the vicinity of the interface (case *II*). We analyze the stress profile in the cellular network for different choices of the relative division rate β in 2 cell rows at both sides of the interface (figure 4.5). Cells become elongated along the interface in the zone of reduced proliferation. Similar to case *I*, we observe patterns of anisotropic stress in the vicinity of interfaces. In this case, the shear stress is originated from the elongation of cells near the interfaces. However, in case *I* cells within the first rows are elongated in perpendicular direction to the interface and increased bond tension generates anisotropic stress. Besides, isotropic stress is not homogenous, and grows in the region of reduced proliferation. Figure 4.5 shows the average values of isotropic and anisotropic stresses in different cell rows. Reducing the relative proliferation rate β , the anisotropies become more pronounced. We analyze that the interfacial anisotropic stress increases when this mechanism is combined with increased cell bond tension at the interface (figure 4.5E, F).

External shear stress. Overall cell elongation can be obtained by applying external shear stresses. The external shear stress will change the shape of cells and their average stress throughout the cellular network. Figure 4.6 shows some examples of stress distribution in such cellular networks. Average anisotropic stress of the cellular network is set by the value of external shear, while the total average of cell pressure vanishes. The stress profile is quite homogeneous, however anisotropic, as far as all the cells are identical. Whereas, by increasing relative bond tension along the interface stress profile changes locally near the interface. This mechanism, in combination with increased bond tension at the interface, has a considerable effect on the distribution of anisotropic stress near the interface (compare figure 4.6C-D and figure 4.4A-B).

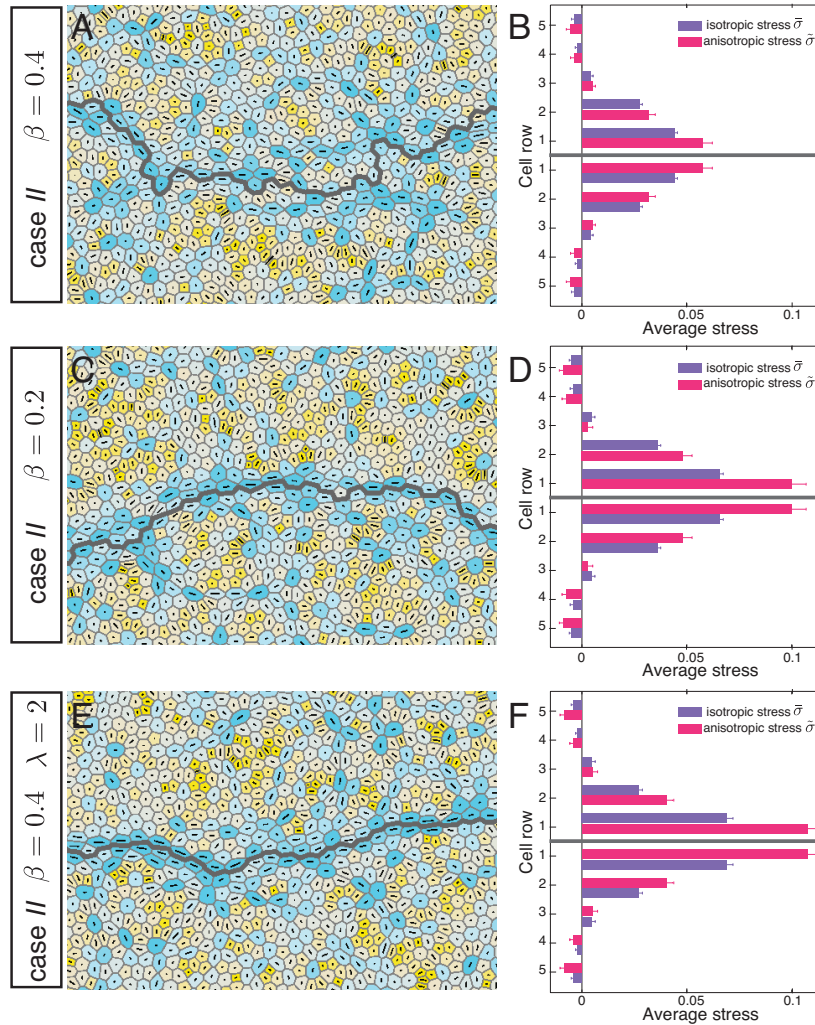


Figure 4.5: Stress profile near the interfaces (shown in dark gray) in case *II* when the rate of cell division is reduced by a factor β in two rows of cells on both sides of the interface. (A, B) $\beta = 0.4$, (C, D) $\beta = 0.2$, (E, F) $\beta = 0.4$ and $\lambda = 2$. (A, C, E) Average cell stress is displayed for individual cells at generation $G = 8$. The cell color shows average isotropic stress and the black bars represent the direction and magnitude of the anisotropic stress (with the same scales as figure 4.3). (B, D, F) The isotropic stress $\bar{\sigma}$ and the anisotropic stress $\tilde{\sigma}$, are averaged for different cell rows near the interface. Stress values are normalized by KA_0 . Mean and SEM are shown (n=20 realizations).

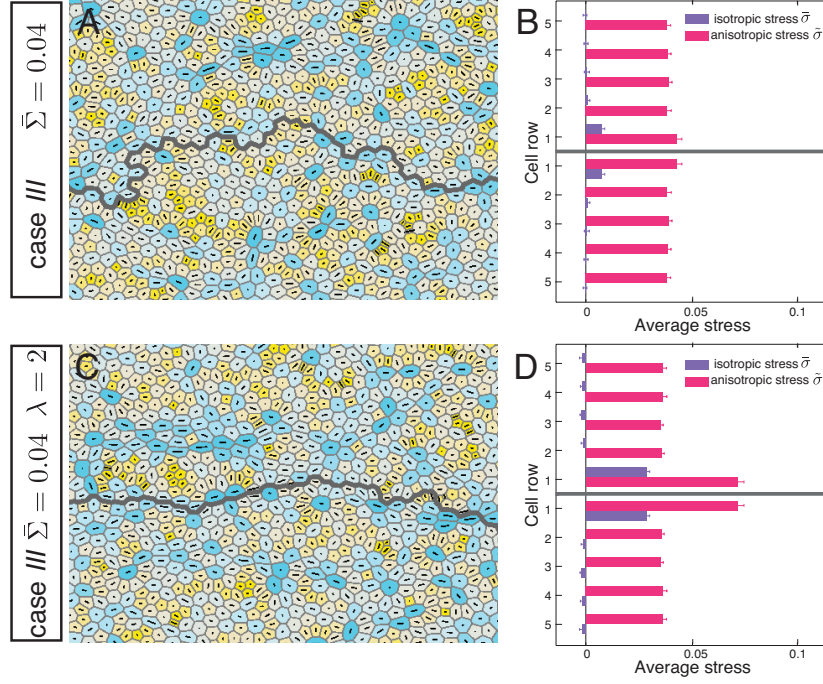


Figure 4.6: Stress profile in case *III* when anisotropic stress $\bar{\Sigma} = 0.04$ is applied to stretch the network parallel to the interface (shown in dark grey). (A, B) $\lambda = 1$, and (C, D) $\lambda = 2$. (A, C) Average cell stress is displayed for individual cells at generation $G = 8$. The cell color shows average isotropic stress and the black bars represent the direction and magnitude of the anisotropic stress (with the same scales as figure 4.3). (B, D) The isotropic stress $\bar{\sigma}$ and the anisotropic stress $\tilde{\sigma}$, are averaged for different cell rows near the interface. Stress values are normalized by KA_0 . Mean and SEM are shown (n=20 realizations).

4.3.2 Effective interfacial tension

In the previous section we studied the stress profile in the vicinity of an interface between two cellular compartments. Especially, we analyzed anisotropic stress for different cases. We observed that increasing cell bond tension along the interface as well as reducing cell proliferation near the interface locally change anisotropic stress. In this section, we use the profile of anisotropic stress to calculate interfacial tension and analyze how much different mechanical properties of the cellular network contribute to interfacial tension.

We quantified the effective interfacial tension integrating anisotropic stress in a two-component fluid (equation 2.9). With the same approach, we can calculate the effective interfacial tension in the cellular networks by integrating the anisotropic stress over area

$$\gamma = \frac{2}{L_y} \int_A (\tilde{\sigma} - \tilde{\sigma}_0) dA, \quad (4.4)$$

where A is the total area of the cellular network. $\tilde{\sigma}_0$ is the average anisotropic stress in

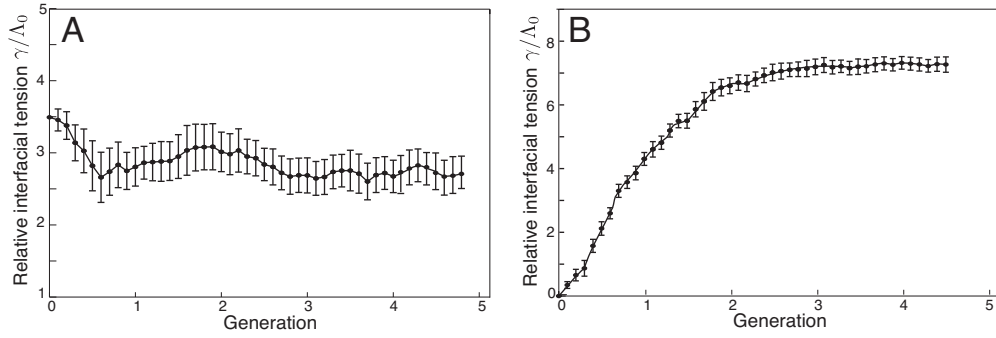


Figure 4.7: Effective interfacial tension as a function of generation. (A) Cell bond tension is increased along the interface by a factor $\lambda = 3$. (B) Rate of cell division is reduced by a factor $\beta = 0.4$ in $n = 2$ rows of cells on both sides of the interface. Mean and SEM are shown ($n=10$ realizations).

the bulk and far from the interface, where $\langle \tilde{\sigma}^n \rangle$ reaches a constant value. We can replace this integral by a summation over all cells

$$\gamma = \frac{2}{L_y} \sum_{\alpha} (\tilde{\sigma}(\alpha) - \tilde{\sigma}_0) A_{\alpha} . \quad (4.5)$$

Time dependency of interfacial tension. We first study how interfacial tension evolves during tissue growth. Figure 4.7 shows interfacial tension as a function of generation for case *I* and case *II*. In case *I*, when cell bond tension is increased along the interface, effective interfacial tension decreases slightly from the initial hexagonal configuration and remains approximately constant during growth. In case *II*, where cell division probability is reduced near the interface, effective interfacial tension vanishes initially. However, while tissue grows cells with less proliferation elongate and the effective interfacial tension increases rapidly and plateaus later. We conclude that beyond the initial configuration, the effective interfacial tension does not depend on the generation or the size of the network.

Interfacial tension and tissue mechanics. We calculate the effective interfacial tension when it plateaus and analyze how mechanical properties of cells influence the effective interfacial tension. Figure 4.8 compares the effective interfacial tension between different cases for several choices of increased cell bond tension along the interface. In the reference case with identical cells, the anisotropic stress is uniformly distributed all over the network and the effective interfacial tension vanishes. Increasing cell bond tension along the interface as well as reducing proliferation in the vicinity of the interface increase interfacial tension. More interfacial tension is gained by combining these two mechanisms. Applying an external shear stress generates no effective interfacial tension as far as all the cells are identical. However, when cell bond tension is increased along the interface, the interfacial tension is increased compared to case *I*. Effective interfacial

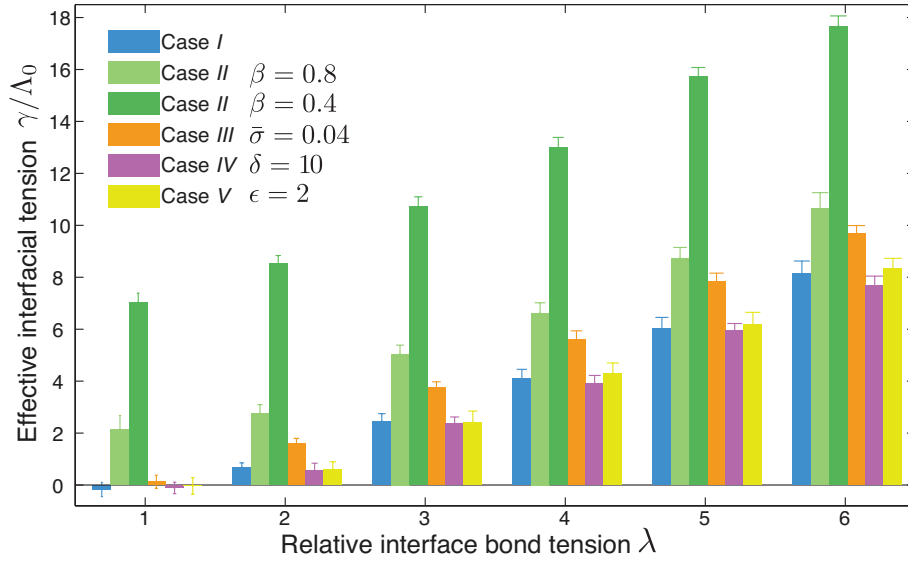


Figure 4.8: Effective interfacial tension and cell mechanics. Interfacial tension as a function of relative cell bond tension along the interface λ . Each color represents one case describing different mechanisms, increased bond tension along the interface (case *I*), reduced proliferation near the interface (case *II*), external shear (case *III*), orientated cell division (case *IV*), and pressure-dependent division rate (case *V*).

tension remains unchanged in comparison to case *I* when cell division probability depends on cell area pressure or cell division orientation is biased by cell elongation likewise.

4.4 Roughness of interfaces during tissue growth

In this section we study the morphology of interfaces and discuss how tissue mechanics influences the interface shape. Morphology of interfaces modifies during growth of cellular networks. Figure 4.9 shows an example of interface shape at different generations. The interface is initially chosen to be straight ($G = 0$). In this example, one can distinguish the increase of the interface length driven by tissue growth, from the interface roughening, which is read as the increase in the width of excursions in the perpendicular direction. In section 4.1, we explained that the roughening process happens because of the randomness of cell divisions and cell rearrangements. On the other hand, interface morphology is definitely affected by tissue mechanics. Here we analyze the morphology of interfaces during tissue growth for different cases introduced in section 4.2.

The shape of interfaces is described by a sequence of the position of the vertices along the interface. We use two different methods to quantify the shape of interfaces by measuring the roughness or analyzing the Fourier transform. The interface roughness is determined by the average variance of excursions of the interface away from a straight line as a function of the length traveled along this line. This roughness measure is

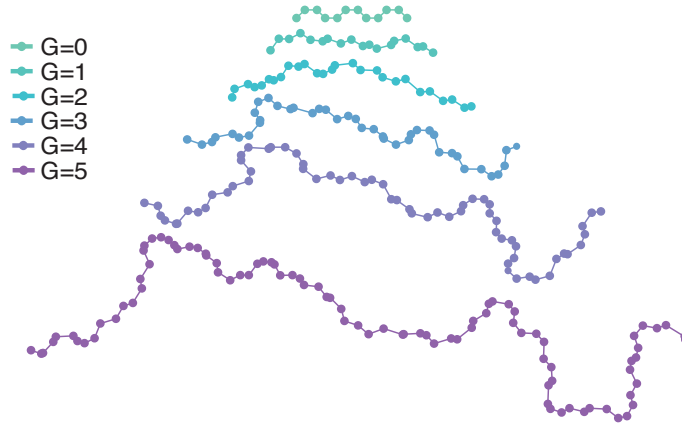


Figure 4.9: The shape of an interface between two cellular compartments during six generations of simulated tissue growth. The cell vertices along the interface are shown by circles and different colors depict different generations.

therefore given as a function of time and length $w = w(L, t)$ (equation 1.2 and E.1). Furthermore, the Fourier coefficients of the interface shape $C(q)$ represent the amplitude of periodic functions with different wavelengths. In appendix E we explain in detail how to implement these definitions to analyze the shape of interfaces in cellular networks. Here we use these methods to quantify the shape of interfaces and compare different cases.

Compartments of identical cells. We first quantify the interface shape in the reference case, where all the cells are identical. The interfaces are initially chosen to be globally straight, however it is slightly rough in the cellular scale due to the hexagonal packing of the cellular network. A straight interface starts to become rough as tissue grows, governed by the randomness of cell divisions. Figure 4.10B-C shows the interface roughness averaged over different realizations. The roughness of interfaces increases as a function of time (generation number) and with increasing distance along the interface. Furthermore, we look at the Fourier coefficients of these interfaces which decrease with the wave number q (figure 4.10D). For any wave number the Fourier coefficient decreases slightly as tissue grows. Whereas, due to the tissue growth and increase of the interface length L_y , the plots include more wave numbers.

Increased bond tension at the interface. In case *I*, when cell bond tension is increased along the interface by a factor λ , interfaces are more straight compared to the reference case (figure 4.11A, E, and I). Figure 4.11 shows the interface roughness for different choices of the interface bond tension λ . Compared to the reference case, interface roughness is significantly reduced both over time and with increasing distance. Increasing cell bond tension along the interface correlates with the reduction of interface roughness for different choices of λ . Similar to the reference case, the Fourier coefficients

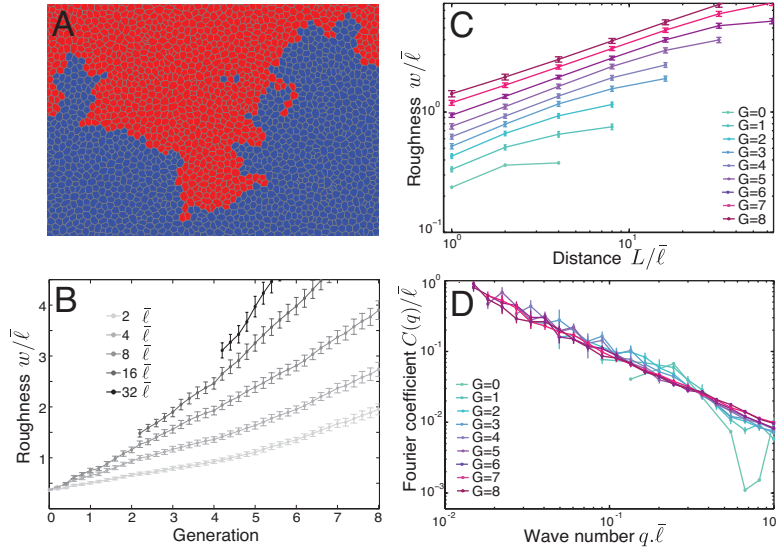


Figure 4.10: Time-evolution of the interface morphology between compartments of identical cells in the reference case. (A) An example of the final configuration of the network of cell bonds of the two adjacent cell populations (red and blue) at generation $G=8$. (B) The roughness w of the interface as a function of generation G for the indicated distances L along the interface. (C) The roughness w of the interface as a function of distance L for the generations G indicated. Distance and roughness values are normalized by mean bond length $\bar{\ell}$. (D) Fourier coefficient $C(q)$, normalized by $\bar{\ell}$, as a function of the wave number q , normalized by $1/\bar{\ell}$, for the generations G indicated. Mean and SEM are shown ($n=20$ realizations).

of interfaces decrease with increasing λ .

Reduced cell proliferation near the interface. In case *II*, interfaces are more straight compared to the reference case. Figure 4.12 shows two examples when cell proliferation is reduced by a factor β within two cell rows on both sides of the interface. The interface is maintained with locally decreasing proliferation rate, even if there is no increased cell bond tension at the interface. This mechanism has similar effects as increasing interface bond tension in decreasing interface roughness. Decreasing the relative cell proliferation rate near the interface leads to more straight interfaces. In figure 4.13 we compare roughness of interfaces for different choices of β changing between 1 and 0. Furthermore, interface roughness decreases even further combining this mechanism with increased cell bond tension at the interface.

Anisotropic shear stress. Here we quantify the effects of external shear forces, described by $\bar{\Sigma}$, on the morphology of interfaces (case *III*). Two examples, where $\bar{\Sigma} = 0.03$ and $\bar{\Sigma} = 0.04$, are shown in figure 4.14. The shear stress results in both elongation

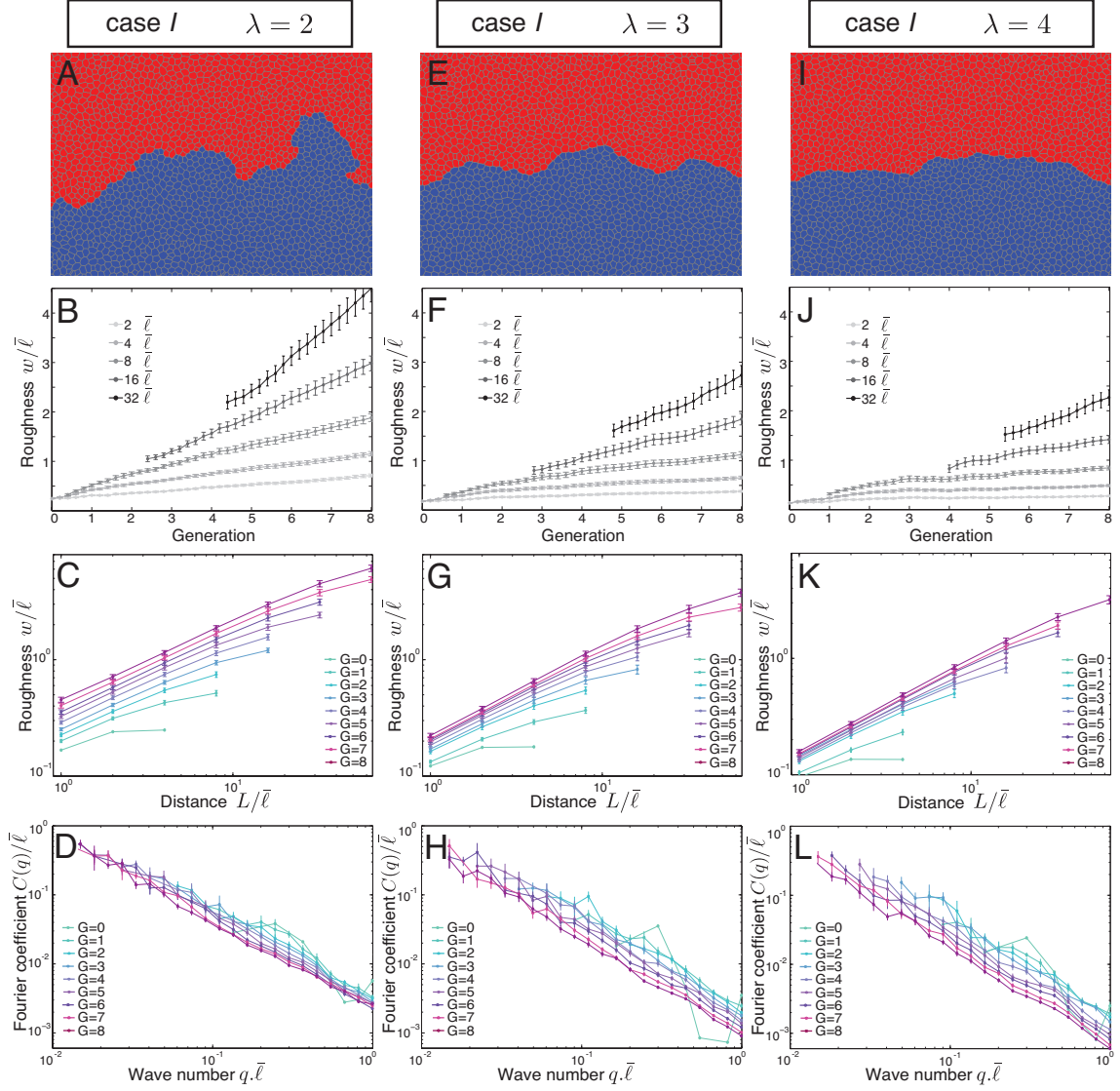


Figure 4.11: Time-evolution of the interface morphology in case *I*. Cell bond tension is increased along the interface with a factor (A-D) $\lambda = 2$, (E-H) $\lambda = 3$, and (I-L) $\lambda = 4$. The top row (A, E, I) represents examples of the final configuration of the network of cell bonds of the two adjacent cell populations (red and blue) at generation $G = 8$. The second row (B, F, J) depicts the roughness w of the interface as a function of generation G for the indicated distances L along the interface. The third row (C, G, K) shows the roughness w of the interface as a function of distance L for the generations G indicated. In the second and third rows, distance and roughness values are normalized by mean bond length $\bar{\ell}$. The fourth row (D, H, L) shows the Fourier coefficient $C(q)$, normalized by $\bar{\ell}$, as a function of the wave number q , normalized by $1/\bar{\ell}$, for the generations G indicated. Mean and SEM are shown ($n=20$ realizations).

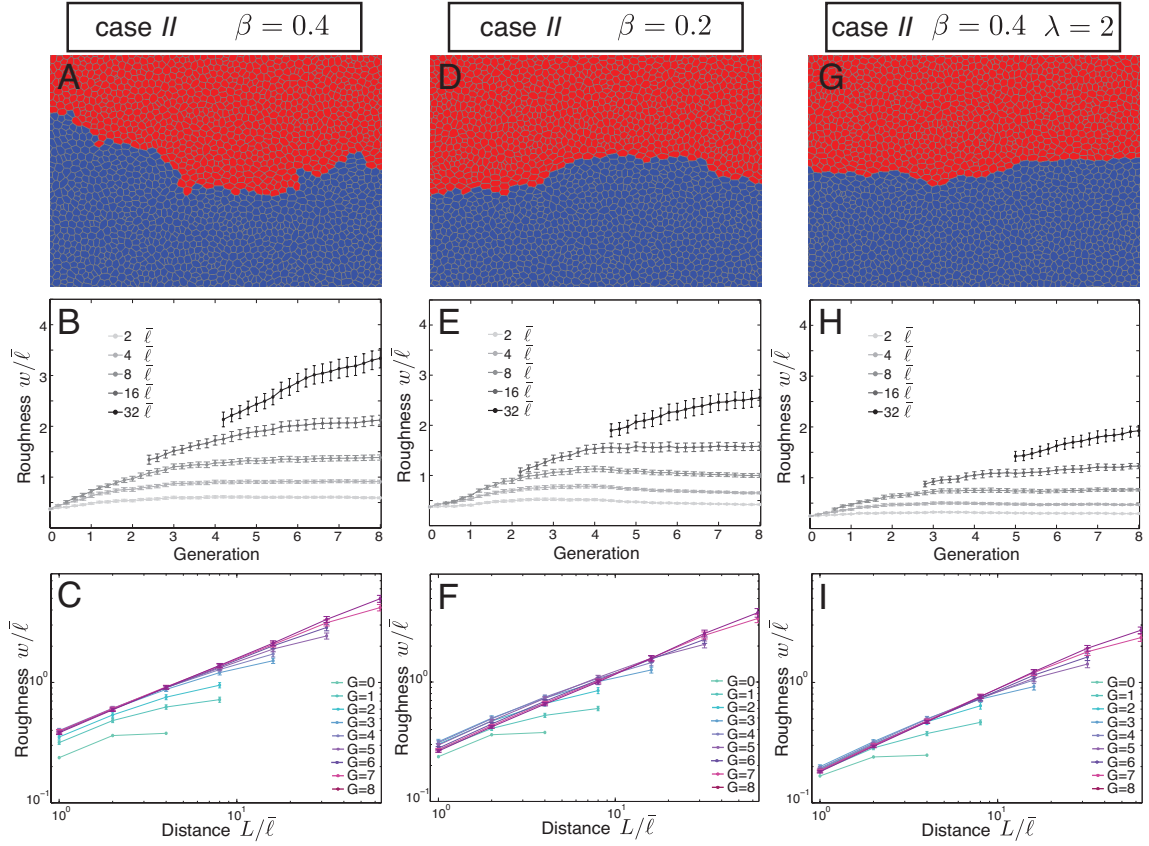


Figure 4.12: Time-evolution of the interface morphology in case *II*, when the rate of cell division is reduced by a factor β in two rows of cells on both sides of the interface. (A-C) $\beta = 0.4$, (D-F) $\beta = 0.2$, $\beta = 0.4$ and (G-I) $\lambda = 2$. The top row (A, D, G) represents examples of the final configuration of the network of cell bonds of the two adjacent cell populations (red and blue) at generation $G = 8$. The second row (B, E, H) depicts the roughness w of the interface as a function of generation G for the indicated distances L along the interface. The third row (C, F, I) shows the roughness w of the interface as a function of the distance L for the generations G indicated. In the second and third rows, distance and roughness values are normalized by mean bond length $\bar{\ell}$. Mean and SEM are shown ($n=20$ realizations).

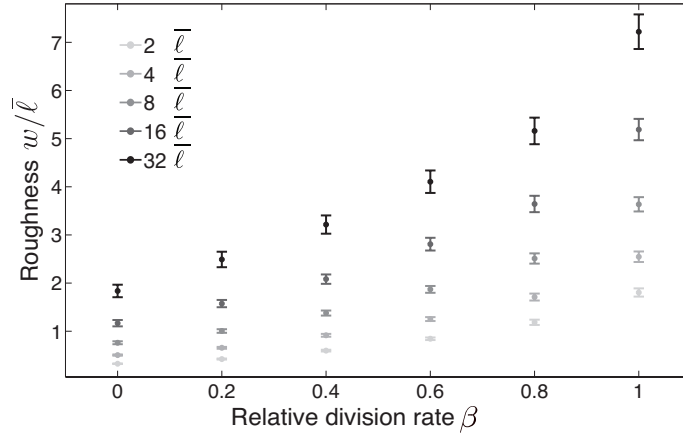


Figure 4.13: Interface roughness as a function of relative division rate of cells within two cell rows near the interface β , while $\lambda = 1$, for the indicated distances L along the interface at generation $G = 8$. Distance and roughness values are normalized by mean bond length \bar{l} . Mean and SEM are shown (n=20 realizations).

of individual cells and overall elongation of the cellular network. In this case cell mixing is not prevented, some islands of one cell type exist within the other compartment. However, the interface roughness is reduced significantly compared to the reference case (figure 4.14). Figure 4.15 describes how interface roughness decreases with increasing the strength of external shear stress. Interfaces are maintained if this mechanism acts with increased cell bond tension at the interface. In this case interface roughness is mainly decreased compared to case *I* (compare figure 4.14I-L and figure 4.11A-D).

Oriented cell division. We analyze the shape of interfaces during tissue development when orientation of cell division is biased by cell elongation (case *IV*). In this case the roughness of the interface increases with generation number for different lengths similar to the reference case (compare figure 4.10B and figure 4.16B). Figure 4.16 represents an example where $\delta = 5$, however, this result is independent of the value of δ . It can be explained that in a cellular network of identical cells there is no correlation between cell elongation near the interface (figure 4.17A,B). Therefore this mechanism has no effect on the interface morphology. Interestingly when both cell bond tension along the interface is increased and the orientation of cell division is biased by cell elongation, the interface roughness is significantly reduced both over time and increasing distance as compared to case *I* (figure 4.16; figure 4.11). This happens because increased cell bond tension results in local patterns of cell elongation that depend on interface curvature (figure 4.17C,D). The resulting bias of the cell division orientation is such that local interface roughness is reduced.

Pressure dependent proliferation rate. Now we analyze the morphology of interfaces in case *V*, where cell pressure influences the probability of cell division. Fig-

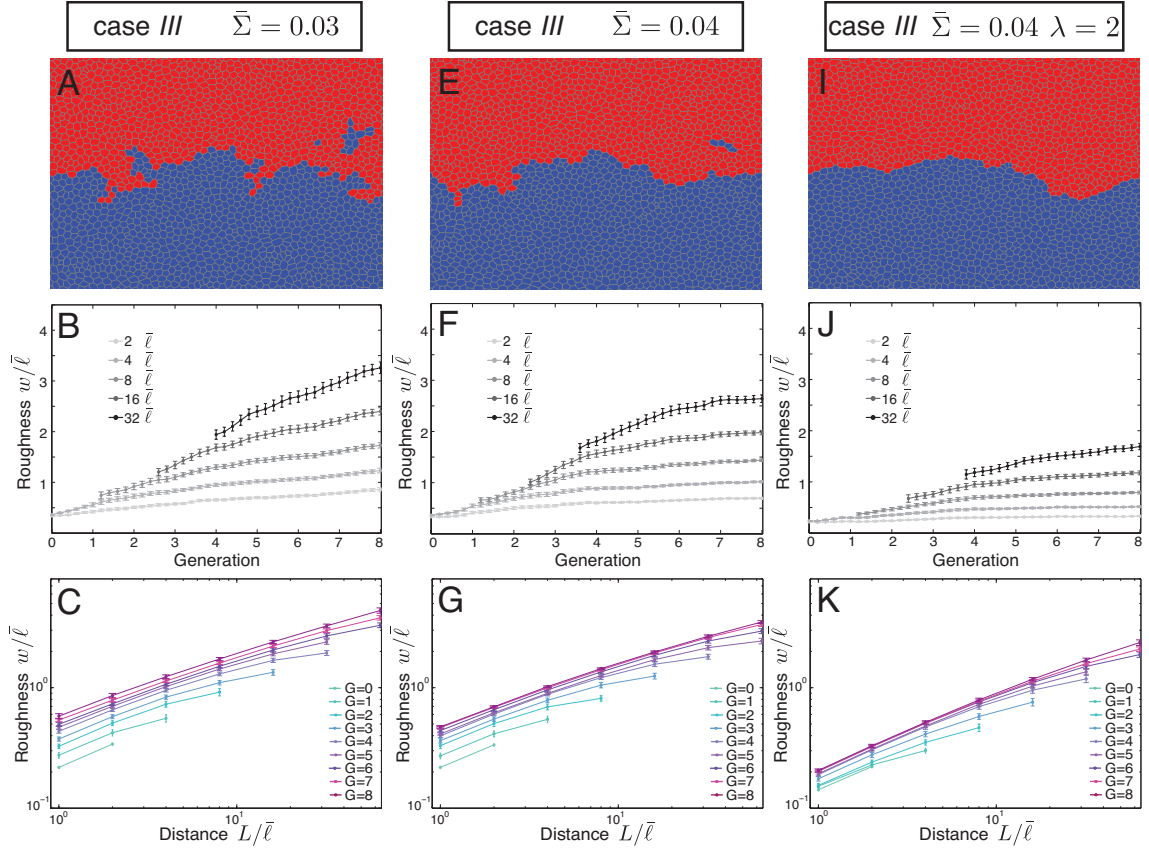


Figure 4.14: Time-evolution of the interface morphology in case *III* when anisotropic stress of the relative strength σ is applied to stretch the network parallel to the interface. (A-C) $\bar{\Sigma} = 0.03$, (D-F) $\bar{\Sigma} = 0.04$, (G-I) $\bar{\Sigma} = 0.04$ and $\lambda = 2$. The top row (A, D, G) represents examples of the final configuration of the network of cell bonds of the two adjacent cell populations (red and blue) at generation $G = 8$. The second row (B, E, H) depicts the roughness w of the interface as a function of generation G for the indicated distances L along the interface. The third row (C, F, I) shows the roughness w of the interface as a function of the distance L for the generations G indicated. In the second and third rows, distance and roughness values are normalized by mean bond length $\bar{\ell}$. Mean and SEM are shown ($n=20$ realizations).

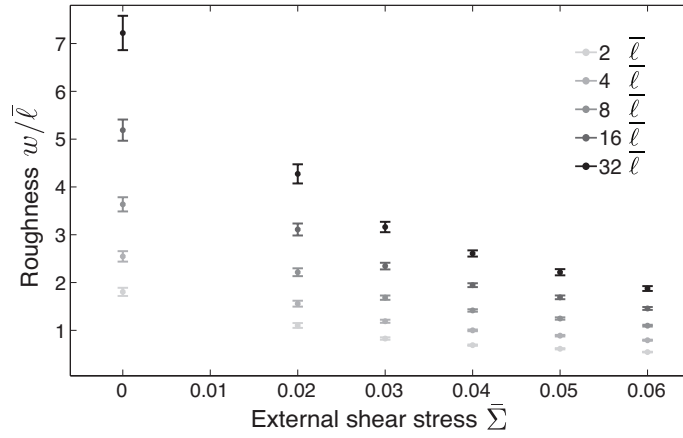


Figure 4.15: Interface roughness as a function of anisotropic stress $\bar{\Sigma}$, while $\lambda = 1$, for the indicated distances L along the interface at generation $G = 8$. Distance and roughness values are normalized by mean bond length $\bar{\ell}$. Mean and SEM are shown (n=20 realizations).

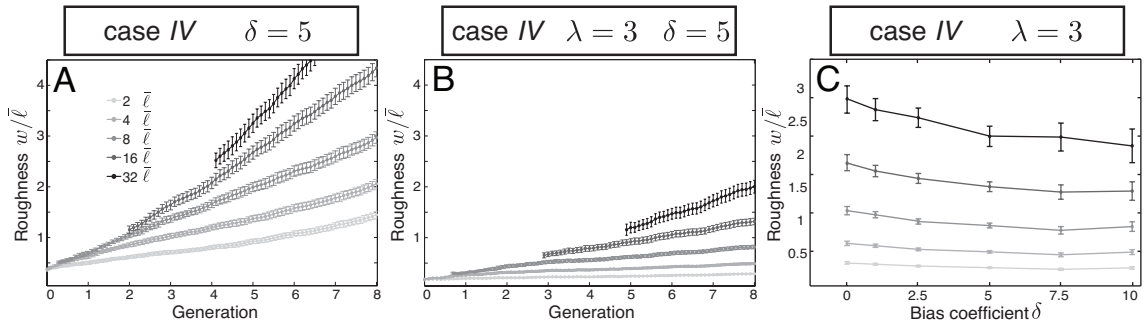


Figure 4.16: Interface morphology in case IV when orientation of cell division is biased by cell elongation with a coefficient δ . (A, B) Interface roughness w of the interface as a function of generation G for the indicated distances L along the interface when $\delta = 5$. Relative cell bond tension along the interface is (A) $\lambda = 1$, (B) $\lambda = 3$. (C) The interface roughness w as a function of the strength of bias δ for the indicated distances L along the interface at generation $G = 7.5$. Cell bond tension is increased along the boundary by a factor $\lambda = 3$. Distance and roughness values are normalized by mean bond length $\bar{\ell}$. Mean and SEM are shown (n=10 realizations).

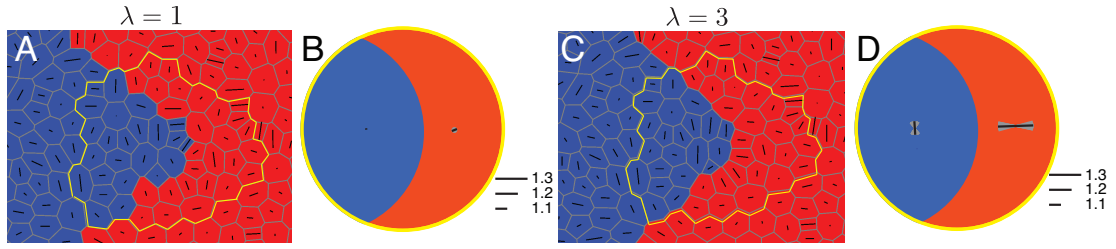


Figure 4.17: Local pattern of cell elongation around a curved boundary. The boundary is introduced as a sine function in a cell network after growth. The elongation of cells in two compartments (blue and red) near the boundary is indicated by black bars. (A, C) Examples of individual cell elongation around such a boundary. (B, D) Cell elongation averaged over 10 realizations in a few cell rows on both sides of the boundaries, indicated by a yellow line. Gray regions show the distribution of angles of average cell elongation in different realizations. (A, B) Cell bond tension is not increased at the interface ($\lambda = 1$) and cell elongation is isotropically distributed. (C, D) Interface cell bond tension is increased ($\lambda = 3$) and cell elongation is biased by the boundary curvature.

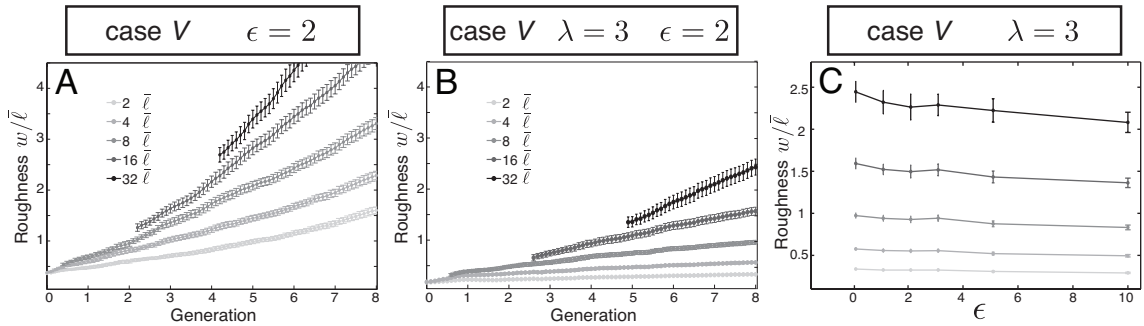


Figure 4.18: Interface morphology in case V when the probability of cell division depends on cell pressure by ϵ . (A, B) Interface roughness w as a function of generation G for the indicated distances L along the interface. The probability of cell division depends on cell pressure by $\epsilon = 2$. Relative cell bond tension along the interface is (A) $\lambda = 1$, (B) $\lambda = 3$. (C) The interface roughness w as a function of the coefficient ϵ for the indicated distances L along the interface at generation $G = 7.5$. Cell bond tension is increased along the boundary by a factor $\lambda = 3$. Distance and roughness values are normalized by mean bond length $\bar{\ell}$. Mean and SEM are shown ($n=10$ realizations).

ure 4.18A shows the average roughness of interfaces between two compartments of identical cells where the probability of cell division depends on cell area pressure by $\epsilon = 2$. In this case boundary roughness increases as in the reference case and cell mixing occurs (compare figure 4.18A and figure 4.10B). This result is independent of the value of the coefficient ϵ .

We next analyze whether cell proliferation depending on cell area pressure influences interface morphology if it acts together with increased cell bond tension along the interface. The motivation for this effect is that increased bond tension may give rise to increased pressure on the side of the interface towards which it is curved. The reduction of cell division probability on this side reduces the interface curvature and thus the interface becomes less rough. In appendix D we quantify the difference of inside and outside cell area pressure near a curved interface in a hexagonal network.

Figure 4.18B shows that this mechanism, even in combination with local increases in interface bond tension, has no considerable effect on boundary morphology (compare to figure 4.11F). Figure 4.18C shows how roughness changes with the strength of this effect ϵ . It should be mentioned that cells in the first rows have in average larger area pressure when interface bond tension is increased. Therefore, for large values of ϵ , all the cells within the first row divide with a significantly reduced probability and this mechanism acts as case *II* ($\epsilon = 10$ in figure 4.18C). For applicable values of ϵ the effects of this mechanism on interface morphology are negligible. This could originate from the fact that fluctuations in cell area are bigger than systematic differences in the vicinity of a curved interface. This result is independent of the choice of cell area pressure in equation 3.2. The shape of interfaces remains in average unchanged when the probability of cell division depends on the total pressure or the tension pressure.

Scaling properties of interfaces. We analyze the scaling properties of the interfaces between cellular compartments. In the introduction we discussed the scaling relations for self-affine interfaces (equations 1.4, 1.5, and 4.7). In many cases studied in this chapter, the roughness saturates at late generations (see appendix E for detailed discussion). We show that the saturation roughness scales with distance (figure 4.19A)

$$w(L) \propto L^a. \quad (4.6)$$

The roughness exponent a does not show a meaningful dependence on the tissue parameters and fluctuates between 0.65 and 0.75. Figure E.4 shows how roughness exponent varies for different mechanisms. Furthermore, analyzing the Fourier transform of interfaces indicates that the Fourier coefficients of interfaces scale with the wave number (equation 4.7)

$$C^2(q) \propto q^f. \quad (4.7)$$

Similar to the roughness exponent, the Fourier exponent f does not change significantly between different mechanisms and varies in the range of 2.2 – 2.7 (see figure E.5).

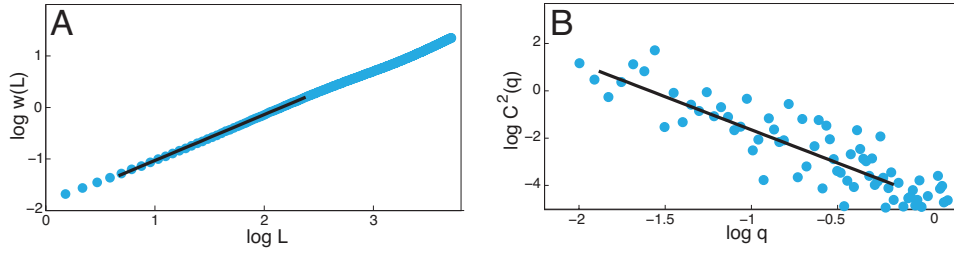


Figure 4.19: Examples of scaling properties of interfaces ($\lambda = 3$). (A) Roughness of the interface as a function of distance in a logarithmic scale (blue dots). A linear fit of the data is shown (black line). The slope of the line defines the roughness exponent a . (B) Fourier transform of interface shape as a function of the wave number in a logarithmic scale (blue dots). A linear fit of the data is shown (black line). The slope of the line defines the Fourier exponent f .

4.5 Summary

In this chapter we introduced the cellular compartments in the vertex model. We analyzed how compartment boundaries evolve during simulated tissue growth. We studied the stress distribution inside the cellular networks and calculated effective interfacial tension by integrating the anisotropic stress. Moreover, we quantified the morphology of interfaces by measuring its roughness and analyzing its Fourier transform. An initially straight interface becomes rough due to stochastic behavior of cell divisions. On the other hand the interface roughness increases with increasing distance along the interface.

With the help of this model we studied how different physical mechanisms affect the stress distribution and shape of interfaces in developing tissues. In a cellular network including two compartments of identical cells, the interface becomes very rough during tissue growth. In this reference case the stress is distributed randomly all over the cellular network and there is no effective interfacial tension. However, increased cell bond tension at the interface and reduced cell proliferation near the interface produce effective interfacial tension. In both cases we observe overall reduction of values of roughness compared to the reference case. In addition, overall cell elongation in the tissue parallel to the interface induced by external shear produces no considerable effective interfacial tension. However, it leads to a significant reduction of roughness. Furthermore, a bias in orientation of cell division by cell elongation, or the dependence of cell division probability on cell area pressure do not contribute in the interfacial tension. The preferential cell division orientation has no influence on boundary roughness. But the boundary roughness is further reduced when it is combined with local increases in cell bond tension. However, the pressure-dependent division rate mechanism has, even in combination with local increases in interface bond tension, no considerable effect on boundary morphology. We also analyzed the scaling behavior of interfaces for different mechanisms. We showed that the saturation value of roughness scales with the distance along the interface and the Fourier transform of interfaces scales with the wave number.

Chapter 5

Experimental study of the dorsoventral compartment boundary in the developing fly wing

The wing imaginal disc of the fruit fly *Drosophila* is an important model system to study compartmentalization (see section 1.3). There are two compartment boundaries in the wing imaginal disc, the anteroposterior (AP) boundary and the dorsoventral (DV) boundary. In this work we quantitatively analyze which mechanisms play a role in shaping the dorsoventral boundary in the developing fly wing. In this chapter we review our experimental results on the mechanics and morphology of dorsoventral compartment boundary. The experiments are subdivided into three categories. At first we analyze the images of the wing imaginal discs in the vicinity of the DV compartment boundary at different stages during wing development. In particular we quantify elongation of cells near the DV boundary and quantify the roughness of the boundary. In the second part we discuss the laser ablation experiments. We analyze the response of tissues to the ablation of cell bonds in order to estimate cell bond tension at different developmental stages. Moreover, we analyze the pattern of cell division near the DV boundary and study whether this mechanism has any influence on the boundary shape. The experimental results will be used in the next chapter in order to propose a scenario characterizing the time evolution of the DV boundary.

5.1 Morphology of wing imaginal discs near the dorsoventral boundary

We analyze the images of the adherens network of cells in order to quantify the morphology of the wing discs near the DV boundary at different developmental times (72h, 84h, 96h, 108h, and 120h AEL). Wing discs are stained for *E-cadherin*, a marker for adherens

junctions, and a membrane-associated GFP, *CD8-GFP*, expressed under control of the dorsal-specific *ap-GAL4* line [104] (figure 5.1A-E). We use automated image analysis to distinguish cell bonds and quantify tissue properties (see appendix G.1). For instance, we quantify the morphology of cells in the vicinity of this boundary and the roughness of the DV boundary at different developmental times.

5.1.1 Cell shape analysis

The shape of cells reflects their mechanical properties and the local stresses. In the network of adherens junctions, the shape of each cell is described by the cell bonds and cell vertices. We quantitatively analyze the shape of cells all over the wing imaginal disc. Cell shape in two dimensional tissues can be described by cell area and cell elongation (See appendix C). We quantify cell elongation with a symmetric traceless tensor (equation C.1). This tensor can be displayed by a bar at angle Ω and length ρ , which can be mapped to the ratio of long to short axis of the cell. Figure 5.1F-J shows shape of individual cells quantified in some examples of wing disc images at different developmental stages.

We average cell properties to compare morphology of cells at different stages and in different regions of the tissue. Interestingly, cells in the vicinity of the DV boundary are clearly elongated with an average ratio of long to short axis of 1.1-1.3 parallel to the DV boundary at all time points analyzed (figure 5.1N). We also observe that the average apical cross section area of cells at the level of adherens junctions decreases between 84h and 120h AEL and is similar for cells along the DV boundary and cells in the analyzed area of the tissue (figure 5.1K). Furthermore, the average cell bond length decreases between 84h and 120h AEL. We observe the same behavior for the average cell bond length at the DV boundary, which is always shorter than the tissue average bond length (figure 5.1L). Besides, the angles between cell bonds are typically larger along the DV boundary compared to the bond angles of the rest of the tissue (figure 5.1M). These two observations can be signatures of increased bond tension at the DV boundary.

5.1.2 Roughness of the DV boundary

We next quantify the roughness of the DV boundary at different developmental times. The shape of the boundary is shown by a sequence of the position of the vertices along the boundary and we calculate the roughness of the boundary as the deviation from a straight line as described in equation E.1.

The roughness of the DV boundary increases with increasing distances along the boundary. Surprisingly, the roughness starts with comparably high values at 72h and 84h AEL, but is reduced at 96h and remains almost constant after that, at 108h and 120h AEL (figure 5.2A-B). Note that in figure 5.2A,B the roughness is normalized to the average cell bond length of each time, which is not constant. However the choice of this normalization has no effect on our conclusions. We observe similar behavior when roughness is presented in micrometer and is not normalized.

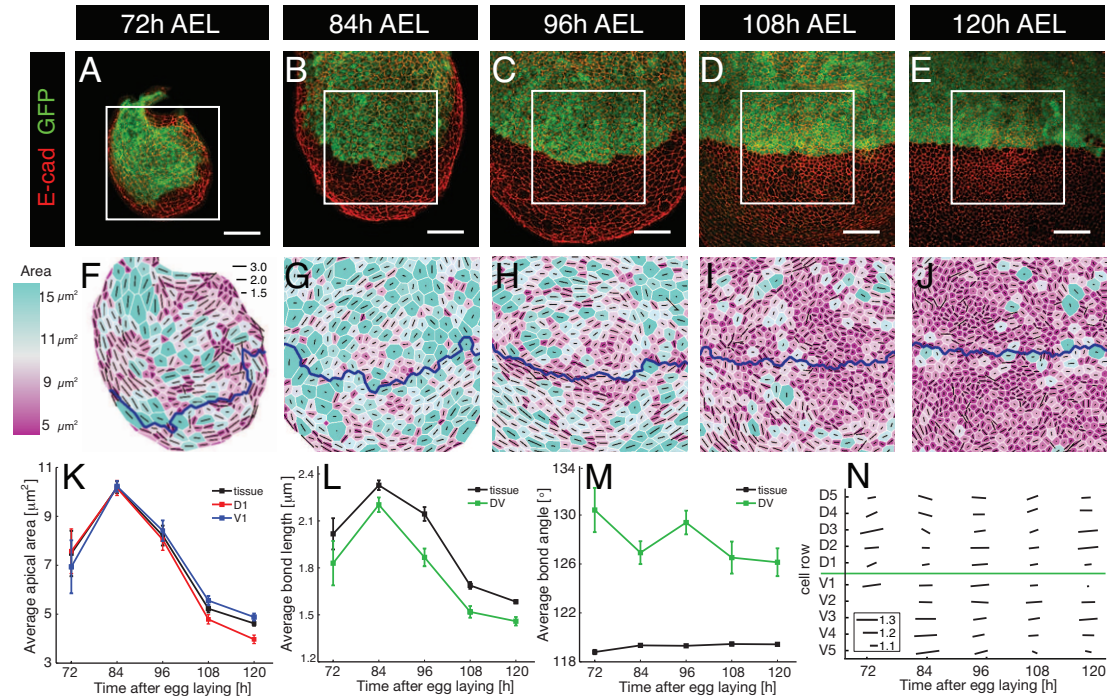


Figure 5.1: (A-E) Wing imaginal discs at (A) 72h, (B) 84h, (C) 96h, (D) 108h, and (E) 120h AEL stained for *E-cadherin* (*E-cad*, red). The dorsal compartments are visualized by expression of *CD8-GFP* (green). Scale bars represent $20\mu\text{m}$. (F-J) Analysis of the areas boxed in (A-E). Apical cross sectional area is color coded as indicated on the left. Bold blue lines demarcate the DV boundary. The lengths of the black bars represent the ratio of long to short axis of cells. (K) Average apical area for D1 cells, V1 cells, and the total wing imaginal disc region analyzed (tissue) for the indicated time points. Mean and SEM are shown. (L) Average cell bond length along the DV boundary, and within the total wing imaginal disc region analyzed (tissue) for the indicated time points. Mean and SEM are shown. (M) Average angle between cell bonds along the DV boundary, and within the total wing imaginal disc region analyzed (tissue) for the indicated time points. Mean and SEM are shown. (N) Average cell elongation of different cell rows near the DV boundary (D1..D5, V1...V5) of the analyzed region for the indicated time points. Green line demarcates the DV boundary. The length of the bars represents the ratio of long to short axis of a cell parallel to the DV boundary (see inset).

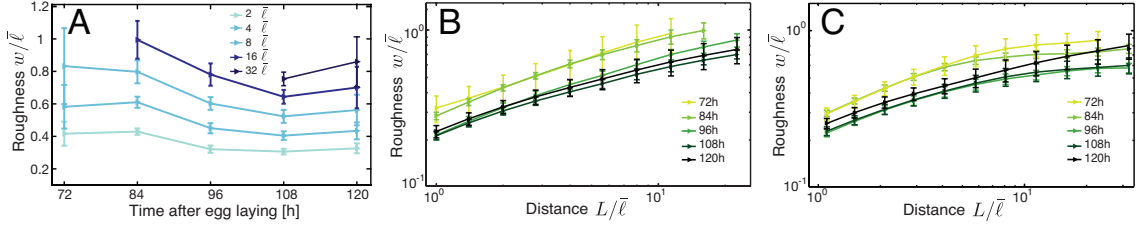


Figure 5.2: (A) Roughness w of the interface as a function of time after egg laying for the indicated distances L . (B) roughness w of the interface as a function of distance L for the indicated times after egg laying. (C) Circle roughness w of the interface as a function of distance L for the indicated times after egg laying. Distance and roughness values are normalized to the average cell bond length $\bar{\ell}$ for the indicated times after egg laying. Mean and SEM are shown.

The DV boundary is significantly curved during mid-larval development, but its curvature is reduced towards late larval development (figure 5.1A-E). We test whether the overall boundary morphology is responsible for the observed roughness reduction. We calculate the deviation of the DV boundary from a specified curve in order to exclude the roughness associated with the global curvature. Here we fit a circle to the shape of the boundary and quantify the circle roughness as the deviation of the boundary from the fit circle. Figure 5.2C shows the circle roughness of the DV boundary at different time stages. Similar to linear roughness, we observe a reduction in the circle roughness of the DV boundary between 84h and 96h AEL. We conclude that the reduction of DV roughness is not governed by the decrease in the boundary global curvature.

5.2 Response of wing discs to ablation of cell bonds

In this section we quantify the mechanical tension on cell bonds along the DV boundary relative to the tension along the other cell bonds in the wing disc. Tissue relaxation in response to ablating single cell bonds provides a quantitative indicator of mechanical tension on cell bonds [26]. We ablate individual cell bonds using a UV-laser beam at 84h, 96h, 108h and 120h AEL. The ablation of cell bonds generates an anisotropic displacement around the cut bond. We observe the movement of the network over several minutes after ablation. We cut the bond along the DV boundary or inside dorsal and ventral compartments and compare the maximum distance increase of the vertex separation, and the displacement field near the cut bond.

Figure 5.3A-D shows the distance increase between the vertices of ablated bond over time $d(t)$. The maximal increase of distance between vertices upon cell bond ablation within the dorsal or ventral compartments are similar to each other for all time points (figure 5.3A-D, I). At 84h AEL, the vertex distance increase after ablating cell bonds along the DV boundary is slightly larger compared to ablation in the dorsal and ventral compartments (figure 5.3A). For 96h, 108h, and 120h AEL the vertex distance increase

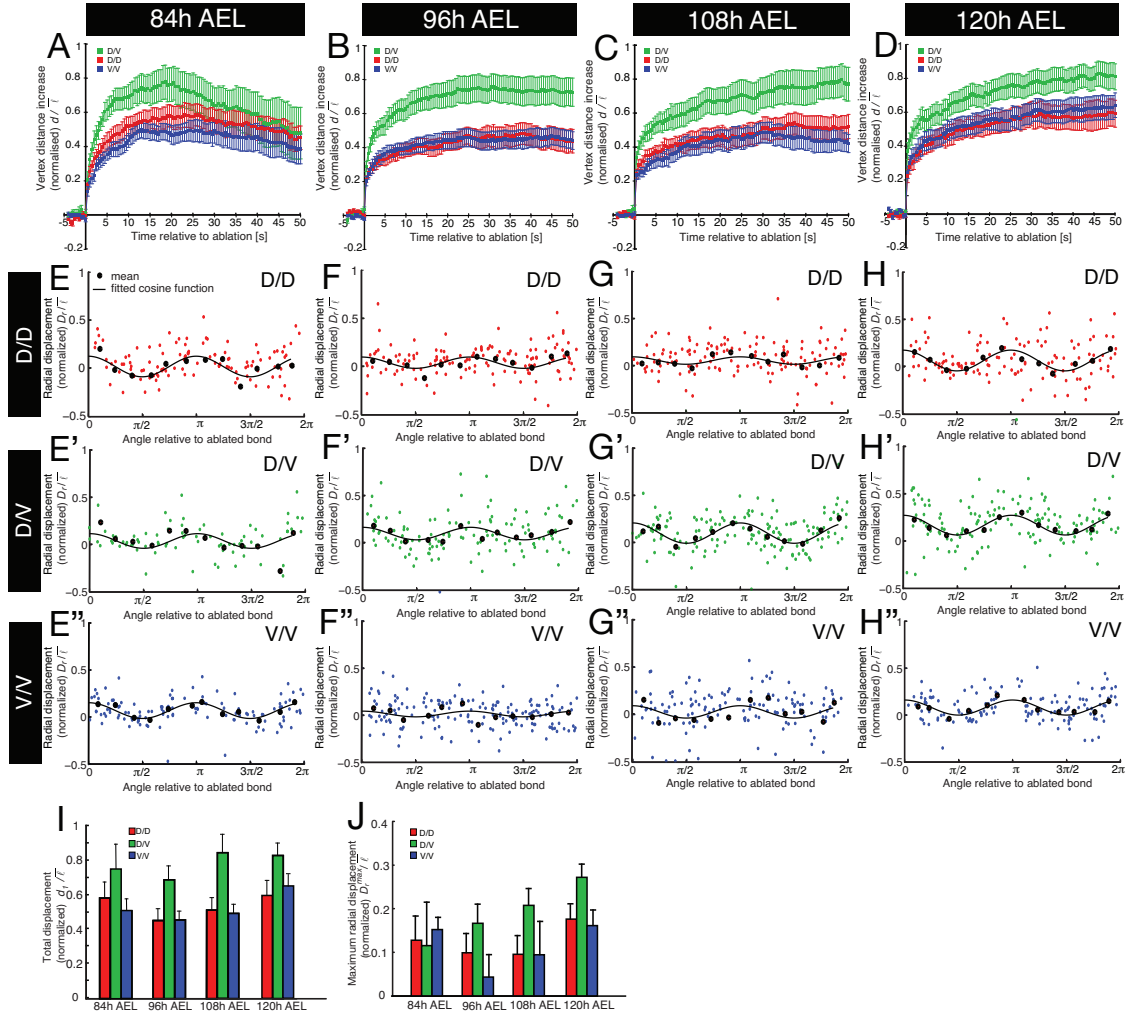


Figure 5.3: Tissue response to ablation of cell bonds. (A-D) Change in distance d between vertices at the ends of cell bonds before and after ablation as a function of time relative to ablation for wing discs at (A) 84h, (B) 96h, (C) 108h, and (D) 120h AEL. The types of ablated cell bonds are indicated. Mean and SEM are shown. (E-H) Radial displacement D_r of all the vertices located at a distance of up to two average bond lengths from the point of ablation shown as a function of the angle between the ablated bond and the line between the vertex and the point of ablation. The types of ablated cell bonds are indicated on the left and the developmental time of ablation is shown on the top. Mean values are shown for bins of $\pi/6$ (black dots). A fit of the mean values to a cosine function is shown (black line). (I) Total displacement d_1 of vertices at the ends of ablated cell bonds for the indicated types of cell bonds and developmental times. The mean and SEM of fits are shown. (J) Maximum radial displacement determined by the fits shown in (E-H^{''}). The average values and the standard error of the fits are shown. Distance and displacement values are normalized to the average bond length $\bar{\ell}$ of each time point.

is significantly larger for DV bonds as compared to bonds in the dorsal and ventral compartments (figure 5.3B-D).

We then quantify the experimentally observed radial displacements of vertices as a function of angle relative to the orientation of the ablated bond (figure 5.3E-H", J). We determine the radial displacement of vertices $D_r(\vartheta)$ as a function of the angle relative to the ablated bond ϑ . The function $a \cos \vartheta + b$ is fit to the radial displacement $D_r(\vartheta)$ and the maximum radial displacement is $D_r^{max} = a + b$. At 84h AEL, the radial displacements resulting from ablating bonds along the DV boundary and within the dorsal and ventral compartments are similar (figure 5.3E-E", J). For 96h, 108h, and 120h AEL, the radial displacements of DV bonds are increased as compared to the radial displacements of D/D or V/V bonds (figure 5.3F-H", J). These results demonstrate that cell bond tension along the DV boundary varies over developmental time. In the next chapter we will compare the displacement field of experimental cuts and simulation of laser ablation to estimate the relative bond tension along DV.

5.3 Cell division pattern in the wing imaginal disc

We next determine the relative proliferation rate of cells in the vicinity of the DV boundary compared to the cells elsewhere in the wing disc for different developmental times. Cells replicating DNA are labeled by *BrdU* incorporation and the ratio of labeled to unlabeled cells are determined. At 84h and 96h AEL, the distribution of *BrdU* labeled cells is homogeneous, and therefore, the rate of cell proliferation is similar for the cells located in the vicinity of the DV boundary and further away from this boundary (figure 5.4F,G). At 108h AEL, cell proliferation rate is reduced to approximately 0.6 – 0.7 fold in a strip of 5-10 cells centering on the DV boundary as compared to the rate of proliferation of cells located elsewhere (figure 5.4H) [55]. At 120h AEL, cell proliferation rate is reduced to approximately 0.4 – 0.5 fold within a strip of 10 – 20 cells centering on the DV boundary (figure 5.4I) [55].

To test whether this local decrease in cell proliferation is important for the morphology of the DV boundary, we increase the rate of cell proliferation by co-expressing the cell cycle regulators *string* and *Cyclin E* in the vicinity of the DV boundary [105]. As a consequence, the rate of cell proliferation in the vicinity of the DV boundary is indistinguishable from the rate of cell proliferation elsewhere in the tissue at 108h AEL [106]. The shape of the DV boundary is indistinguishable between control wing imaginal discs and imaginal discs co-expressing *string* and *CycE* (figure 5.5). We conclude that a decreased rate of cell proliferation during late larval development is not important to maintain a straight and sharp DV boundary.

5.4 Summary

In this chapter, we summarized our experimental results on the mechanics and morphology of the dorsoventral boundary in the developing fly wing. We analyzed images of the wing discs to quantify the morphology of the DV boundary and the cells in the

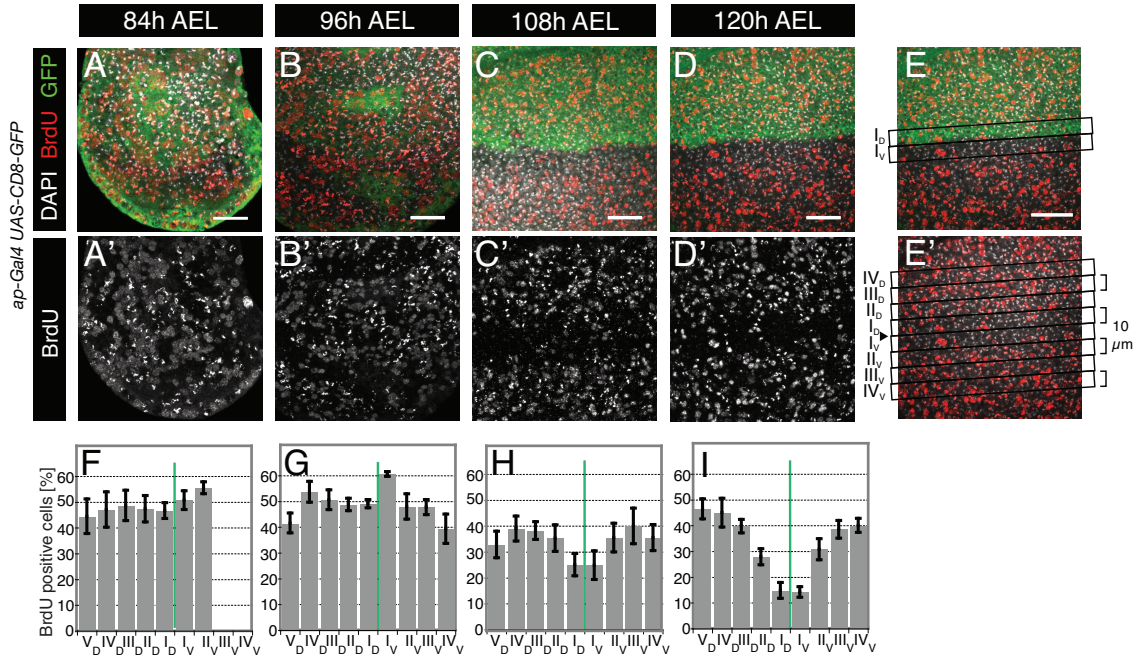


Figure 5.4: Proliferation profile near the DV boundary. (A-D) Wing imaginal discs at (A) 84h, (B) 96h, (C) 108h, and (D) 120h AEL stained for *BrdU* incorporation (red) and *DAPI* (white). The dorsal compartments are visualized by expression of *CD8-GFP* (green). Scale bars represent $20\mu\text{m}$. (E, E') Subdivision of images of stained wing discs into consecutive $10\mu\text{m}$ broad strips of cells symmetric to the DV boundary. (F-I) Percentage of *BrdU* positive cells of wing imaginal discs at (F) 84h, (G) 96h, (H) 108h, and (I) 120h AEL. I_D to V_D and I_V to IV_V refer to consecutive $10\mu\text{m}$ broad strips of cells adjacent to the DV boundary. Mean and SEM are shown ($n = 6$ (84h), 5 (96h), 5 (108h), and 6 (120h) wing imaginal discs).

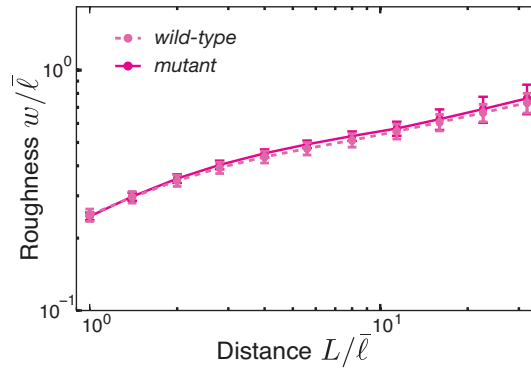


Figure 5.5: Roughness w of DV boundary as a function of distance L in the wild-type and mutant (co-expressing *string* and *CycE*) wing imaginal discs. Lengths and roughness values are normalized by average bond length $\bar{\ell}$. Mean and SEM are shown, $n = 6$.

vicinity of this boundary at different developmental stages (72h, 84h, 96h, 108h, and 120h AEL). In particular, we quantified elongation of cells and showed that cells are in average elongated along the DV boundary. We also studied the roughness of the boundary, and observed a significant reduction in the roughness of the DV boundary between 84h and 96h AEL.

By measuring tissue relaxation in response to ablation of cell bonds, we compared the mechanical tension of the bonds along the DV boundary and the bonds within dorsal and ventral compartments. We analyzed the increase in the vertex distance of the ablated bonds in time and the displacement field of the neighboring vertices. The response of the tissue to ablation of cell bonds changes during developmental time. At 84h AEL, no difference is observed between the tissue response to the ablation of bonds at different positions in the wing discs. However, at later time steps, the tissue response is more distinct when a cut bond lays along the DV boundary compared to the bonds inside the compartments. In the next chapter we compare the experiments and simulations of bond ablation to estimate the mechanical tension along cell bonds.

Furthermore, we determined the cell proliferation pattern in the wing imaginal disc for different developmental times. Our observations demonstrated that cell proliferation is reduced in the vicinity of the DV boundary compared to elsewhere in the wing disc at late larval development. However, further experiments showed that local reduction in cell proliferation rate is not required to maintain a straight and sharp DV compartment boundary.

Chapter 6

Comparison of theory and experiment

We would like to investigate the different mechanisms that play a role in shaping the dorsoventral compartment boundary during the development of the wing of the fruit fly. We reviewed our experimental results analyzing the morphology and mechanics of the DV boundary in chapter 5. We quantified the roughness of the DV boundary, elongation of cells, the proliferation rate, and cell bond tension in the wing discs at different developmental stages. On the other hand, in the chapter 4, we studied theoretically how general mechanisms influence the morphology of interfaces between two compartments during simulated tissue growth. We showed that the interfaces evolve in a dynamic process during tissue growth, and their morphology changes as a function of time. Moreover, cell bond tension, cell proliferation rate, a bias in the orientation of cell division, cell elongation, and dependence of cell proliferation rate on cell pressure have distinct effects on the shape of compartment boundaries.

In this chapter we compare our theory with the experiments to analyze the mechanisms shaping the DV boundary. We first estimate the parameters used in the vertex model based on the experimental observations discussed in the previous chapter and literature. We discuss how we estimate the relative cell bond tension along the DV boundary with simulating the ablation of cell bonds. We also describe our methods to estimate the anisotropic stress in the vertex model and the bias in cell division axis. We then analyze whether our model, using the determined parameters, can describe the time-dependent behavior of the DV boundary.

6.1 Estimate of cell bond tension

We estimate cell bond tension by analyzing the response of the tissue to the ablation of cell bonds. In section 5.2, we reviewed the experimental results denoting the response of the wing imaginal discs to the ablation of cell bonds at different time stages. We analyzed the anisotropic displacement of vertices around the cut bond and showed that the response of the wing disc varies over time. Besides, the displacements are more

pronounced when the cut bonds lie at the DV boundary compared to the bonds inside the compartments, which is an indication of increased cell bond tension along the boundary. We can estimate the relative cell bond tension along the DV boundary by comparing laser ablation results between experiments and simulations. We first introduce how to simulate the ablation of cell bonds in a vertex model and study how mechanical properties of the network influence its response to the bond ablation.

6.1.1 Simulation of bond ablation in the Vertex model

We simulate the ablation of cell bonds in the vertex model to quantify cell bond tension [83]. In a stable cell network, one bond is selected to be cut and the line tension of the bond Λ_{ij} is set to zero spontaneously. Furthermore, the perimeter elasticity of the two cells α and β sharing the cut bond Γ_α and Γ_β is set to zero. The network is then relaxed to a new stable configuration. We analyze the displacement of the vertices around the cut bond as described in the previous chapter (section 5.2). We determine the radial displacement of vertices, $D_r(\vartheta)$, as a function of the angle relative to the ablated bond, ϑ . We use the maxima of radial displacement to compare different cuts.

At first, we would like to address this question whether the response of tissue to laser ablation depends on generation or system size. Figure 6.1A,B shows two examples of the displacement fields in response to the ablation of cell bonds within a cellular network for two different generations 3 and 6. The displacement fields and the cosine function fits look very similar. We repeat the simulation of laser ablation for different generations and average the fit values over different examples. Figure 6.1C shows the average value of maximal displacement for different generations, ranging between 0 and 7. The maximal radial displacement is constant for different generations except for the initial configuration $G = 0$, which corresponds to a hexagonal network.

The response of cellular networks to the ablation of cell bonds depends on the tissue mechanics. We discussed that mechanical properties of cellular networks are described by different parameters denoting cell bond tension, perimeter elasticity, anisotropic shear stress and division rates. We study how individual parameters affect the response of cellular networks to the ablation of cell bonds. Displacement fields upon bond ablation are mainly influenced by bulk bond tension $\bar{\Lambda}_0$ and perimeter elasticity $\bar{\Gamma}$, as well as the relative bond tension at the interface λ for the cuts at the interface. However increasing external shear stress $\bar{\Sigma}$, or reducing division rate β have minor effects on the ablation results, at least within the range consistent with the observed quantities in the wing imaginal disc.

6.1.2 Estimate of the relative bond tension along DV

In this section we discuss how to estimate the relative cell bond tension along the DV boundary compared to the bonds within the compartments. The most robust estimate is obtained by comparing the radial displacements fields in the vicinity of the ablation between experiments and simulations. In the previous chapter, we quantified the experimentally observed displacement fields of vertices in the vicinity of bonds within the

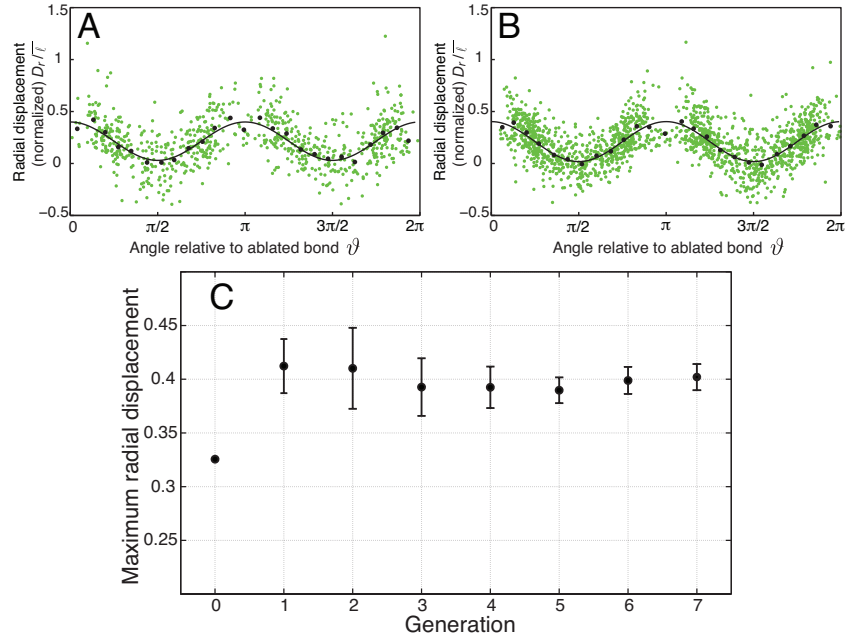


Figure 6.1: Response of cellular networks to bond ablation at different generations. (A-B) Radial displacement $D_r(\vartheta)$ of all vertices located at a distance of up to two average bond lengths from the point of ablation shown as a function of the angle ϑ between the ablated bond and the line between the vertex and the point of ablation, (A) $G = 3$, (B) $G = 6$. (C) Maxima of radial displacements obtained from simulations with constant mechanical properties at different stages. Displacements are normalized by the average bond length \bar{l} . For all simulations $\bar{\Lambda} = 0.12$, $\bar{\Gamma} = 0.04$, and $\lambda = 1$.

dorsal and ventral compartments and along the DV boundary (figure 5.3). To estimate the relative bond tension along the boundary, we first need to quantify the bulk properties.

To estimate $\bar{\Lambda}_0$ and $\bar{\Gamma}$, we compare the maximum radial displacement, D_r^{max} , obtained in simulations for different choices of $\bar{\Lambda}_0$, and $\bar{\Gamma}$, when $\lambda = 1$ to the value of D_r^{max} obtained experimentally by the ablation of bonds within the dorsal and ventral compartments. This procedure is repeated for different time steps, 84, 96, 108, and 120h AEL, to find the bulk parameters for which the maxima radial displacement fits the best with the experimental value. Interestingly, the maximum radial displacements resulting from ablating cell bonds within the dorsal or ventral compartments are increased at 120h AEL compared to earlier time points, indicating that the average cell bond tension in the tissue increases during late larval development (figure 6.2).

For each developmental stage, we use estimated bulk parameters $\bar{\Lambda}_0$ and $\bar{\Gamma}$ and repeat the ablation simulation for different choices of the relative bond tension along the interface λ . In figure 6.2, the maxima radial displacement is shown as a function of λ for different sets of bulk parameters corresponding to the developmental stages.

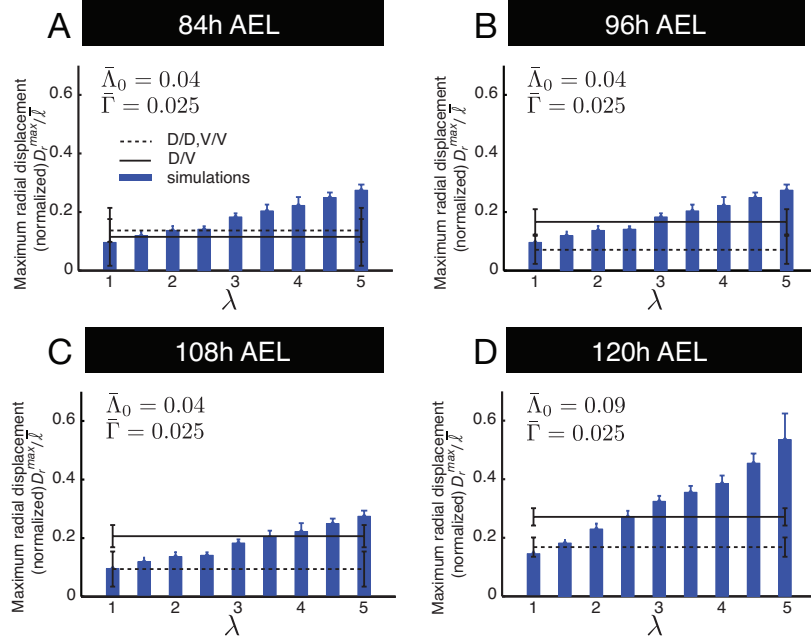


Figure 6.2: Maxima of radial displacements obtained from simulations of cell bond ablations with different values of λ are shown as blue bars. The values of $\bar{\Lambda}$ and $\bar{\Gamma}$ used in the simulations are indicated. Maxima of radial displacements for ablated DV bonds (black line) and average of D/D and V/V bonds (dashed black line) for laser ablations at (A) 84h, (B) 96h, (C) 108h, and (D) 120hAEL are shown. For experimental data the average values and the standard error of the fits are shown. For simulations, mean and SEM are shown ($n = 10$ realizations).

We estimate the relative bond tension along DV, λ , by comparing these plots with the maximum radial displacement of cell bonds along the DV boundary.

Our observations demonstrate that at 84h AEL, the maximal radial displacements resulting from ablating bonds along the DV boundary and within the dorsal and ventral compartments are similar (figure 6.2A). It indicates that there is no increased cell bond tension along the DV boundary compared to the other bonds. However, for 96h, 108h, and 120h AEL, the maximal radial displacements of DV bonds are increased as compared to the maximal radial displacements of D/D or V/V bonds. The maximum radial displacements in response to laser ablations at 96h, 108h, or 120h AEL corresponds to values of λ between 2.5 and 3.0 (figure 6.2B-D). Further experiments show that cell bond tension at the bonds between the first and second row of dorsal cells (D1/D2) or between the first and second row of ventral cells (V1/V2) is almost the same as the bonds inside the compartments.

We can conclude that cell bond tension along the DV boundary varies over developmental time. Relative cell bond tension along the DV boundary increases between 84h and 96h AEL. Interestingly, the increase in cell bond tension along the DV boundary

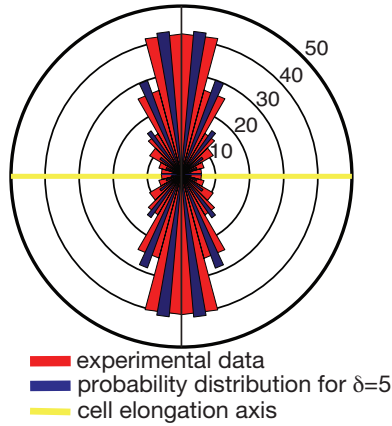


Figure 6.3: The comparison between the probability distribution of the cleavage plane orientation from the cell elongation axis in the wing discs [76] and the function for the probability of division orientation equation 3.4 for $\delta = 5$. The yellow line shows the axis of cell elongation that is used as the reference angle for each cell. The orientation probabilities, shown in percent, are averaged within $\pi/12$ angle intervals. The angles range $[0, \pi/2]$ and are shown in the three other quadrants symmetrically.

coincides with the observed reduction of roughness (figure 5.2). Later in this chapter we address the question whether the reduction of the DV roughness is generated by the increase in the relative bond tension at the DV boundary.

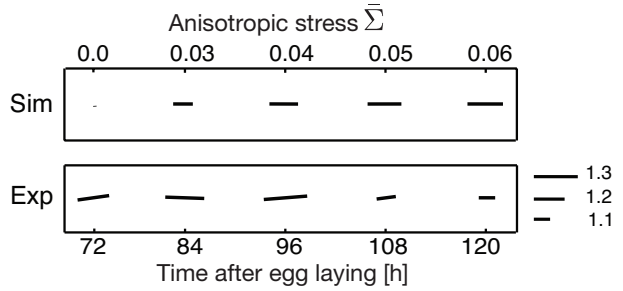
6.2 Estimation of the bias in the division axis

There are experimental evidences showing that the orientation of cell division is biased in the vicinity of the DV boundary such that the division plane is frequently perpendicular to the DV boundary [24, 57]. It has been proposed that oriented cell division might influence boundary shape [24, 58]. Experimental observation in different tissues and particularly in the wing imaginal discs show that cell elongation affects the orientation of cell division axis [76]. This effect, in combination with the observed cell elongation along the DV boundary, can lead to oriented cell division along the DV boundary.

In our model cell division axis can be influenced by cell elongation, where δ describes the strength of this effect (introduced in section 3.3.2). We estimate the value of δ based on the observed distribution of the orientation of the cleavage plane with respect to cell elongation axis in the wing disc [76]. We use a typical value of elongation of individual cells, $\varrho = 0.3$, in the wing discs and calculate the probability distribution of the new bond direction with respect to cell elongation axis for different values of δ . Our results show that $\delta = 5$ presents the best agreement with the observed distribution of cell division orientation in the wing imaginal discs (see figure 6.3).

It should be noted that this estimate is based on a mean field approximation, whereas the experimental data describe the mean distribution of the cleavage plane orientation, independent of the strength of cell elongation. For a better estimate, one needs to quantify the correlation between cell elongation and the cleavage plane orientation of individual cells.

Figure 6.4: Comparison of the average cell elongation between simulation (Sim) for the indicated values of $\bar{\Sigma}$ and wing disc at the indicated time AEL (Exp). The length of the bars represents the ratio of long to short axis of a cell parallel to the DV boundary.



6.3 Estimation of anisotropic stress

We now estimate the strength of anisotropies in the wing imaginal disc. Analysis of the images of the wing discs shows that cells are typically elongated along the DV boundary at different stages (figure 5.1). We do not know the origin of the anisotropies in the wing disc, however, in a simple picture we consider it in our model by applying external shear stresses. In section 3.1, we discussed that cells get elongated when a shear stress is applied to the cellular network. The average cell elongation is controlled by the strength of shear stress $\bar{\Sigma}$. We observed that the elongation of cells influences the morphology of the interface although it does not lead to an effective interfacial tension (figure 4.14). We speculate whether tissue anisotropies contribute to shaping the DV boundary.

To estimate an appropriate choice of external shear stress, $\bar{\Sigma}$, in our model, we compare the elongation of cells in the cellular networks with average cell elongation in the wing imaginal discs. For this purpose we simulate the growth of tissues where a constant $\bar{\Sigma}$ is applied to the tissue and all the cells are identical. We should note that the elongation of cells is quite constant during growth. Moreover, it changes negligibly with local increase of bond tension along the interface if the tissue is large enough.

In figure 6.4, we plot the average cell elongation in a network generated by simulation of growth for different values of external anisotropic stress $\bar{\Sigma}$. This is compared to the average cell elongation quantified in the wing disc within 20 cell rows around the DV boundary at different stages during development. We find that dimensionless shear stress $\bar{\Sigma} = 0.05$ leads to comparable cell shapes as observed in the wing discs.

6.4 Simulations accounting for the time-evolution of the DV morphology

Quantifying the morphology and mechanics of the cells in the vicinity of the DV boundary allowed us to estimate the strength of different mechanisms. In this section we study whether experimentally estimated parameters can account for the time evolution of the morphology of the DV boundary. Especially we investigate whether increasing the relative cell bond tension along the DV boundary drives the reduction of its roughness, and whether reduced proliferation rate, elongated cells, or oriented cell division play a role in shaping the DV boundary.

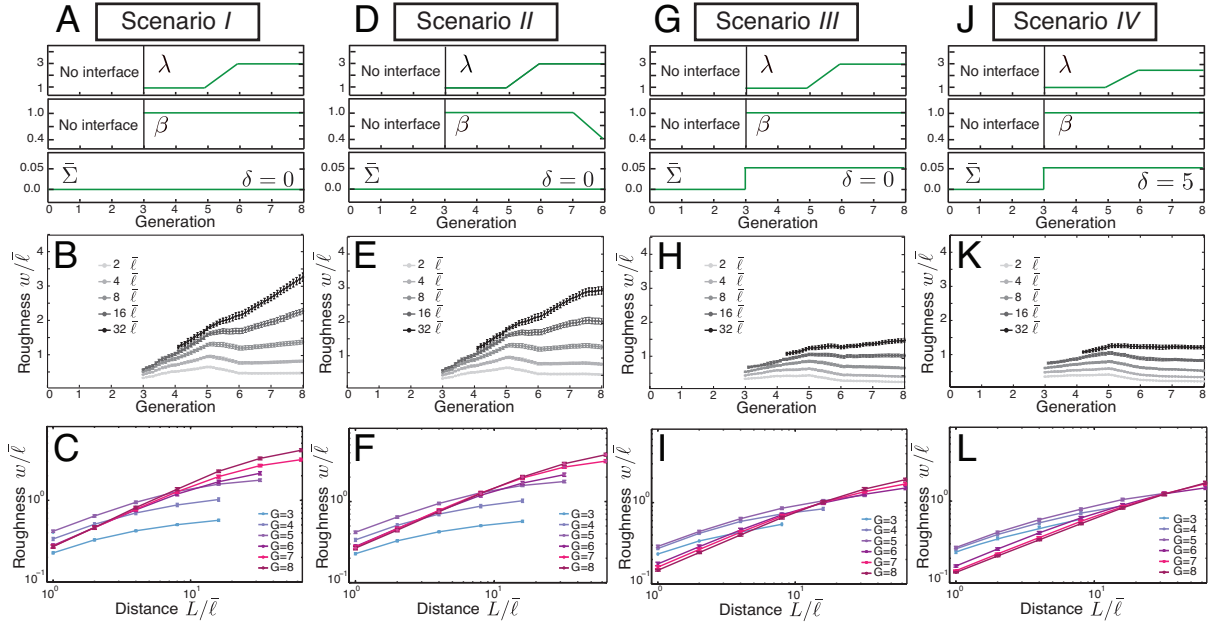


Figure 6.5: Mechanisms shaping the DV boundary during development. (A-L) A straight interface is introduced in the tissue at $G = 3$. All the cells are identical until $G = 5$. Cell bond tension is increased along the interface between generation five and six and it remains constant afterwards. The first line (A, D, G, J) depicts the values of the parameters used in the simulations as a function of generation number. The second line (B, E, H, K) depicts the roughness w of the interface as a function of generation G for the indicated distances L along the interface. The third line (C, F, I, L) shows the roughness w of the interface as a function of the distance L for the generations G indicated. Distance and roughness values are normalized by $\bar{\ell}$. Mean and SEM are shown ($n = 10$ realizations). (A-C) Scenario I: Relative cell bond tension along the interface is increased by a factor $\lambda = 3$ at generation six. (D-F) Scenario II: Relative cell bond tension along the interface is increased by a factor $\lambda = 3$ at generation six. The rate of cell division is reduced during the last generation by a factor $\beta = 0.4$ in five rows of cells on both sides of the interface. (G-I) Scenario III: Anisotropic stress of the relative strength $\bar{\Sigma} = 0.05$ is applied to stretch the network parallel to the interface after generation three. Relative cell bond tension along the interface is increased by a factor $\lambda = 3$ at generation six. (J-L) Scenario IV: Orientation of cell division is biased by a coefficient $\delta = 5$. Anisotropic stress of the relative strength $\bar{\Sigma} = 0.05$ is applied to stretch the network parallel to the interface after generation three. Relative cell bond tension along the interface is increased by a factor $\lambda = 2.5$ at generation six.

For this purpose we perform simulations of tissue growth during eight rounds of cell division which approximately corresponds to the number of cell divisions that takes place in the wing disc between 48h and 120h AEL [107]. We start from a hexagonal network of identical cells. There is no compartmentalizing in the initial configuration up to the third generation. To resemble the establishment of the DV boundary, at third generation a boundary separating two cell populations is introduced in the cellular network. The introduced boundary is straight with some perturbations of one mean bond length width. In our simulations, relative cell bond tension at the interface is not increased until generation 5. Then cell bond tension along the interface is linearly increased by $\lambda = 3$ between generation 5 and 6 and remains constant afterwards (figure 6.5A). We observe that an increase in relative cell bond tension can lead to reductions of interface roughness during this period (figure 6.5A-C), similar to the roughness decrease observed in the experiments. However, the interface is significantly rougher than the DV boundary observed in the wing discs (compare to figure 5.2).

We next analyze how other mechanisms influence the shape of the boundary. Due to the experimental evidence, cell proliferation is reduced in the vicinity of the DV boundary at later time points (section 5.3). In the second scenario, we reduce the division rate to 40% in five rows of cells on both sides of the boundary between generation seven and eight (figure 6.5D). It is similar to what is observed in the wing disc (figure 5.4F-I). The interface roughness is very similar to scenario *I*, and barely reduced at very late generation (figure 6.5D-F). This indicates that changes of cell proliferation rate near the DV boundary at late stages of development have a weak effect on the morphology of the interface, consistent with our experimental findings (section 5.5).

In scenario *III* we take into account that cells are elongated parallel to the boundary by subjecting the system to an externally applied anisotropic stress. Our theoretical study showed that this mechanism leads to more straight interfaces (figure 4.14). Here we analyze the contribution of this mechanism to shaping the DV boundary. We apply a constant shear stress $\bar{\Sigma} = 0.05$, as estimated in section 6.3, to the network starting from generation three. It is combined with a local increase in cell bond tension between generation 5 and 6 (figure 6.5G). In this scenario, the interfaces are more straight compared to scenario *I* and *II* and the roughness values are close to the roughness of the DV boundary. However, the roughness does not decrease as much as observed for large distances (figure 6.5G-I).

The last scenario is similar to scenario *III*, except that we also take into account the oriented cell division. In this scenario cell division orientation is biased by cell elongation with $\delta = 5$ as estimated in figure 6.3. Besides, the relative cell bond tension along the interface increases to $\lambda = 2.5$ at the sixth generation. With this scenario we observe interfaces which look very similar to the DV boundary (figure 6.5K-L and figure 6.6). We observe interface roughness decreases for small and large distances when cell bond tension is increased. More importantly roughness values are very similar to the roughness of DV boundary at different developmental stages. This mechanism can quantitatively account for the main features of the observed time-evolution of the DV boundary morphology during development.

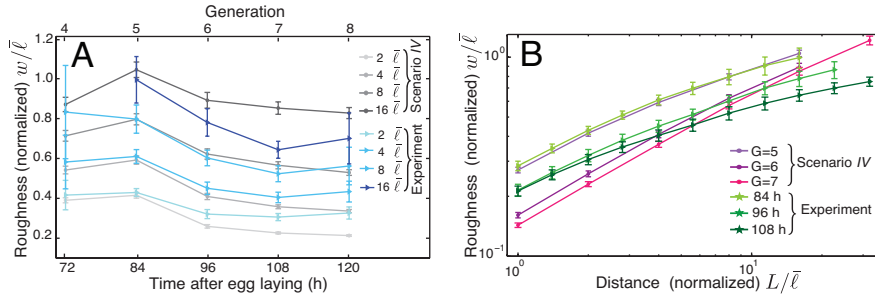


Figure 6.6: (A) Comparison between the roughness of the DV boundary (experiment) for different times AEL and the roughness of the simulation in scenario *IV* at different generations for the indicated distances L along the interface. (B) Comparison between the roughness of the DV boundary (experiment) at the indicated times AEL and the roughness of the interfaces in scenario *IV* at different generations indicated as a function of the distance L along the interface.

Despite the good agreement between the experimental observation and the suggested scenario, some differences are still noticeable. This scenario leads to less roughness reduction for large scales and more for short scales, compared to the reduction of the DV roughness. We tested another mechanism, when cell division probability is affected by cell pressure. It did not affect the interface morphology, even if combined with anisotropic stress and increased bond tension at the interface. We also took into account the time evolution of the bulk parameters $\bar{\Lambda}_0$ and $\bar{\Gamma}$, according to what observed in figure 6.2. However, it has no significant influence on the reduction of the interface roughness.

There are other candidates for the additional mechanisms which may help to improve the suggested scenario. For example chemical signaling can change cell mechanics or growth rate in a way that the division rate would be different on both sides of a bump. Therefore cell proliferation straighten the bump. Importantly, tissues remodel actively in the time scales smaller than a cell division. Cell rearrangements are governed by cell division, T1 and T2 transitions in the vertex model. However, it is more complicated in the live tissues where everything is much more dynamic. For example, tension along cell bonds may fluctuate or there can be some other noises in the system. These noises lead to annealing of the network toward other minima of energy function. We speculate whether this mechanism changes the morphology of compartment boundaries.

6.5 Summary

In this chapter we compared our theory with the experiments of the dorsoventral boundary in the wing imaginal disc. We estimated the parameters used in our model with the help of the quantified experimental results. We first introduced how to simulate the ablation of cell bonds in the vertex model. We determined the displacement field of the vertices near the cut bond and compared the maximum radial displacement from

experiments to simulations. We discussed how we estimate the relative cell bond tension along the DV boundary with comparing the displacement field of cellular networks in response to the ablation of cell bonds between experiments and simulations. Our results demonstrate that cell bond tension along the DV boundary varies over developmental time. At 84h AEL, cell bond tension along the DV boundary is similar to cell bond tension in the dorsal and ventral compartments. By contrast, from 96h to 120h AEL, cell bond tension along the DV boundary is approximately increased by a factor $\lambda = 2.5-3$. Furthermore, we determined the strength of the bias in cell division axis, based on the distribution of the orientation of the cleavage plane observed in the wing disc. Finally, by comparing average cell elongation in experimental images and simulations, we estimated the external shear stress.

We then used the estimated parameters in our model and studied whether they can explain the time-evolution behavior of the DV boundary. We showed that a local increase in cell bond tension along the interface can account for the decrease in its roughness from 84h to 96h. We took into account additional mechanisms and compared the roughness of interfaces between the simulations and experiments. We concluded that a combination of increased cell bond tension, cell elongation/stress, and oriented cell division are the key mechanisms to shape the DV boundary during wing development. The suggested mechanism predicts the time-dependence of the morphology of the DV boundary very well.

Chapter 7

Conclusion

In this work, we have studied the mechanics and dynamics of interfaces between cellular compartments. Separating compartments of distinct cell lineage by straight and sharp boundaries is important for growth and pattern formation during animal development. We presented a theoretical analysis of interfaces in a coarse-grained description as well as a vertex model. With the help of these models, we showed that interfaces evolve in time due to the interplay of cell dynamics and tissue mechanics. Using a continuum model for the growth of active tissues, we showed that an interface can propagate between two cell populations with different mechanical properties. With the help of a vertex model, we proposed different general mechanisms which shape the compartment boundaries in developing tissues. By comparing our theoretical results with quantified experimental observations, we showed that local increase of cell bond tension along the interface as well as global anisotropies in the tissue contribute to shaping the DV boundary in the developing wing.

We presented different tools and results throughout the thesis, including physical theories, mathematical derivations, numerical calculations, and quantitative analysis of experiments. First of all, we studied a passive binary fluid with the help of the Ginzburg-Landau model at thermodynamic equilibrium and out of equilibrium. In the non-equilibrium case, where an external field breaks the symmetry of the system, a traveling wave solution exists in which the interface moves with a constant velocity. Analyzing the stress profile in such a two-component fluid, the anisotropic stress does not vanish near the interface and is proportional to the interaction of two components. We demonstrated how to calculate the effective interfacial tension by integrating the anisotropic stress near an overall straight interface. This is a valuable method to obtain interfacial tension and can be generalized to be applicable to curved interfaces.

We presented the basic concepts of a coarse-grained description of cellular compartments in active tissues. This model is based on the balance of cell numbers and conservation of momentum, including active terms which are responsible for cell division and apoptosis. We analyzed the interesting case when two cell populations with different homeostatic pressures meet. The difference in the homeostatic pressures drives the propagation of the interface, corresponding to the invasion of one cell type into the other.

We showed that the dynamics of the system is determined by a generalized version of the Fisher equation, which takes into account the coupling between cell number balance and tissue mechanics. We calculated the profile of the moving interface and its velocity as a function of the relevant parameters. Linearizing the dynamic equations near the unstable front allows us to analyze some interesting features of interface propagation. For localized initial conditions the system either reaches a pulled front or a pushed front solution, depending on the parameter values. Our theoretical analysis confirms that these two regimes are separated by a sharp transition.

The continuum description of interfaces in tissues can be expanded in several directions. We can use this approach to study interface propagation in other geometries. For example, the cylindrical or spheroidal geometry are more realistic for a small clone of cells surrounded by the host tissue. We expect that for large curvatures of interfaces, the dynamics is controlled by the effective interfacial tension. Moreover, in this model we consider tissues as incompressible fluids. However, tissues effectively behave as viscoelastic materials. Especially for short time scales they are better captured by elastic descriptions. It is worthwhile to study whether elastic response of cells has any effect on the dynamics of interfaces. Furthermore, the deterministic equations studied here can be extended by taking into account noises. Noises originate from the stochastic feature of cell division and cell death as well as fluctuations in cell mechanics or cell shape. It is very interesting to study whether the wave speed and the front shape are modified considering the noises in the system. In such a system interface morphology will also be affected by noises and it will be possible to analyze the roughness of interfaces.

We also used a vertex model to study an epithelium at the level of adherens junctions. Using this vertex model, we studied the growth of a cellular network involving two adjacent cell populations separated by an interface. We proposed general physical mechanisms and studied how each mechanism contributes to the dynamics of interfaces during growth. We studied the stress distribution inside the tissue and calculated the effective interfacial tension from the profile of the anisotropic stress. In the reference case, including two compartments of identical cells, the effective interfacial tension vanishes. We studied how different mechanisms contribute to the effective interfacial tension. An effective interfacial tension is achieved when cell bond tension is increased at the interface or when cell proliferation is reduced in the vicinity of the interface. Applying external shear increases the interfacial tension if combined with increased bond tension at the interface. However, the interfacial tension remains unchanged when orientation of cell division is biased by cell elongation.

Moreover, we quantified the morphology of interfaces for different mechanisms. Our growth simulations confirm that an initially straight interface becomes rough due to the stochastic behavior of cell divisions. The interface roughness also increases with increasing distance along the interface. We investigated the influence of different mechanisms on time dependence of the interface morphology. Increased cell bond tension and reduced cell proliferation lead to overall reduction of values of roughness compared to the reference case. Interestingly, a significant reduction of roughness can also result from overall cell elongation in the tissue parallel to the interface. Strikingly, in conjunction

with increased cell bond tension, a bias in orientation of cell division by cell elongation can significantly reduce interface roughness. Thus, local effects at the interface as well as global anisotropies within the whole tissue contribute to shaping interfaces in cell networks.

Finally, we combined our theoretical results with quantitative experiments to investigate the role of different physical mechanisms for shaping the DV compartment boundary in the fly wing. By analyzing the images of the wing disc, we quantified the roughness of the DV boundary and the morphology of cells at different developmental times. Notably, the roughness starts with comparably high values, however, is then reduced from mid-to-late third instar. By measuring tissue relaxation in response to laser ablation of cell bonds at different developmental times, we demonstrated that the decrease in boundary roughness correlates with an increase in cell bond tension along the compartment boundary. We estimated the relative increase in cell bond tension along DV by comparing the experimental data to simulations of laser ablations in the vertex model.

Cells in the vicinity of the DV boundary are elongated parallel to this boundary. This elongation is a signature of tissue anisotropies that could play a role in interface morphology. In our model, we studied the simple case of cell elongation induced by externally applied stresses, which strongly affects the interface morphology. We estimated the external shear by comparing average cell elongation in wing discs and simulations. We also proposed that the bias in the orientation of cell division by cell elongation influences the shape of the DV boundary.

In the wing imaginal disc, cell proliferation is reduced in the vicinity of the DV boundary during late larval development. However, with additional experimental evidence and further simulations we concluded that the reduction of cell proliferation rate is not important for the morphology of the DV boundary in the fly wing disc. This mechanism can play a role for shaping other compartment boundaries. Taken together, by using experimentally determined values for cell bond tension, cell elongation and bias in orientation of cell division in our model of tissue growth, we could reproduce the main features of the time-evolution of the DV boundary shape.

Our analysis on the mechanics and dynamics of the DV boundary can be extended in different ways. Despite the very good agreement between the experimental observation and the suggested scenario, some differences exist, especially for the roughness of large scales. We speculate whether there are additional mechanisms which may improve the suggested scenario. It should be also mentioned that the origin of cell elongation in the wing imaginal disc is not well understood. It may be governed by external shear forces, or there can be some molecular mechanisms underlying tissue anisotropies [108]. It is still a challenge to identify the mechanisms that control the patterns of cell elongation. Moreover, it will be useful to have a quantified analysis representing the correlation between cell division orientation and the elongation axis of individual cells. It helps to have a more realistic description of the oriented cell division. More importantly, the establishment of the DV boundary is still unknown. Any observation about the exact timing of the DV establishment or the underlying mechanisms will be crucial. We hope

that the novel improvements in experiments can help to clarify many of the unknown issues. For instance, live imaging of wing discs can give a clearer picture of the processes which influence the dynamics of compartment boundaries.

At the end it should be mentioned that the physical description of interfaces presented in this work is highly general. Our theoretical approaches and results can be applied to analyze the dynamics of interfaces in different tissues. Remarkably, the general physical mechanisms studied in this thesis can play a role in shaping other compartment boundaries. Previous works have demonstrated an increase in mechanical tension confined to cell bonds along the anteroposterior compartment boundary in the wing imaginal discs [4]. Thus, a local increase in mechanical tension might be a common principal mechanism to maintain straight and sharp compartment boundaries in developing tissues. It is also worthwhile to investigate whether tissue anisotropies, oriented cell division, or decreased proliferation play any role in shaping other compartment boundaries. We also hope that the tools developed for analyzing interfaces will be used in the future to propose other mechanisms which affect the dynamics of interfaces in developing tissues.

Appendix A

The Ericksen stress tensor

We want to derive the Ericksen stress for a two component fluid. The free energy density of the fluid is a function of the volume fraction ψ and its derivatives, $f = f(\psi, \partial_\alpha \psi)$. We consider a volume change from V to $V + \delta V$ and calculate the free energy change [109]

$$\begin{aligned}
 \delta F &= \int_{V+\delta V} d^3\mathbf{r} f(\psi + \delta\psi, \partial_\alpha \psi + \delta\partial_\alpha \psi) - \int_V d^3\mathbf{r} f(\psi, \partial_\alpha \psi) \\
 &= \int_{\delta V} d^3\mathbf{r} f(\psi, \partial_\alpha \psi) + \int_V d^3\mathbf{r} \frac{\partial f}{\partial \psi} \delta\psi + \int_V d^3\mathbf{r} \frac{\partial f}{\partial(\partial_\alpha \psi)} \delta\partial_\alpha \psi \\
 &= \int_{\delta V} d^3\mathbf{r} f(\psi, \partial_\alpha \psi) + \int_V d^3\mathbf{r} \frac{\partial f}{\partial \psi} \delta\psi - \int_V d^3\mathbf{r} \partial_\alpha \left(\frac{\partial f}{\partial(\partial_\alpha \psi)} \right) \delta\psi + \int_S dA_\alpha \frac{\partial f}{\partial(\partial_\alpha \psi)} \delta\psi \\
 &= \int_{\delta V} d^3\mathbf{r} f(\psi, \partial_\alpha \psi) + \int_V d^3\mathbf{r} \frac{\delta f}{\delta \psi} \delta\psi + \int_S dA_\alpha \frac{\partial f}{\partial(\partial_\alpha \psi)} \delta\psi . \tag{A.1}
 \end{aligned}$$

Here the functional derivative of f is introduced as $\frac{\delta f}{\delta \psi} = \frac{\partial f}{\partial \psi} - \partial_\alpha \left(\frac{\partial f}{\partial(\partial_\alpha \psi)} \right)$. If cell number is conserved, we can write

$$\int_V d^3\mathbf{r} \delta\psi = - \int_{\delta V} d^3\mathbf{r} \psi . \tag{A.2}$$

Moreover, the integral over volume in δV can be replaced by a surface integral $dV = u_\beta dA_\beta$. Here \mathbf{u} is normal to the surrounding surface and describes the change from V to $V + \delta V$. With the same approach, we can use the expression $\delta\psi = -(\partial_\beta \psi) u_\beta$ for the change in the volume fraction. With these assumptions, the free energy change is

$$\delta F = \int_S dA_\beta u_\beta f(\psi, \partial_\alpha \psi) - \int_S dA_\beta u_\beta \frac{\delta f}{\delta \psi} \psi - \int_S dA_\alpha \frac{\partial f}{\partial(\partial_\alpha \psi)} u_\beta \partial_\beta \psi . \tag{A.3}$$

Using this relation, the Ericksen stress reads

$$\sigma_{\alpha\beta}^e = (f - g) \delta_{\alpha\beta} - \frac{\partial f}{\partial(\partial_\alpha \psi)} \partial_\beta \psi , \tag{A.4}$$

where $g = \psi \frac{\delta f}{\delta \psi}$. This method can be used to obtain stress components for the Ginzburg-Landau free energy (section 2.1.2).

Appendix B

Stresses and force balance at cellular vertices

In this Appendix we analyze the force balance of the stress tensor at the vertices in cellular networks. We introduced the expression for the stress in the vertex model in section 3.4.1. We showed that the stress tensor satisfies force balance inside the cells and along the cell bonds. However, the stress tensor should fulfill force balance at the vertices as well. Here we calculate stress components at the vertices and verify the validity of force balance at these points.

B.1 Stress tensor at cell vertices

The stress at the vertices consists of different terms describing the stress along different bonds which intersect at the vertex. We consider a general picture where three cell bonds meet at a vertex as illustrated in figure B.1. The vertex is shared between three cells α , β , and γ . The total stress at the vertex can be split into an area pressure and stresses along cell bonds. The area pressure is a combination of area pressure of the cells around the vertex

$$P_A = P_\alpha \Theta(-x) \Theta(x \cos \theta_1 + y \sin \theta_1) + P_\beta \Theta(x) \Theta(-x \cos \theta_2 - y \sin \theta_2) + P_\gamma \Theta(-x \cos \theta_1 - y \sin \theta_1) \Theta(x \cos \theta_2 + y \sin \theta_2), \quad (\text{B.1})$$

where P_α , P_β , and P_γ are the area pressures of cells α , β , and γ as introduced in equation 3.9. The domain of each cell in the vicinity of the specified vertex is defined by Heaviside functions $\Theta(x, y)$ (see equation 3.12).

The stress at each cell bond includes a term describing the effective tension at the bond and some terms ensuring the constraint that the bond is straight. Equation 3.14 shows the stress tensor near each bond in its local coordinate system. It should be transformed rotationally in order to calculate stresses in the global coordinate system (like equation 3.21). Summing up the stresses along the intersecting cell bonds, the total

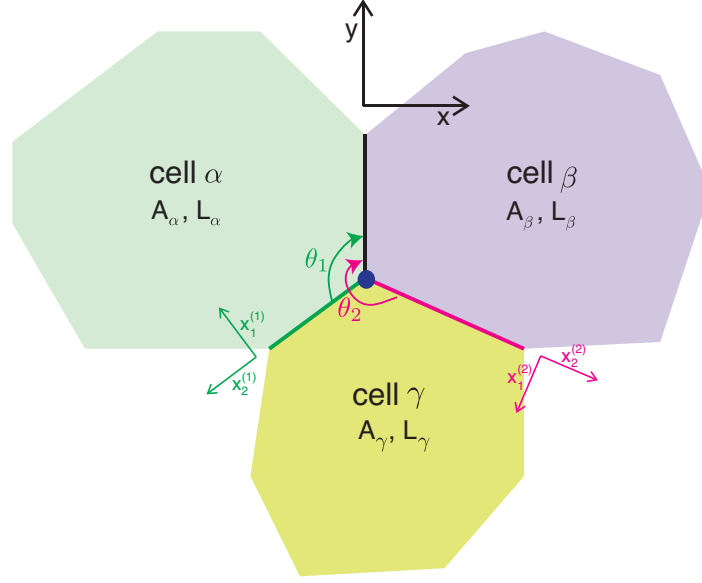


Figure B.1: A schematic view of a vertex (blue big dot) shared between three cell α (with area A_α and perimeter L_α), cell β (with area A_β and perimeter L_β), and cell γ (with area A_γ and perimeter L_γ). The vertex is the intersection of three cell bonds 0 (shown in black), 1 (shown in green), and 2 (shown in pink). Each cell bond has a local coordinate system. The local coordinate system of bond 0 is the same as the global coordinate system, shown by (x, y) . The local coordinate system of bond 1 and 2 are respectively shown by $(x_1^{(1)}, x_2^{(1)})$ and $(x_1^{(2)}, x_2^{(2)})$, which can be transformed to the global coordinate system by a rotation with the angles θ_1 and θ_2 .

stress at the vertex is

$$\begin{aligned}
\sigma_{xx} = & -P_A + \sin^2 \theta_1 \Theta(y \cos \theta_1 - x \sin \theta_1) [T_1 \delta(x \cos \theta_1 + y \sin \theta_1) \\
& + \frac{1}{2} \Delta P_{\alpha\gamma} (y \cos \theta_1 - x \sin \theta_1) (-l_2 + y \cos \theta_1 - x \sin \theta_1) \delta'(x \cos \theta_1 + y \sin \theta_1)] \\
& + \sin^2 \theta_2 \Theta(y \cos \theta_2 - x \sin \theta_2) [T_2 \delta(x \cos \theta_2 + y \sin \theta_2) \\
& - \frac{1}{2} \Delta P_{\beta\gamma} (y \cos \theta_2 - x \sin \theta_2) (-l_1 + y \cos \theta_2 - x \sin \theta_2) \delta'(x \cos \theta_2 + y \sin \theta_2)] \\
& + \Delta P_{\alpha\gamma} \sin 2\theta_1 \left(\frac{l_2}{2} - y \cos \theta_1 + x \sin \theta_1 \right) \delta(x \cos \theta_1 + y \sin \theta_1) \Theta(y \cos \theta_1 - x \sin \theta_1) \\
& + \Delta P_{\beta\gamma} \sin 2\theta_2 \left(\frac{l_1}{2} - y \cos \theta_2 + x \sin \theta_2 \right) \delta(x \cos \theta_2 + y \sin \theta_2) \Theta(y \cos \theta_2 - x \sin \theta_2) ,
\end{aligned} \tag{B.2}$$

$$\begin{aligned}
\sigma_{yy} = & -P_A + \Theta(y) [T_0 \delta(x) - \frac{1}{2} \Delta P_{\alpha\beta} y (-l_0 + y) \delta'(x)] \\
& + \cos^2 \theta_1 \Theta(y \cos \theta_1 - x \sin \theta_1) [T_1 \delta(x \cos \theta_1 + y \sin \theta_1) \\
& \quad + \frac{1}{2} \Delta P_{\alpha\gamma} (y \cos \theta_1 - x \sin \theta_1) (-l_2 + y \cos \theta_1 - x \sin \theta_1) \delta'(x \cos \theta_1 + y \sin \theta_1)] \\
& + \cos^2 \theta_2 \Theta(y \cos \theta_2 - x \sin \theta_2) [T_2 \delta(x \cos \theta_2 + y \sin \theta_2) \\
& \quad - \frac{1}{2} \Delta P_{\beta\gamma} (y \cos \theta_2 - x \sin \theta_2) (-l_1 + y \cos \theta_2 - x \sin \theta_2) \delta'(x \cos \theta_2 + y \sin \theta_2)] \\
& + \Delta P_{\alpha\gamma} \sin 2\theta_1 (\frac{1}{2} l_1 - y \cos \theta_1 + x \sin \theta_1) \delta(x \cos \theta_1 + y \sin \theta_1) \Theta(y \cos \theta_1 - x \sin \theta_1) \\
& - \Delta P_{\beta\gamma} \sin 2\theta_2 (\frac{1}{2} l_2 - y \cos \theta_2 + x \sin \theta_2) \delta(x \cos \theta_2 + y \sin \theta_2) \Theta(y \cos \theta_2 - x \sin \theta_2) ,
\end{aligned} \tag{B.3}$$

and finally

$$\begin{aligned}
\sigma_{xy} = \sigma_{yx} = & -\Delta P_{\alpha\beta} (\frac{l_0}{2} - y) \delta(x) \Theta(y) \\
& + \Delta P_{\alpha\gamma} \cos(2\theta_1) (\frac{l_2}{2} - y \cos \theta_1 + x \sin \theta_1) \delta(x \cos \theta_1 + y \sin \theta_1) \Theta(y \cos \theta_1 - x \sin \theta_1) \\
& - \Delta P_{\beta\gamma} \cos(2\theta_2) (\frac{l_1}{2} - y \cos \theta_2 + x \sin \theta_2) \delta(x \cos \theta_2 + y \sin \theta_2) \Theta(y \cos \theta_2 - x \sin \theta_2) \\
& - \cos \theta_1 \sin \theta_1 \Theta(y \cos \theta_1 - x \sin \theta_1) [T_1 \delta(x \cos \theta_1 + y \sin \theta_1) \\
& \quad + \frac{1}{2} \Delta P_{\alpha\gamma} (y \cos \theta_1 - x \sin \theta_1) (-l_1 + y \cos \theta_1 - x \sin \theta_1) \delta'(x \cos \theta_1 + y \sin \theta_1)] \\
& - \cos \theta_2 \sin \theta_2 \Theta(y \cos \theta_2 - x \sin \theta_2) [T_2 \delta(x \cos \theta_2 + y \sin \theta_2) \\
& \quad - \frac{1}{2} \Delta P_{\beta\gamma} (y \cos(\theta_2) - x \sin \theta_2) (-l_2 + y \cos \theta_2 - x \sin \theta_2) \delta'(x \cos \theta_2 + y \sin \theta_2)] .
\end{aligned} \tag{B.4}$$

In these equations $\Delta P_{\alpha\gamma} = P_\alpha - P_\gamma$. l_0 , l_1 , and l_2 are the length of the corresponding bonds, 0, 1, 2. The effective tension along these cell bonds are described by T_0 , T_1 , and T_2 (equation 3.10). Bond 0 is along the global y -axis and θ_1 and θ_2 are the angle of the local coordinate systems of bonds 1 and 2 from the global coordinate system (figure B.1).

B.2 Force balance at cell vertices

In order to study the validity of force balance at vertices, we calculate the divergence of the stress tensor introduced in the previous section. The calculation is massive, however,

at the end many terms cancel each other. The force balance can be summarized as

$$\begin{aligned}
\partial_x \sigma_{xx} + \partial_y \sigma_{xy} &= \delta^2(0) [-T_1 \sin \theta_1 - T_2 \sin \theta_2 \\
&\quad + \frac{l_0}{2} \Delta P_{\beta\alpha} + \frac{l_1}{2} \Delta P_{\gamma\beta} \cos \theta_1 + \frac{l_2}{2} \Delta P_{\alpha\gamma} \cos \theta_2] , \\
\partial_y \sigma_{yy} + \partial_x \sigma_{xy} &= \delta^2(0) [-T_0 - T_1 \cos \theta_1 - T_2 \cos \theta_2 \\
&\quad + \frac{l_0}{2} \Delta P_{\beta\alpha} + \frac{l_1}{2} \Delta P_{\gamma\beta} \sin \theta_1 + \frac{l_2}{2} \Delta P_{\alpha\gamma} \sin \theta_2] . \tag{B.5}
\end{aligned}$$

These relations are equal to the derivatives of the energy function of the vertex model (equation 3.1) with respect to the position of the vertex i

$$\begin{aligned}
\partial_x \sigma_{xx} + \partial_y \sigma_{xy} &= \frac{\delta E}{\delta x_i} , \\
\partial_y \sigma_{yy} + \partial_x \sigma_{xy} &= \frac{\delta E}{\delta y_i} . \tag{B.6}
\end{aligned}$$

These quantities represent the forces acting on the vertex and vanish in the equilibrium configurations. With this calculation we can state that stress tensor introduced for the vertex model satisfies force balance everywhere in the cellular network.

Appendix C

Quantification of cell shape

In this appendix we describe how we quantify the shape of two dimensional bodies. In particular we use this method to analyze cell shapes in the cellular network in the vertex model or experimental images of adherens junctions of cells. However, the arguments are general and can be applied to other simple shapes in 2D surfaces. Cell shape in two dimensional tissues can be described by a symmetric tensor. Cell area represents the isotropic part of cell shape which is the trace of this tensor. The traceless part of this tensor denotes cell elongation.

C.1 Tensor of cell elongation

We quantify the elongation of cell α with a symmetric traceless tensor

$$\tau_\alpha = \begin{pmatrix} \mathcal{D}_\alpha & \mathcal{B}_\alpha \\ \mathcal{B}_\alpha & -\mathcal{D}_\alpha \end{pmatrix}. \quad (\text{C.1})$$

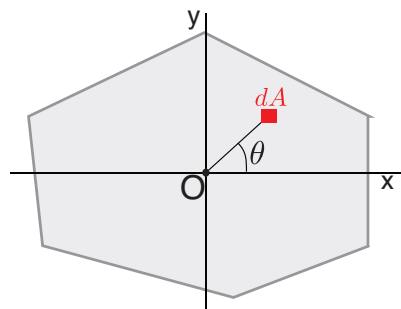


Figure C.1: A scheme of the polar coordinate used in quantifying cell elongation. O is the center of area of the cell. An area element dA is shown in red, θ is its polar angle, with respect to the x -axis.

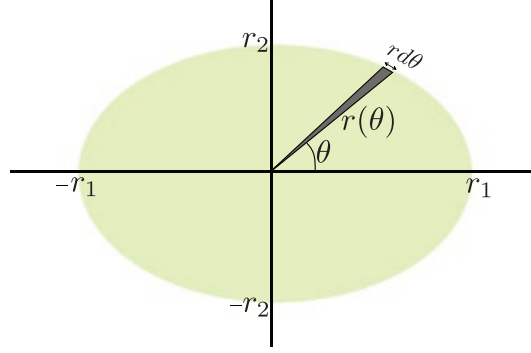


Figure C.2: Polar coordinate system for an ellipse. The shape of the ellipse is described by a function $r(\theta)$ for any polar angle θ . r_1 and r_2 are long and short radii of the ellipse. The area element, shaded in gray, is a triangle (for an infinitesimal angle width $d\theta$) and equals to $dA = \frac{1}{2}r^2d\theta$.

Where \mathcal{D}_α and \mathcal{B}_α are defined as

$$\begin{aligned}\mathcal{D}_\alpha &= \frac{1}{A_\alpha} \int_{A_\alpha} \cos 2\theta \, dA, \\ \mathcal{B}_\alpha &= \frac{1}{A_\alpha} \int_{A_\alpha} \sin 2\theta \, dA.\end{aligned}\tag{C.2}$$

Here the integrals are over the area of cell α and θ is the polar angle of each point with respect to the geometrical center of the cell (figure C.1). This tensor has two symmetric eigenvalues $\pm\varrho$, where

$$\varrho = \sqrt{\mathcal{D}^2 + \mathcal{B}^2}.\tag{C.3}$$

The positive eigenvalue and the corresponding eigenvector of this tensor define the magnitude of cell elongation, ϱ , and an axis of cell elongation with the orientation angle $\Omega = \tan^{-1}((\varrho - \mathcal{D})/\mathcal{B})$. In the other words, the tensor of cell elongation can be written as

$$\tau_\alpha = \varrho \begin{pmatrix} \cos 2\Omega & \sin 2\Omega \\ \sin 2\Omega & -\cos 2\Omega \end{pmatrix}.\tag{C.4}$$

The tensor of cell elongation can be displayed by a bar at angle Ω and length ϱ .

C.2 Ellipse approximation for cell elongation

The magnitude of cell elongation can be mapped to the ratio of long to short axis of the cell. We estimate this ratio by comparing cell elongation with the elongation of an ellipse. Here we calculate the cell shape tensor for an ellipse with the long radius of r_1 and short radius of r_2 (see figure C.2). In a polar coordinate system, where the origin

is located at the geometric center of the ellipse, the shape of the ellipse is described by the polar radius $r(\theta)$ which is a function of the polar angle θ

$$r(\theta) = \frac{r_1 r_2}{\sqrt{(r_1 \sin \theta)^2 + (r_2 \cos \theta)^2}}. \quad (\text{C.5})$$

In this framework, the area element is $dA = \frac{1}{2}r^2 d\theta$ and the area of the ellipse is $\pi r_1 r_2$. Therefore we calculate the integrals \mathcal{D} and \mathcal{B} for the ellipse as follows

$$\begin{aligned} \mathcal{D} &= \frac{r_1 r_2}{\pi} \int_0^\pi \frac{\cos 2\theta}{(r_1 \sin \theta)^2 + (r_2 \cos \theta)^2} d\theta = \frac{r_1 - r_2}{r_1 + r_2}, \\ \mathcal{B} &= \frac{r_1 r_2}{\pi} \int_0^\pi \frac{\sin 2\theta}{(r_1 \sin \theta)^2 + (r_2 \cos \theta)^2} d\theta = 0. \end{aligned} \quad (\text{C.6})$$

Here the ellipse shape tensor is a diagonal tensor, which is because we consider the coordinate system along the semi axes of the ellipse (figure C.2). In this framework, the magnitude of cell elongation is

$$\varrho = \frac{c - 1}{c + 1}, \quad (\text{C.7})$$

where c is the ratio of long to short axis, $c = r_1/r_2$. With the help of this result, we approximate the ratio of long to short axis of a cell with arbitrary shape as $c \simeq (\varrho + 1)/(\varrho - 1)$.

Appendix D

Effective Laplace's law in cellular networks

Laplace's law describes that the pressure difference across the interface between two fluids is proportional to the interface curvature with a coefficient equals to the surface tension. We analyze whether we can define an effective Laplace's law near a curved interface in a cellular network. Figure D.1 shows the distribution of cell area pressure near a curved interface in a hexagonal network. We consider approximately circular interfaces with different radii ($R = 1/C$) in a hexagonal network and increase cell bond tension at the interface with a factor λ relative to the other bonds. The network is relaxed to a local energy minimum. We analyze the distribution of cell area pressure, $P_\alpha = -K(A_\alpha - A^{(0)})$, in the cellular network. The cell area pressure is not uniform near the curved interface if cell bond tension is increased at the interface. The average cell area pressure is calculated in the first cell rows inside and outside of the circle

$$\begin{aligned}\bar{P}_{in} &= \frac{\sum_{\alpha}^{in} P_{\alpha} A_{\alpha}}{\sum_{\alpha}^{in} A_{\alpha}}, \\ \bar{P}_{out} &= \frac{\sum_{\alpha}^{out} P_{\alpha} A_{\alpha}}{\sum_{\alpha}^{out} A_{\alpha}}.\end{aligned}\tag{D.1}$$

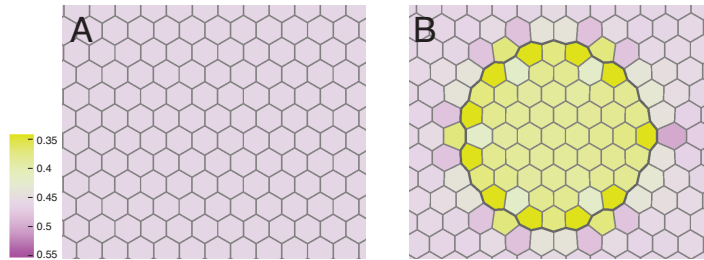


Figure D.1: Cell area pressure in a hexagonal network is color coded. (A) All the cells are identical. (B) Cell bond tension is increased at the dark gray interface by $\lambda = 3$.

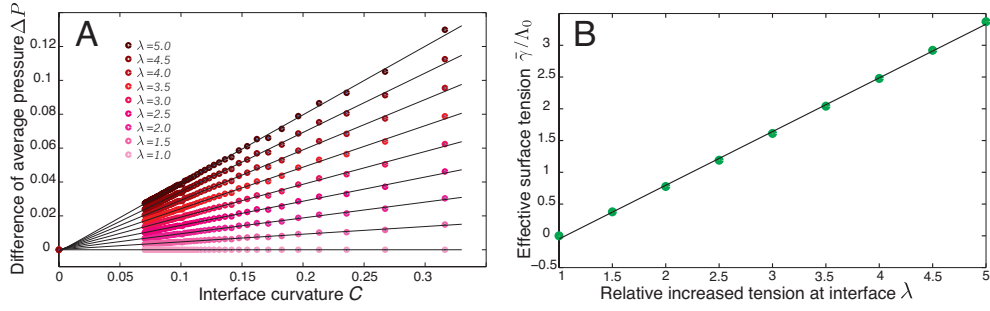


Figure D.2: Laplace's law in cellular networks. (A) The difference average pressure ΔP of inside and outside as a function of interface curvature for different values of relative increased cell bond tension at the interface $\lambda = 1.0, 1.5, 2.0, \dots, 5.0$. A line with slope $\bar{\gamma}$ is fit to each curve. (B) The effective surface tension normalized by bulk bond tension $\bar{\gamma}/\Lambda_0$ as a function of relative cell bond tension at the interface $\lambda = \Lambda_I/\Lambda_0$.

Here *in* and *out* indicate that the sum is over one cell row inside and outside the interface. We observe that the difference of inside and outside average pressure $\Delta P = \bar{P}_{in} - \bar{P}_{out}$ is proportional to the interface curvature in accordance with Laplace's law. We fit a line $\Delta P = \bar{\gamma}C$ to the numerical data (ΔP versus interface curvature C) for different values of λ (figure D.2A). We determine the slope $\bar{\gamma}$ which represents the effective surface tension. It changes linearly with the value of increased bond tension at the interface λ (figure D.2).

Appendix E

Morphology of interfaces

Here we explain how we analyze the morphology of interfaces. We first describe our methods to quantify the shape of interfaces. These methods are used to study the roughness of interfaces during growth simulation in chapter 4. Moreover, we use these methods to quantify the roughness of the DV boundary in the developing fly wing (section 5.1.2). In the second section we analyze the scaling properties of interfaces in our model.

E.1 Quantification of interface morphology

An interface in a cellular network consists of all the bonds shared between two compartments. The shape of the interface is described by the sequence of the position of vertices at the interface $R_i = (X_i, Y_i)$. We consider the y -axis to be along the line $\overline{R_0R_M}$ connecting the end points of the boundary. We describe the shape of the interface with a function $h(y)$, which represents the orthogonal distance of the boundary from the y -axis (figure E.1). Considering that vertices are connected by straight bonds, $h(y)$ is a continuous function. If an overlap exists, we average the orthogonal distance from y -axis to calculate $h(y)$ at each point. There are different methods to quantify the morphology of an interface. Here we describe our methods to analyze the roughness and the Fourier transform of interfaces.

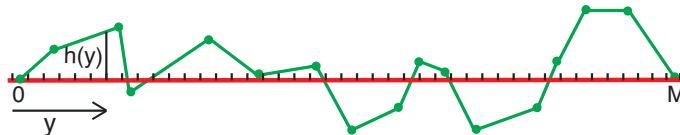


Figure E.1: The shape of an interface is represented by a sequence of vertices (green dots) which are connected by cell bonds (green lines). The reference line, y -axis (colored in red), connects the end points of the interface (vertices 0 and M). Interface shape is described by a function $h(y)$ which measures its orthogonal distance from the reference line.

E.1.1 Roughness as the average peak height

We discussed in section 1.5 that the morphology of interfaces depends on the scale by which they are observed. For any length scale along the interface, roughness characterizes the average depth of excursions of the boundary away from the average straight line [89]. We measure the interface roughness $w(L)$ as the deviation of $h(y)$ from mean value, for any distance L [4]

$$w^2(L) = \frac{1}{LL_y} \int_0^{L_y} dy' \int_0^L dy (h(y+y') - \bar{h}(L, y'))^2. \quad (\text{E.1})$$

Where L_y is the total length of the interface along the y direction. The roughness value is averaged over distance L and along the interface. Here $\bar{h}(L, y')$ is the average height between the points y' and $y' + L$

$$\bar{h}(L, y') = \frac{1}{L} \int_0^L dy h(y+y'). \quad (\text{E.2})$$

This roughness is a standard measure of interface morphology. We use this quantity to compare the shape of interfaces in cellular networks between different cases in section 4.4. This method is also used to quantify the roughness of the DV boundary in wing imaginal discs at different developmental times (section 5.1.2). It should be noted that for experimental images the averages along the boundary are done within the distance $[0, L_y - L]$.

E.1.2 Fourier transform of the interface shape

We know the shape of an interface is described by a function $h(y)$. The Fourier transform of this function $\tilde{h}(q)$ is defined by equation 1.3. The Fourier transform describes interface shape as a function of periodic functions with different wavelengths [110]. Due to the periodic boundary condition we use in the simulations, $h(y)$ is a periodic function in the interval $[0, L_y]$. Therefore the Fourier integral is replaced by the Fourier series

$$h(y) = \sum_{n=0}^{\infty} C_n e^{\frac{2\pi i n y}{L_y}}, \quad (\text{E.3})$$

where C_n is the Fourier complex coefficient which describes the amplitude of periodic waves

$$C_n = \frac{1}{L_y} \int_0^{L_y} e^{-\frac{2\pi i n y}{L_y}} h(y) dy. \quad (\text{E.4})$$

Comparing the Fourier transform and the Fourier coefficients (equation 1.3 and E.4) follows that $C_n = \tilde{h}(n/L_y)/L_y$. We introduce $C(q) = C_n$, where $q = n/L_y$ as L_y varies between different realizations. We average $C(q)$ for different values of q between different realizations.

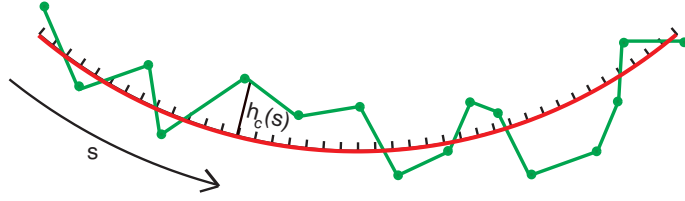


Figure E.2: An interface is shown in green and a circle fit to its shape is shown in red. Here s is the contour length along the fit curve. The shape of the interface is described by its orthogonal distance from the fit circle, $h_c(s)$.

E.1.3 Circle roughness

The roughness introduced in equation E.1 can be generalized to calculate roughness for curved interfaces. Of particular interest, we quantify circle roughness to measure the deviation of interfaces from a circle. We use this method in chapter 5 to study the circle roughness of the dorsoventral boundary which has a global curvature. In this method, we fit a circle to the shape of a curved interface. The fit circle is considered as a reference curve (figure E.2). The orthogonal distance of the interface from the reference circle $h_c(s)$ defines the shape of the interface, where s is the contour length along the fit circle. For any distance L , we calculate the circle roughness $w_c(L)$ as the deviation of the boundary shape from mean line along the reference circle

$$w_c^2(L) = \frac{1}{L(L_0^c - L)} \int_0^{L_0^c - L} ds' \int_0^L ds (h_c(s + s') - \bar{h}_c(L, s'))^2, \quad (\text{E.5})$$

where L_0^c is the total contour length of the interface along the fit circle. The circle roughness is averaged over distance L and along the interface. Here $\bar{h}_c(L, s')$ is the average height between the points s' and $L + s$

$$\bar{h}_c(L, s') = \frac{1}{L} \int_0^L ds h_c(s + s'). \quad (\text{E.6})$$

In the limit that interface curvature vanishes, the circle roughness is equal to the line roughness (equation E.1).

E.2 Scaling properties of interfaces

In this section we analyze these scaling behaviors for the interfaces between cellular compartments in our growth model. The roughness of many interfaces obey simple scaling relations. Equation 1.4 summarizes the scaling properties of interface roughness. This equation defines the growth exponent b , and the roughness exponent a . Starting from a straight interface, roughness increases as a power of time defining the growth exponent b . This is valid in short times and for any distance L along the interface. In our growth simulations time can be replaced by $N_c^{1/2}$. The exponent can be found

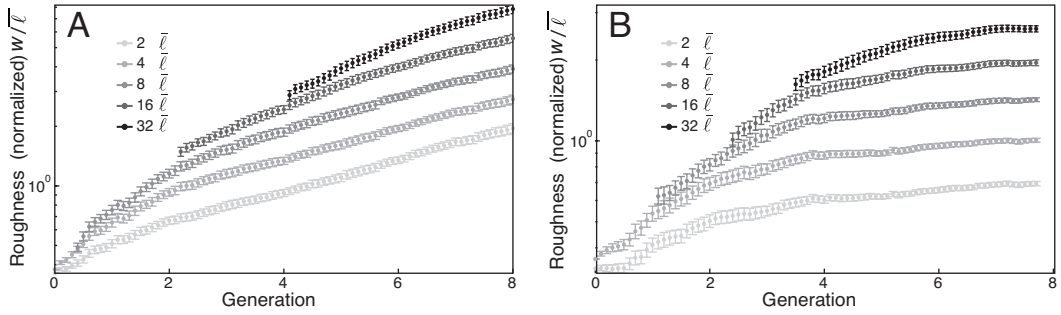


Figure E.3: Examples of roughness growth phase. The interface roughness w in the logarithmic scale as a function of generation G for the indicated distances L along the interface corresponding to the plots in figure 4.10B (A), and figure 4.14F (B).

from the slope of roughness plot in the logarithmic scale as a function of generation. The difficulty is that the linear growth phase can not be noticed easily for many of our interfaces. Figure E.3 shows two examples of roughness growth. In the first example, regarding the reference case, the growth phase can be recognized, beyond the second generation. However, in the second example, the growth phase is short and it is hard to measure the growth exponent. For the cases where we could distinguish the growth phase, the growth exponent varies between 0.6 and 1.0.

In many simulations roughness saturates after several generations. The saturation value of roughness scales with the length L , defining the roughness exponent a . In the saturated regime we can measure the roughness exponent a as the slope of roughness $w(L)$ in a logarithmic scale (see figure 4.19A). Figure E.4 shows the roughness exponent for different mechanisms. We do not calculate it for $\lambda = 1$ since the saturation phase hardly exists.

The other exponent represents how the Fourier transform of interfaces scales with the wavelength (equation 4.7). We calculate the Fourier exponent f as the slope of Fourier transform function in a logarithmic scale (See figure 4.19B). Figure E.5 shows the Fourier exponent for different mechanisms and different values of bond tension along the interface. Both the roughness and the Fourier exponents remains almost unchanged between different mechanisms in our model.

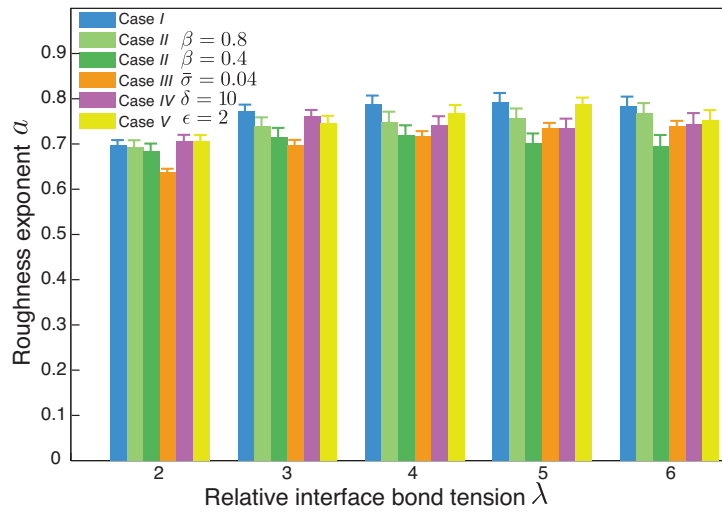


Figure E.4: Roughness exponent as a function of relative bond tension along the interface. Each color represents one case describing different mechanisms, increased bond tension along the interface (case *I*), reduced proliferation near the interface (case *II*), external shear (case *III*), orientated cell division (case *IV*), and pressure-dependent division rate (case *V*). Mean and SEM are shown.

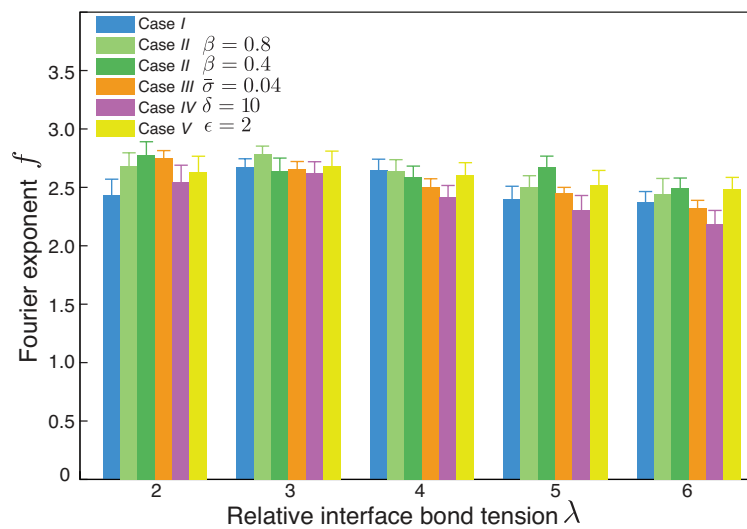


Figure E.5: Fourier Exponent as a function of relative bond tension along the interface. Different colors denote different cases. Mean and SEM are shown.

Appendix F

Cell morphology near an interface in a cellular network

In this appendix, we analyze the morphology of cells in the vicinity of an interface between cellular compartments in our simulations. In chapter 4 we discussed that increasing bond tension at the interface leads to shorter cell bonds along the interface, or cells are bigger in the zone of reduced proliferation. However, here we consider the reference case, where all the cells have identical mechanical properties. However, after thousands of stochastic cell divisions, cells have distinct shape and area due to the stochastic behavior of cell rearrangements. We study the distribution of cell shape near the interface between two compartments. We first quantify average area of cells in different cell rows near the interface (see figure F.1B). This plot shows that the average cell area in the first cell row at the interface is higher, by about 5%, compared to the average cell area in bulk. Although the difference is small, it is astonishing to obtain a non-homogeneous distribution of cell area when the mechanical properties of all cells are identical. We know that in a box containing tens of cells, cell properties are in average independent of the position of the box.

To test the validity of this result, we analyze the distribution of cell area near interfaces with specific shapes. We introduce cellular compartments with specific shapes of interfaces in a grown cellular network. Cells are sorted in two compartments according to the position of their geometric center (x_c, y_c) relative to a line with a particular shape. Figure F.1C shows an example with a straight interface, for the blue cells $y_c < L_y/2$. We still notice that cell average area is not uniform in different cell rows (figure F.1D). Similar results are obtained for interfaces with sinusoidal shapes.

In order to compare the average area of cells in different cell rows, we study the distribution of cell area in these regions. Figure F.2 shows the probability distribution of cell area $P(A)$ throughout a cellular network after thousands of cell division. The average cell area is given by

$$\langle A_\alpha \rangle = \frac{\int P(A) A dA}{\int P(A) dA} . \quad (\text{F.1})$$

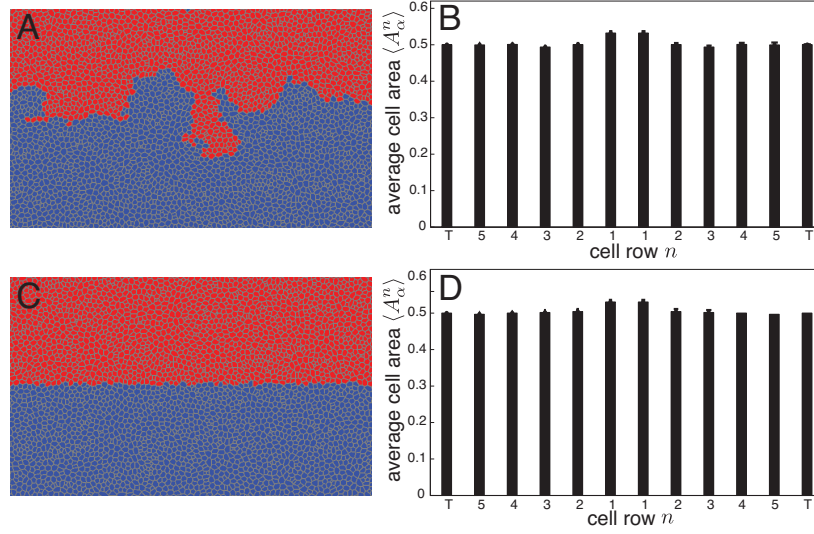


Figure F.1: The first column (A, C) represents examples of the shape of interfaces in cellular networks of identical cells. The second column (B, D) shows the average cell area in different cell rows in the vicinity of interfaces. Mean and SEM are shown ($n = 20$ realizations). (A, B) The reference case, where the interface gets rough during growth. (C, D) A straight interface is introduced in a grown cellular network.

The average cell area of cell row n can be calculated in the same way by using the probability distribution of cell area in this cell row $P^n(A)$

$$\langle A_\alpha^n \rangle = \frac{\int P^n(A) A dA}{\int P^n(A) dA} . \quad (\text{F.2})$$

We use the probability distribution of cell area throughout the cellular network $P(A)$, and estimate the probability distribution of cell area in the first cell rows $P^1(A)$. We consider the interface shape is given by a specified function. The first cell row contains all the cells which share a bond along the interface. In a simplified picture, the typical perpendicular distance of cell center to the interface d should be smaller than cell radius a if cell lies in the first row (a scheme is shown in figure F.2B). Therefore, the probability of being in the first row is proportional to the cell radius a , which is proportional to $\sqrt{A_\alpha}$ in an isotropic picture. We conclude that the probability distribution for cell area in the first cell row is given by

$$P^1(A) \propto P(A) \sqrt{A_\alpha} . \quad (\text{F.3})$$

This probability can be replaced in equation F.2 to estimate the average cell area in the first row

$$\langle A_\alpha^1 \rangle = \frac{\int P(A) A^{3/2} dA}{\int P(A) A^{1/2} dA} . \quad (\text{F.4})$$

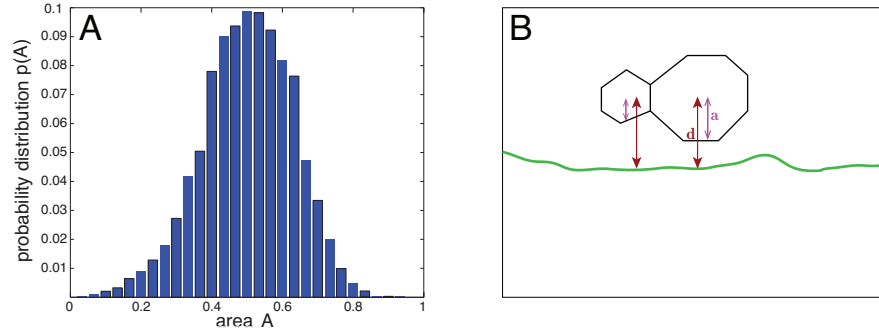


Figure F.2: (A) The normalized probability distribution $P(A)$ of cell area in a cellular network after thousands of cell divisions. (B) A scheme of area distribution of cells in the vicinity of an interface (green line). Here d (shown in red) is the typical distance of cell center from the interface and a (shown in pink) is cell radius, which measures the typical distance of cell center and cell border along d .

Considering the probability distribution of cell area P_A as shown in figure F.2A, we estimate that the average cell area in the first row $\langle A_\alpha^1 \rangle$ is higher than the average cell area of the tissue $\langle A_\alpha \rangle$ by about 5%. This estimate explains very well the results shown in figure F.1.

Furthermore, we analyze the average values of cell bond length, cell perimeter, and the angle between cell bonds for different cell rows near an interface (figure F.3). All these quantities show special nonuniform profiles near interfaces. We can explain these profiles with a similar approach as what explained here for the profile of average cell area. To justify the observed profiles of cell bond length and cell bond angle, this simple picture should be improved by taking into account elongation of cells near interfaces.

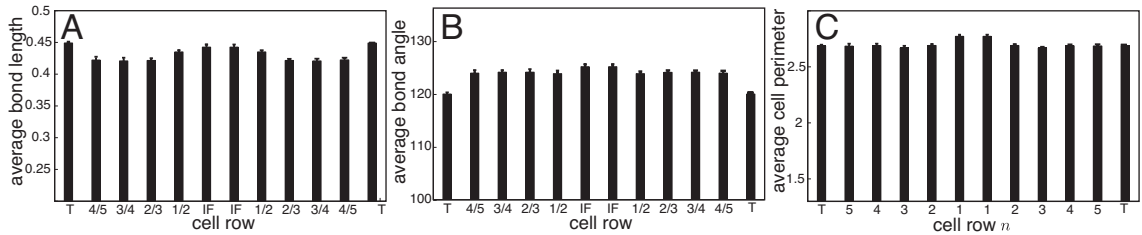


Figure F.3: (A) The average bond length, (B) the average angle between cell bonds shared between different cell rows, and (C) the average cell perimeter in different cell rows, for the reference case. Mean and SEM are shown ($n = 20$ realizations).

Appendix G

Analysis of experimental images

We quantify morphology of cells and compartment boundaries by analyzing images of the wing imaginal discs. Experimental images show the epithelia at the level of adherens junctions (figure G.1A,B). Since wing discs are not flat, each image is a projection of several single images of a wing disc from different focal planes where the staining of adherens junctions is detectable. Wing discs, which are stained for *E-cadherin*, can be analyzed to distinguish the network of adherens junctions. For automated image analysis, we use packing analyzer v2.0 [111]. The program automatically recognizes the position of cell bonds and cell vertices in the experimental images (figure G.1C).

We need extra information from the experimental images. Specifically, we are interested in the shape of compartment boundaries. Furthermore we want to quantify cell shapes, and compare the properties of cells in different regions in the wing disc. For this purpose we developed a code that reads the position of vertices produced by the packing analyzer and transform it into our standard structure of data sets. Therefore we can quantify different characteristic of cells and compartment boundaries. We first need to distinguish the position of compartment boundaries. Cells within dorsal compartments express CD8-GFP in experimental images (figure G.1A). We identify cells within the first rows on both sides of the DV boundary. With the help of this information, the program can detect the vertices along the interface and analyze the shape of the compartment boundary. This program distinguishes cells within different compartments and sort cells into different cell rows around the compartment boundary. We quantify cell properties for different rows of cells to analyze tissue anisotropies near the compartment boundaries. Specifically, we look at the average apical cell area, cell perimeter, cell bond length, angle between cell bonds, the distribution of neighbor numbers for cells, and elongation of cells.

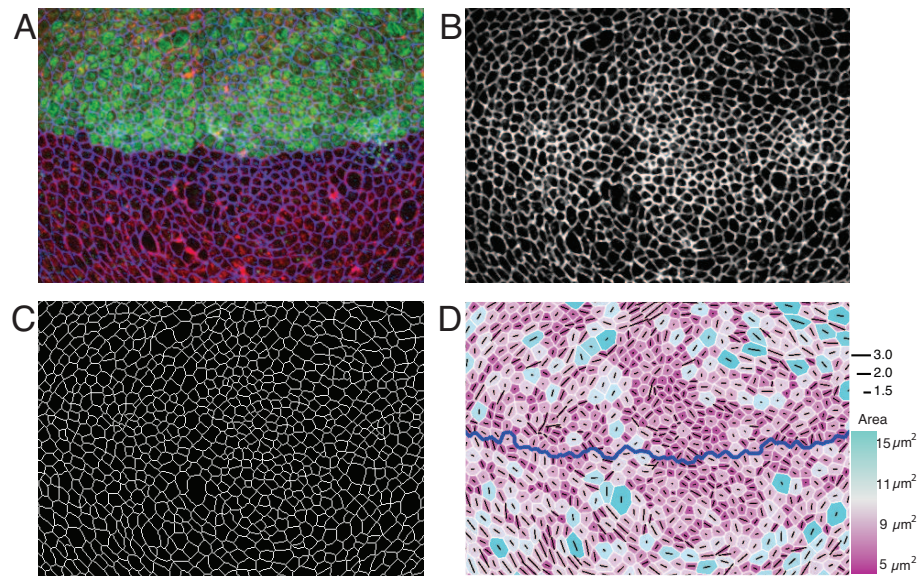


Figure G.1: Analysis of experimental images. (A) An image of the wing imaginal disc stained for *E-cad* (red). Cells in dorsal compartment express CD8-GFP (green). (B) *E-cad* segmentation of (A). This image is loaded into the packing analyzer. (C) The network of adherens junctions recognized by the the packing analyzer. (D) The network of adherens junctions rebuilt and analyzed by our code. Blue line demarcates the DV boundary. Apical cross sectional area is color coded (right). Elongation of individual cells is shown by black bars and their lengths represents ratio of long to short axis of a cell (right).

Bibliography

- [1] L. Wolpert, T. Jessell, P. Lawrence, E. Meyerowitz, E. Robertson, and J. Smith. *Principles of Development*. Oxford: Oxford University Press, 2nd edition, 2002.
- [2] R. Farhadifar, J.-C. Röper, B. Aigouy, S. Eaton, and F. Jülicher. The influence of cell mechanics, cell-cell interactions, and proliferation on epithelial packing. *Current Biology*, **17**(24): 2095, 2007.
- [3] B. Alberts, A. Johnson, J. Lewis, M. Raff, K. Roberts, and P. Walter. *Molecular Biology of the Cell*. New York: Garland Science, 4th edition, 2002.
- [4] K. P. Landsberg, R. Farhadifar, J. Ranft, D. Umetsu, T. J. Widmann, T. Bittig, A. Said, F. Jülicher, and C. Dahmann. Increased cell bond tension governs cell sorting at the drosophila anteroposterior compartment boundary. *Current Biology*, **19**(22): 1950, 2009.
- [5] J. Vincent. Compartment boundaries: where, why and how? *The International Journal of Developmental Biology*, **42**: 311, 1998.
- [6] H. McNeill. Sticking together and sorting things out: adhesion as a force in development. *Nature Reviews Genetics*, **1**: 100, 2000.
- [7] K. Irvine and C. Rauskolb. Boundaries in development: formation and function. *Annual Review of Cell and Developmental Biology*, **17**: 189, 2001.
- [8] U. Tepass, D. Godt, and R. Winklbauer. Cell sorting in animal development: signalling and adhesive mechanisms in the formation of tissue boundaries. *Current Opinion in Genetics and Development*, **12**(5): 572, 2002.
- [9] S. S. Blair. Developmental biology: Boundary lines. *Nature*, **424**(6947): 379, 2003.
- [10] J. Vincent and D. Irons. Developmental biology: tension at the border. *Current Biology*, **19**: R1028, 2009.
- [11] A. C. Martin and E. F. Wieschaus. Tensions divide. *Nature Cell Biology*, **12**(1): 5, 2010.

- [12] C. Dahmann, A. C. Oates, and M. Brand. Boundary formation and maintenance in tissue development. *Nature Reviews Genetics*, **12**(1): 43, 2011.
- [13] B. Monier, A. Pelissier-Monier, and B. Sanson. Establishment and maintenance of compartmental boundaries: role of contractile actomyosin barriers. *Cellular and Molecular Life Sciences*, **68**(11): 1897, 2011.
- [14] A. Garcia-Bellido, P. Ripoll, and G. Morata. Developmental compartmentalisation of the wing disk of drosophila. *Nature New Biology*, **245**: 251, 1973.
- [15] P. A. Lawrence. A clonal analysis of segment development in oncopeltus. *Journal of Embryology and Experimental Morphology*, **30**(3): 681, 1973.
- [16] J.-P. Vincent and P. H. O'Farrell. The state of engrailed expression is not clonally transmitted during early drosophila development. *Cell*, **68**(5): 923, 1992.
- [17] N. A. Sunmonu, K. Li, Q. Guo, and J. Y. H. Li. Gbx2 and fgf8 are sequentially required for formation of the midbrain-hindbrain compartment boundary. *Development*, **138**(4): 725, 2011.
- [18] C. Dahmann and K. Basler. Compartment boundaries: at the edge of development. *Trends in Genetics*, **15**(8): 320, 1999.
- [19] M. Steinberg. Reconstruction of tissues by dissociated cells. some morphogenetic tissue movements and the sorting out of embryonic cells may have a common explanation. *Science*, **141**: 401408, 1963.
- [20] D. Godt and U. Tepass. Drosophila oocyte localization is mediated by differential cadherin-based adhesion. *Nature*, **395**(6700): 387, 1998.
- [21] A. Nose, A. Nagafuchi, and M. Takeichi. Expressed recombinant cadherins mediate cell sorting in model systems. *Cell*, **54**(7): 993, 1988.
- [22] A. Harris. Is cell sorting caused by differences in the work of intercellular adhesion? a critique of the steinberg hypothesis. *Journal of Theoretical Biology*, **61**: 267285, 1976.
- [23] R. Major and K. Irvine. Localization and requirement for myosin ii at the dorsal-ventral compartment boundary of the drosophila wing. *Developmental Dynamics*, **235**: 3051, 2006.
- [24] R. Major and K. Irvine. Influence of notch on dorsoventral compartmentalization and actin organization in the drosophila wing. *Development*, **132**: 3823, 2005.
- [25] B. Monier, A. Pelissier-Monier, A. H. Brand, and B. Sanson. An actomyosin-based barrier inhibits cell mixing at compartmental boundaries in drosophila embryos. *Nature Cell Biology*, **12**(1): 60, 2010.

- [26] D. P. Kiehart, C. G. Galbraith, K. A. Edwards, W. L. Rickoll, and R. A. Montague. Multiple forces contribute to cell sheet morphogenesis for dorsal closure in drosophila. *The Journal of Cell Biology*, **149**(2): 471, 2000.
- [27] T. J. Widmann. *The Role of DPP and Wingless Signaling Gradients in Directing Cell Shape During Drosophila Wing Imaginal Disc Development*. Ph.D. thesis, Technischen Universität Dresden, 2009.
- [28] C. Auerbach. The development of legs, wings, and halteres in wild type and some mutant strains of drosophila melanogaster. *Trans. R. Soc. Edinb.*, **58**(787-815), 1936.
- [29] K. D. McClure and G. Schubiger. Developmental analysis and squamous morphogenesis of the peripodial epithelium in drosophila imaginal discs. *Development*, **132**: 5033, 2005.
- [30] F. T. Lewis. The effect of cell division on the shape and size of hexagonal cells. *The Anatomical Record*, **33**(5): 331, 1926.
- [31] S. S. Blair. Lineage compartments in drosophila. *Current Biology*, **13**(14): R548, 2003.
- [32] P. A. Lawrence and G. Struhl. Morphogens, compartments, and pattern: Lessons from drosophila? *Cell*, **85**(7): 951, 1996.
- [33] S. Blair and A. Ralston. Smoothed-mediated hedgehog signaling is required for the maintenance of the anterior-posterior lineage restriction in the developing wing of drosophila. *Development*, **124**: 4053, 1997.
- [34] I. Rodriguez and K. Basler. Control of compartmental affinity boundaries by hedgehog. *Nature*, **389**(6651): 614, 1997.
- [35] C. Dahmann and K. Basler. Opposing transcriptional outputs of hedgehog signaling and engrailed control compartmental cell sorting at the drosophila a/p boundary. *Cell*, **100**(4): 411, 2000.
- [36] J. Shen and C. Dahmann. The role of dpp signaling in maintaining the drosophila anteroposterior compartment boundary. *Developmental Biology*, **279**(1): 31, 2005.
- [37] K. G. Coleman, S. J. Poole, M. P. Weir, W. C. Soeller, and T. Kornberg. The invected gene of drosophila: sequence analysis and expression studies reveal a close kinship to the engrailed gene. *Genes and Development*, **1**: 19, 1987.
- [38] J. J. Lee, D. P. von Kessler, S. Parks, and P. A. Beachy. Secretion and localized transcription suggest a role in positional signaling for products of the segmentation gene hedgehog. *Cell*, **71**(1): 33, 1992.

- [39] K. Basler and G. Struhl. Compartment boundaries and the control of drosophila limb pattern by hedgehog protein. *Nature*, **368**(6468): 208, 1994.
- [40] A. Kicheva, P. Pantazis, T. Bollenbach, Y. Kalaidzidis, T. Bittig, F. Jülicher, and M. González-Gaitán. Kinetics of morphogen gradient formation. *Science*, **315**(5811): 521, 2007.
- [41] M. Zecca, K. Basler, and G. Struhl. Sequential organizing activities of engrailed, hedgehog and decapentaplegic in the drosophila wing. *Development*, **121**(8): 2265, 1995.
- [42] T. Lecuit, W. J. Brook, M. Ng, M. Calleja, H. Sun, and S. M. Cohen. Two distinct mechanisms for long-range patterning by decapentaplegic in the drosophila wing. *Nature*, **381**(6581): 387, 1996.
- [43] S. Schilling, M. Willecke, T. Aegerter-Wilmsen, O. A. Cirpka, K. Basler, and C. von Mering. Cell-sorting at the a/p boundary in the drosophila wing primordium: A computational model to consolidate observed non-local effects of hh signaling. *PLOS Computational Biology*, **7**(4): 1002025, 2011.
- [44] A. Garcia-Bellido and J. R. Merriam. Parameters of the wing imaginal disc development of drosophila melanogaster. *Developmental Biology*, **24**(1): 61, 1971.
- [45] P. Bryant. Cell lineage relationships in the imaginal wing disc of drosophila melanogaster. *Developmental Biology*, **22**: 389, 1970.
- [46] A. Garcia-Bellido, P. Ripoll, and G. Morata. Developmental compartmentalization in the dorsal mesothoracic disc of drosophila. *Developmental Biology*, **48**: 132, 1976.
- [47] S. Blair, D. Brower, J. Thomas, and M. Zavortink. The role of apterous in the control of dorsoventral compartmentalization and ps integrin gene expression in the developing wing of drosophila. *Development*, **120**: 1805, 1994.
- [48] C. Rauskolb, T. Correia, and K. D. Irvine. Fringe-dependent separation of dorsal and ventral cells in the drosophila wing. *Nature*, **401**(6752): 476, 1999.
- [49] S. S. Blair. Mechanisms of compartment formation: evidence that non-proliferating cells do not play a critical role in defining the d/v lineage restriction in the developing wing of drosophila. *Development*, **119**(2): 339, 1993.
- [50] M. Milán and S. M. Cohen. Notch signaling is not sufficient to define the affinity boundary between dorsal and ventral compartments. *Molecular Cell*, **4**(6): 1073, 1999.

- [51] M. Strigini and S. M. Cohen. Wingless gradient formation in the drosophila wing. *Current Biology*, **10**(6): 293, 2000.
- [52] A. Martinez-Arias. Wnts as morphogens? the view from the wing of drosophila. *Nature Reviews Molecular Cell Biology*, **4**(4): 321, 2003.
- [53] J. Couso, M. Bate, and A. Martinez-Arias. A wingless-dependent polar coordinate system in drosophila imaginal discs. *Science*, **259**(5094): 484, 1993.
- [54] M. Zecca, K. Basler, and G. Struhl. Direct and long-range action of a wingless morphogen gradient. *Cell*, **87**(5): 833, 1996.
- [55] D. O’Brochta and P. Bryant. A zone of non-proliferating cells at a lineage restriction boundary in drosophila. *Nature*, **313**: 138, 1985.
- [56] I. Becam, N. Rafel, X. Hong, S. M. Cohen, and M. Milan. Notch-mediated repression of bantam mirna contributes to boundary formation in the drosophila wing. *Development*, **138**(17): 3781, 2011.
- [57] L. A. Baena-López, A. Baonza, and A. García-Bellido. The orientation of cell divisions determines the shape of drosophila organs. *Current Biology*, **15**(18): 1640, 2005.
- [58] O. Canela-Xandri, F. Sagués, J. Casademunt, and J. Buceta. Dynamics and mechanical stability of the developing dorsoventral organizer of the wing imaginal disc. *PLOS Computational Biology*, **7**(9): e1002153, 2011.
- [59] O. Thoumine and A. Ott. Time scale dependent viscoelastic and contractile regimes in fibroblasts probed by microplate manipulation. *Journal of Cell Science*, **110**(17): 2109, 1997.
- [60] G. Forgacs, R. A. Foty, Y. Shafir, and M. S. Steinberg. Viscoelastic properties of living embryonic tissues: a quantitative study. *Biophysical journal*, **74**(5): 2227, 1998.
- [61] A. Goriely, M. Robertson-Tessi, M. Tabor, and R. Vandiver. Elastic growth models. In R. P. Mondaini, P. M. Pardalos, P. M. Pardalos, and D. W. Hearn, editors, *Mathematical Modelling of Biosystems*, volume 102 of *Applied Optimization*, pages 1–44. Springer Berlin Heidelberg, 2008.
- [62] W. A. Malik, S. C. Prasad, K. R. Rajagopal, and L. Preziosi. On the modeling of the viscoelastic response of embryonic tissues. *Mathematics and Mechanics of Solids*, **13**(1): 81, 2008.
- [63] T. J. Newman. Modeling multicellular systems using subcellular elements. *Mathematical Biosciences and Engineering*, **2**: 611, 2005.

- [64] J. M. Ranft. *Mechanics of Growing Tissues: A Continuum Description Approach*. Ph.D. thesis, l'université Pierre et Marie Curie and TU Dresden, 2012.
- [65] E. Hannezo, J. Prost, and J. F. Joanny. Instabilities of monolayered epithelia: Shape and structure of villi and crypts. *Physical Review Letters*, **107**(7): 078104, 2011.
- [66] J. Ranft, J. Prost, F. Jülicher, and J. Joanny. Tissue dynamics with permeation. *The European Physical Journal E: Soft Matter and Biological Physics*, **35**(6): 1, 2012.
- [67] M. Basan, T. Risler, J.-F. Joanny, X. Sastre-Garau, and J. Prost. Homeostatic competition drives tumor growth and metastasis nucleation. *HFSP Journal*, **3**(4): 265, 2009.
- [68] A. Tosin and L. Preziosi. Multiphase modeling of tumor growth with matrix remodeling and fibrosis. *Mathematical and Computer Modelling*, **52**(7–8): 969, 2010.
- [69] L. Preziosi and G. Vitale. A multiphase model of tumor and tissue growth including cell adhesion and plastic reorganization. *Mathematical Models and Methods in Applied Sciences*, **21**(09): 1901, 2011.
- [70] D. DRASDO. Coarse graining in simulated cell populations. *Advances in Complex Systems*, **8**: 319, 2005.
- [71] H. M. Byrne, J. R. King, D. L. S. McElwain, and L. Preziosi. A two-phase model of solid tumour growth. *Applied Mathematics Letters*, **16**(4): 567, 2003.
- [72] L. Hufnagel, A. A. Teleman, H. Rouault, S. M. Cohen, and B. I. Shraiman. On the mechanism of wing size determination in fly development. *Proceedings of the National Academy of Sciences*, **104**(10): 3835, 2007.
- [73] T. Bittig, O. Wartlick, A. Kicheva, M. González-Gaitán, and F. Jülicher. Dynamics of anisotropic tissue growth. *New Journal of Physics*, **10**(6): 063001, 2008.
- [74] J. Ranft, M. Basan, J. Elgeti, J.-F. Joanny, J. Prost, and F. Jülicher. Fluidization of tissues by cell division and apoptosis. *Proceedings of the National Academy of Sciences*, 2010.
- [75] J. Ahringer. Control of cell polarity and mitotic spindle positioning in animal cells. *Current Opinion in Cell Biology*, **15**(1): 73, 2003.
- [76] W. T. Gibson, J. H. Veldhuis, B. Rubinstein, H. N. Cartwright, N. Perrimon, G. W. Brodland, R. Nagpal, and M. C. Gibson. Control of the mitotic cleavage plane by local epithelial topology. *Cell*, **144**(3): 427, 2011.

- [77] B. Dubertret, T. Aste, H. M. Ohlenbusch, and N. Rivier. Two-dimensional froths and the dynamics of biological tissues. *Physical Review E*, **58**(5): 6368, 1998.
- [78] D. W. Thompson. *On Growth and Form*. Cambridge: University Press; New York: Macmillan, 1945.
- [79] R. W. KORN and R. M. SPALDING. The geometry of plant epidermal cells. *New Phytologist*, **72**(6): 1357, 1973.
- [80] R. Cowan and V. B. Morris. Cell population dynamics during the differentiative phase of tissue development. *Journal of Theoretical Biology*, **122**(2): 205, 1986.
- [81] M. C. Gibson, A. B. Patel, R. Nagpal, and N. Perrimon. The emergence of geometric order in proliferating metazoan epithelia. *Nature*, **442**(7106): 1038, 2006.
- [82] M. Miri and N. Rivier. Universality in two-dimensional cellular structures evolving by cell division and disappearance. *Physical Review E*, **73**(3): 031101, 2006.
- [83] R. Farhadifar. *Dynamics of Cell Packing and Polar Order in Developing Epithelia*. Ph.D. thesis, Technische Universitat Dresden, 2009.
- [84] D. Staple, R. Farhadifar, J. Röper, B. Aigouy, S. Eaton, and F. Jülicher. Mechanics and remodelling of cell packings in epithelia. *The European Physical Journal E: Soft Matter and Biological Physics*, **33**(2): 117, 2010.
- [85] A. Brú, S. Albertos, J. Luis Subiza, J. L. García-Asenjo, and I. Brú. The universal dynamics of tumor growth. *Biophysical journal*, **85**(5): 2948, 2003.
- [86] E. Ben-Jacob. From snowflake formation to growth of bacterial colonies ii: Co-operative formation of complex colonial patterns. *Contemporary Physics*, **38**(3): 205, 1997.
- [87] S. Safran. *Statistical Thermodynamics Of Surfaces, Interfaces, And Membranes*, volume 90. Addison-Wesley Pub. (Reading, Mass.), 1994.
- [88] J. S. Rowlinson and B. Widom. *Molecular Theory of Capillarity*. Dover publication, 2002.
- [89] A.-L. Barabási and H. E. Stanley. *Fractal Concepts in Surface Growth*. Cambridge University: Cambridge, UK, 1995.
- [90] T. Vicsek. *Fractal Growth Phenomena*. World Scientific, 2nd edition, 1992.
- [91] H. E. Stanley and N. Ostrowsky. On growth and form: Fractal and non-fractal patterns in physics. In *Proc. 1985 Cargèse NATO ASI, Series E: Applied Sciences*, volume 100. Nijhoff, Dordrecht, 1985.

- [92] M. Kardar, G. Parisi, and Y.-C. Zhang. Dynamic scaling of growing interfaces. *Physical Review Letters*, **56**: 889, 1986.
- [93] R. A. Fisher. The wave of advance of advantageous genes. *Annals of Human Genetics*, **7**(4): 355, 1937.
- [94] J. D. Murray. *Mathematical Biology (3rd Ed)*, volume I (An Introduction). Springer-Verlag, 2002.
- [95] M. Kardar. *Statistical Physics of Fields*. Cambridge University Press, 2007.
- [96] P. M. Chaikin and T. C. Lubensky. *Principles of Condensed Matter Physics*. Cambridge University Press, 2000.
- [97] W. van Saarloos. Front propagation into unstable states: Marginal stability as a dynamical mechanism for velocity selection. *Physical Review A*, **37**(1): 211, 1988.
- [98] W. van Saarloos. Front propagation into unstable states. *Physics Reports*, **386**(2–6): 29, 2003.
- [99] P. Mumcu. *Self-organized Growth in Developing Epithelia*. Ph.D. thesis, Technische Universität Dresden, 2011.
- [100] T. Aegerter-Wilmsen, C. M. Aegerter, E. Hafen, and K. Basler. Model for the regulation of size in the wing imaginal disc of drosophila. *Mechanisms of Development*, **124**(4): 318, 2007.
- [101] L. D. Landau, L. P. Pitaevskii, E. M. Lifshitz, and A. M. Kosevich. *Theory of Elasticity*, volume 3rd. Elsevier Ltd, 1995.
- [102] M. Aliee, J.-C. Röper, K. P. Landsberg, C. Pentzold, T. J. Widmann, F. Jülicher, and C. Dahmann. Physical mechanisms shaping the drosophila dorsoventral compartment boundary. *Current biology*, **22**(11): 967, 2012.
- [103] S. Guthrie, M. Butcher, and A. Lumsden. Patterns of cell division and interkinetic nuclear migration in the chick embryo hindbrain. *Journal of Neurobiology*, **22**: 742, 1991.
- [104] M. Calleja, E. Moreno, S. Pelaz, and G. Morata. Visualization of gene expression in living adult drosophila. *Science*, **274**(252-255), 1996.
- [105] K. Gustafson and G. Boulianne. Distinct expression patterns detected within individual tissues by the gal4 enhancer trap technique. *Genome*, **39**(1): 174, 1996.
- [106] L. Johnston and B. Edgar. Wingless and notch regulate cell-cycle arrest in the developing drosophila wing. *Nature*, **394**: 82, 1998.

-
- [107] F. Martin, S. Herrera, and G. Morata. Cell competition, growth and size control in the drosophila wing imaginal disc. *Development*, **136**: 3747, 2009.
- [108] S. Eaton and F. Jülicher. Cell flow and tissue polarity patterns. *Current Opinion in Genetics and Development*, **21**(6): 747, 2011.
- [109] J. F. Joanny, F. Jülicher, K. Kruse, and J. Prost. Hydrodynamic theory for multi-component active polar gels. *New Journal of Physics*, **9**(11): 422, 2007.
- [110] G. B. Arfken and H. J. Weber. *Mathematical Methods for Physicists*. Academic Press, New York, 1985.
- [111] B. Aigouy, R. Farhadifar, D. Staple, A. Sagner, J. Roper, F. Jülicher, and S. Eaton. Cell flow reorients the axis of planar polarity in the wing epithelium of drosophila. *Cell*, **142**: 773, 2010.

Versicherung

Hiermit versichere ich, dass ich die vorliegende Arbeit ohne unzulässige Hilfe Dritter und ohne Benutzung anderer als der angegebenen Hilfsmittel angefertigt habe; die aus fremden Quellen direkt oder indirekt übernommenen Gedanken sind als solche kenntlich gemacht. Die Arbeit wurde bisher weder im Inland noch im Ausland in gleicher oder ähnlicher Form einer anderen Prüfungsbehörde vorgelegt. Die vorliegende Arbeit wurde am Max-Planck-Institut für Physik komplexer Systeme angefertigt und von Prof. Dr. Frank Jülicher betreut. Meine Person betreffend erkläre ich hiermit, dass keine früheren erfolglosen Promotionsverfahren stattgefunden haben. Ich erkenne die Promotionsordnung der Fakultät für Mathematik und Naturwissenschaften, Technische Universität Dresden an.

Dresden, den 01.01.2013, Maryam Aliee